

Exploring the role of small-scale thermohaline structure on mixing and transport in the ocean

Author:

Li, Yuehua

Publication Date:

2017

DOI:

<https://doi.org/10.26190/unsworks/20294>

License:

<https://creativecommons.org/licenses/by-nc-nd/3.0/au/>

Link to license to see what you are allowed to do with this resource.

Downloaded from <http://hdl.handle.net/1959.4/59745> in <https://unsworks.unsw.edu.au> on 2024-04-20

Exploring the role of small-scale thermohaline structure on mixing and transport in the ocean

Yuehua Li

Supervisor: Scientia Professor Trevor McDougall

Co-supervisors: Dr. Shane Keating

Professor Matthew England

A thesis in fulfilment of the requirements for the degree of
Doctor of Philosophy



UNSW
SYDNEY

School of Mathematics and Statistics

Faculty of Science

December 2017

THE UNIVERSITY OF NEW SOUTH WALES
Thesis/Dissertation Sheet

Surname or Family name: Li

First name: Yuehua

Other name/s:

Abbreviation for degree as given in the University calendar: PhD

School: School of Mathematics and Statistics

Faculty: Science

Title: Exploring the role of small-scale thermohaline structure on mixing and transport in the ocean

Abstract

Salt and heat are two ocean properties of vital importance. Their mean distribution, their advective transport and their diffusive redistribution control ocean dynamics by setting the density of seawater and its spatio-temporal variability. In this thesis, we investigate two aspects of the mixing and transport of salt and heat: the role of double diffusion, a consequence of the slower molecular diffusion of salt relative to heat; and the impact of small-scale density gradients on the poleward heat transport of the ocean.

In the first part of this thesis, double-diffusive interleaving is examined as it progresses from a linear instability towards finite amplitude. We examine the “finger” and “diffusive” instability types and ask whether a steady state is possible. We find that the ratio of the strengths of the fluxes across the “diffusive” interfaces must be many times stronger relative to the corresponding fluxes across the “finger” interfaces than is indicated from existing flux laws as derived from laboratory experiments. The total effect of the interleaving motion on the vertical fluxes of heat and of salt is calculated for the steady-state solutions. It is found that both the fluxes of heat and salt are up-gradient, corresponding to negative vertical diffusion coefficients for heat, salt and density.

The remainder of the thesis addresses the limited spatial resolution of ocean models. Unresolved spatial correlations between horizontal velocity and tracer fields contribute to the actual horizontal fluxes of heat and other scalar quantities but are not accounted for by state-of-the-art ocean models. A method of estimating these unresolved fluxes is proposed, based on calculating an additional non-divergent velocity to advect all scalar variables. The sum of the Eulerian-mean velocity and the extra advection calculated here we call the Horizontal Residual Mean (HRM) velocity. The calculation of the extra advection is based on the depth-integrated horizontal transport from the seafloor to the density surface whose spatially averaged height is at the height of the calculation. Incorporating the HRM velocity into an ocean model improves the effective spatial resolution and the representation of poleward heat transport.

Declaration relating to disposition of project thesis/dissertation

I hereby grant to the University of New South Wales or its agents the right to archive and to make available my thesis or dissertation in whole or in part in the University libraries in all forms of media, now or here after known, subject to the provisions of the Copyright Act 1968. I retain all property rights, such as patent rights. I also retain the right to use in future works (such as articles or books) all or part of this thesis or dissertation.

I also authorise University Microfilms to use the 350 word abstract of my thesis in Dissertation Abstracts International (this is applicable to doctoral theses only).

31/08/2017

Signature

Witness Signature

Date

The University recognises that there may be exceptional circumstances requiring restrictions on copying or conditions on use. Requests for restriction for a period of up to 2 years must be made in writing. Requests for a longer period of restriction may be considered in exceptional circumstances and require the approval of the Dean of Graduate Research.

FOR OFFICE USE ONLY

Date of completion of requirements for Award:

ORIGINALITY STATEMENT

'I hereby declare that this submission is my own work and to the best of my knowledge it contains no materials previously published or written by another person, or substantial proportions of material which have been accepted for the award of any other degree or diploma at UNSW or any other educational institution, except where due acknowledgement is made in the thesis. Any contribution made to the research by others, with whom I have worked at UNSW or elsewhere, is explicitly acknowledged in the thesis. I also declare that the intellectual content of this thesis is the product of my own work, except to the extent that assistance from others in the project's design and conception or in style, presentation and linguistic expression is acknowledged.'

Signed

Date

COPYRIGHT STATEMENT

'I hereby grant the University of New South Wales or its agents the right to archive and to make available my thesis or dissertation in whole or part in the University libraries in all forms of media, now or here after known, subject to the provisions of the Copyright Act 1968. I retain all proprietary rights, such as patent rights. I also retain the right to use in future works (such as articles or books) all or part of this thesis or dissertation.

I also authorise University Microfilms to use the 350 word abstract of my thesis in Dissertation Abstract International (this is applicable to doctoral theses only).

I have either used no substantial portions of copyright material in my thesis or I have obtained permission to use copyright material; where permission has not been granted I have applied/will apply for a partial restriction of the digital copy of my thesis or dissertation.'

Signed

Date 31/08/2017

AUTHENTICITY STATEMENT

'I certify that the Library deposit digital copy is a direct equivalent of the final officially approved version of my thesis. No emendation of content has occurred and if there are any minor variations in formatting, they are the result of the conversion to digital format.'

Date 31/08/2017

Acknowledgements

First and foremost, I would like to express my greatest appreciation to my primary supervisor Professor Trevor McDougall. Trevor's unconditional support has not only been invaluable to my academic life throughout my graduate studies, but also of great importance in every aspect of my life. Academically, Trevor's extensive knowledge, insightful opinions and thoughtful advice and encouragement have played an important role in building up my research and overcoming difficulties in my studies. In addition to numerous illuminating discussions, his great patience, positive attitude and enthusiasm have also contributed to the research contained in this thesis. Moreover, I highly appreciate his encouragement for me to attend conferences, winter schools and a research voyage, from which I have broadened my horizons and gained unique experiences. I would like to thank him sincerely for providing such an enlightening and educational research experience. Furthermore, Trevor has been a marvellous life mentor to me. The life experiences and light-hearted jokes he has kindly shared with me have brought joy and laughter to my life and helped me overcome difficult times. Working with him was one of the most pleasant experiences of my life. I am greatly indebted to Trevor for his priceless help during the pursuit of my goals.

During my study, my co-supervisors Dr. Shane Keating and Professor Matthew England have offered crucial help to my research. I would like to thank Shane for his brilliant suggestions on my work. In addition, he has set a great example for me to learn scientific communication and collaboration skills. I am very grateful to have Matthew as my co-supervisor. He has been a resourceful mentor. Thanks to him, I have had the opportunities to work with and learn from researchers in climate science.

My sincere thanks also go to Dr. Casimir de Lavergne for helping me complete my work with great patience. Casimir is remarkably astute. As a quick thinker, he has been always ready to help and able to shed light on my questions. I also thank Dr. Nicholas Hannah for his unstinting support with ocean modelling. His outstanding computer skills were critical to my research.

I thank Professor Gurvan Madec for his invaluable opinions on my work. Even though we have met for only a short time, his input to interpret the Horizontal Residual Mean theory has been highly appreciated. People I have worked with are all great researchers and I look forward to working with all of them in the future.

My dear family has always been unconditionally supportive. I cannot be who I am today without their love. Even if every flower in the world had a voice, I could not send as many as it would take to express my gratitude enough.

My sincerest gratitudes are extended to all my friends, for them always being on my side, for their understanding, support and encouragement. From the bottom of my heart, I thank Tim, Houying, Yuanze and Lifei for spending time to help me in writing this thesis and being remarkably forbearing. Without Chiyue, Xinglan, Yunqi, Juan and Hongjin comforting and heartening me, I would never have survived this bumpy journey. Their help is worth more appreciation than I can express on paper. Also, the company of all my friends, especially Chanikarn, Yanyan, Ali, Jun, Jinghao, Mengzhe, Huan and Ricky, is very meaningful to me. Last but not least, a big shout-out to fellow PhD students and postdocs for making the workplace a comfortable place to work and have fun.

Abstract

Salt and heat are two ocean properties of vital importance. Their mean distribution, their advective transport and their diffusive redistribution control ocean dynamics by setting the density of seawater and its spatio-temporal variability. In this thesis, we investigate two aspects of the mixing and transport of salt and heat: the role of double diffusion, a consequence of the slower molecular diffusion of salt relative to heat; and the impact of small-scale density gradients on the poleward heat transport of the ocean.

In the first part of this thesis, double-diffusive interleaving is examined as it progresses from a linear instability towards finite amplitude. We examine the finger and diffusive instability types and ask whether a steady state is possible. We find that the strength of the fluxes across the diffusive interfaces must be many times stronger relative to the corresponding fluxes across the finger interfaces than is indicated from existing flux laws as derived from laboratory experiments. The total effect of the interleaving motion on the vertical fluxes of heat and of salt is calculated for the steady-state solutions. It is found that both the fluxes of heat and salt are up-gradient, corresponding to negative vertical diffusion coefficients for heat, salt and density.

The remainder of the thesis addresses the limited spatial resolution of ocean models. Unresolved spatial correlations between horizontal velocity and tracer fields contribute to the actual horizontal fluxes of heat and other scalar quantities but are not accounted for by state-of-the-art ocean models. A method of estimating these unresolved fluxes is proposed, based on calculating an additional non-divergent velocity to advect all scalar variables. The sum of the Eulerian-mean velocity and the extra advection calculated here we call the Horizontal Residual Mean (HRM) velocity. The calculation of the extra

advection is based on the depth-integrated horizontal transport from the seafloor to the density surface whose spatially averaged height is at the height of the calculation. Incorporating the HRM velocity into an ocean model improves the effective spatial resolution and the representation of poleward heat transport.

Contents

Acknowledgements	i
Abstract	iii
List of Abbreviations	xiii
List of Symbols	xiv
1 Introduction	1
2 Double Diffusive Interleaving: Properties of the Steady-State Solution	14
2.1 Introduction	14
2.2 The model equations	18
2.3 The transition to finite amplitude in the finger-finger (FF) regime . . .	26
2.4 The integration in the finger-nondouble-diffusive (FN) regime	27
2.5 The integration in the finger-diffusive (FD) regime	28
2.6 The feasibility of the steady state	29
2.7 The relations among variables in the steady state	37
2.8 The diapycnal fluxes at steady state	42
2.9 Discussion	47
3 Horizontal Residual Mean: Addressing the Limited Spatial Resolution of Ocean Models	52
3.1 Introduction	52
3.2 Expressions for the extra non-divergent advection of HRM	56

3.2.1	The expression of McDougall (1998) for the HRM streamfunction	56
3.2.2	Estimating the HRM streamfunction from coarse-resolution model fields	60
3.3	Assessment of the method using 1/4-degree model snapshot	66
3.3.1	Gulf Stream	67
3.3.2	East Australian Current	68
3.3.3	Antarctic Circumpolar Current	69
3.3.4	The dominance of the horizontal shear term compared with the vertical shear term	71
3.4	The HRM contribution to meridional overturning	79
3.5	The HRM contribution to the horizontal heat transport	80
3.6	Tapering of the quasi-Stokes HRM streamfunction	84
3.7	HRM implementation in ocean models	86
3.8	Conclusions	91
4	Conclusions	95
A	DDI: The Linearly Unstable Solutions	102
B	DDI: Initial Conditions	104
C	DDI: The Laboratory Flux Laws	105
D	DDI: The Finger Flux Divergence in the FF Regime	106
E	DDI: The Relationship between the Steady-State Value X^s, Y^s and a^s	108
F	HRM: Evaluation of the Left-hand Side of Equation 3.8	109
	Bibliography	114

List of Figures

- 2.1 The sketch at the left is a vertical cross section through the frontal region showing the direction of cross-frontal motion of the intrusions and their slopes. The interfaces with vertical short lines represent the dominant finger interfaces. On the right-hand side, the two graphs show the Absolute Salinity and the density profiles at position A. The dashed lines indicate the initial state without perturbations, and the full lines show the profiles at a later stage. 15
- 2.2 Conservative Temperature - Absolute Salinity diagram showing the evolution of the properties of the double-diffusive intrusions with time. The initial properties lie on the dashed line with slope $R_\rho \equiv \alpha \bar{\Theta}_z / \beta \bar{S}_{A_z}$. The arrowed lines connect the initial and final points of several layers. . . . 16
- 2.3 Absolute Salinity - Conservative Temperature diagram showing the evolution of the subservient finger interface between layers a and b. From a to 1, it is a finger interface and then from 1 to 2 is a non-double-diffusive interface. At last, from 2 to 3 is a diffusive interface. In the steady state, a diffusive interface exists between points 3 on this diagram. 17
- 2.4 Contributions to the temporal derivative vector $(\alpha \Theta_t, \beta S_{At})$ from the double-diffusive fluxes and the advective terms. (a) The stage from points a to 1 in Fig. 2.3; this is the growing solution of the linear stability analysis of McDougall (1985a). (b) A sketch of the terms applying at the points 2 of Fig. 2.3. (c) Beyond points 2, the diffusive fluxes begin to grow and allow the possibility of a steady state solution in which $(\alpha \Theta_t, \beta S_{At})$ is (0,0). 33

- 2.5 Contours of the nondimensional salinity and temperature variables X^s and Y^s of the steady state points with respect to the exaggeration factor and R_ρ . Three values for Prandtl number are selected: (top two) $\sigma = 0.3$, (middle two) $\sigma = 1$ and (bottom two) $\sigma = 10$ 34
- 2.6 (top) A typical evolution of the nondimensional salinity and temperature variables X and Y towards the steady-state values at the end of the hook near the upper right-hand of the figure. (bottom) The loci of seven artificially perturbed points around the steady state point. These two panels are for the exaggeration factor $ef = 25$, $R_\rho = 2.5$ and $\sigma = 1$. . . 35
- 2.7 The stability ratios of the (top) diffusive and (bottom) finger interfaces at the steady state for $\sigma = 1$ 36
- 2.8 The upper panel of each pair shows the absolute value of the ratio of the vertical flux of salt across the diffusive interface to that across the finger interface in the steady state. The lower panel of each pair shows the absolute value of the ratio of the vertical flux of temperature across the diffusive interface to that across the finger interface in the steady state. Three values for Prandtl number are selected: (a) $\sigma = 0.3$, (b) $\sigma = 1$ and (c) $\sigma = 10$ 40
- 2.9 Values of γ_{diff}^s for the case of $\sigma = 1$ 41
- 2.10 Values of the ratio \hat{B}^s/\hat{B} for the case of $\sigma = 1$ 41
- 2.11 The values of the total diapycnal fluxes in terms of F_f^{SAs} . These panels are plots of equations 2.57 and 2.58 and the values are substantially negative. Three values for Prandtl number are selected: (a) $\sigma = 0.3$, (b) $\sigma = 1$ and (c) $\sigma = 10$ 46
- 2.12 The ratio $\alpha\text{TDF}\Theta/(R_\rho\beta\text{TDFS})$, being the ratio of the negative effective vertical diffusion coefficient for temperature to that for salt. This is the ratio of the numbers in the two panels in Fig. 2.11, divided by R_ρ . Three values of the Prandtl number are selected: (a) $\sigma = 0.3$, (b) $\sigma = 1$ and (c) $\sigma = 10$ 51

- 3.1 An illustration of the different height variables in equations 3.1 and 3.2. The curved line shows a snapshot of the instantaneous height of a density surface, which is denoted as $z_a(x, t)$ [see 3.2]. $\bar{z}_a(x)$ is illustrated by the straight blue line. $\langle \bar{z}_a \rangle$ is the average height of $\bar{z}_a(x)$, namely the temporal and spatial average of the instantaneous density surface $z_a(x, t)$. 57
- 3.2 Vertical cross-section through three boxes of a coarse-resolution ocean model, with the central box showing three boxes of a finer resolution ocean model that has three times the horizontal resolution compared with the coarse resolution model. At the fine resolution boxes, density surfaces follow the lines from the central point to the small dots at points. The small dots mark intersects of the density surfaces and the tracer casts. At the coarse-resolution, density surfaces follow the lines from the central point to the larger dots. The large dots mark intersects of density surfaces and the tracer casts. The corresponding heights of intersects are denoted z_W for the western intersect and z_E for the eastern intersect. \bar{v}_W , \bar{v}_E , \bar{v}_{upper} and \bar{v}_{lower} are averaged velocities on the vertical and zonal directions, respectively. The velocities available in the model are originally on vertices of grid boxes. $\langle \bar{z}_a \rangle$ is the height that tracers are at and δz is the difference between the average height of density surfaces and $\langle \bar{z}_a \rangle$ 62
- 3.3 Fine-resolution current speeds of the Gulf Stream area at a depth of 414 m are shaded. Velocity arrows are overlain every three grid points. . . 68
- 3.4 Comparison of the transports (in Sv; $1 \text{ Sv} = 10^6 m^3 s^{-1}$) calculated by the two methods at three different latitudes and five different depths in the Gulf Stream region. Red curves correspond to the two-triangle method of Appendix F which uses the high-resolution data, while the blue curves correspond to the right-hand side of equation 3.13 applied to the coarse-resolution fields. The x -axis is the number of coarse-resolution grid boxes from the coast. 69

- 3.5 Scatter plot of transports calculated by the two methods at different latitudes from about $32^{\circ}N$ to $39^{\circ}N$ and different depths from about 382m to 1320m, in the Gulf Stream. On the x -axis is the high-resolution estimate of the streamfunction (the left-hand side of equation 3.13) and on the y -axis is the low-resolution estimate (the right-hand side of equation 3.13). The colorbar indicates the depth of the calculated transport in meters. 70
- 3.6 Fine-resolution current speeds of the East Australian Current area at a depth of 414 m are shaded. Velocity arrows are overlain every three grid points. 71
- 3.7 Comparison of transport calculated by two methods at three different latitudes and five different depths in the East Australia Current. Red curves correspond to the two-triangle method of Appendix F which uses the high-resolution data, while the blue curves correspond to the right-hand side of equation 3.13 applied to the coarse-resolution fields. The x -axis is the number of coarse-resolution grid boxes from the coast. . . . 72
- 3.8 Scatter plot of transports calculated by the two methods at different latitudes from about $22^{\circ}S$ to $30^{\circ}S$ and different depths from about 382m to 1320m, in the East Australian Current. On the x -axis is the high-resolution estimate of the streamfunction (the left-hand side of equation 3.13) and on the y -axis is the low-resolution estimate (the right-hand side of equation 3.13). The colorbar indicates the depth of the calculated transport in meters. 73
- 3.9 Fine-resolution current speeds in a region of the Antarctic Circumpolar Current at 414 m depth are shaded. Velocity arrows are overlain every three grid points. 74

3.10	Comparison of the transport estimates in the (a) meridional and (b) zonal directions, calculated by two methods at three different latitudes and five different depths in the Antarctic Circumpolar Current. Red curves correspond to the high-resolution estimate of the transport, while blue curves correspond the low-resolution estimate. The x -axis is number of coarse-resolution grid boxes, taken as 1 to 5 starting from the coastline for all locations.	75
3.11	Scatter plot of transports calculated by the two methods in the (a) meridional and (b) zonal directions at different latitudes from about $58^\circ S$ to $60^\circ S$ and different depths from about 382m to 1320m, in the Antarctic Circumpolar Current. The x -axis is the high-resolution estimate of the streamfunction and the y -axis is the low-resolution estimate, The colorbar indicates the depth of the calculation in meters.	76
3.12	The first term (the horizontal shear term) of the right-hand sides of equations 3.13 (meridional) and 3.14 (zonal) is plotted on the x -axis, with the full right-hand sides of these equations plotted on the y -axis of these figures.	77
3.13	The first term (the horizontal shear term) of the right-hand sides of equations 3.13 (meridional) and 3.14 (zonal) is plotted on the x -axis, with the full right-hand sides of these equations plotted on the y -axis of these figures.	78
3.14	The meridional overturning streamfunction of the HRM quasi-Stokes velocity in z -coordinates.	79
3.15	The values of $\rho_0 c_p^0 \sum_{i=1}^N \Theta_i \Psi_{HRM,i} - \Psi_{HRM,i+1} $ in the region of the Gulf Stream, in units of PW. The underlying color indicates the total amount of depth-integrated heat flux in each grid box, which is the absolute value of magnitude of the heat flux. The white arrows show the directions. . .	82
3.16	The quasi-Stokes HRM zonally- and depth-integrated meridional heat transport.	83
3.17	An example of outcropping locally-referenced neutral tangent plane in which the effective height (the red dot) is below the sea surface. . . .	85

- 3.18 An illustration of outcropping case where the effective height (the red dot) is also above sea surface. 85
- 3.19 Two ways of calculating HRM transport have been compared in the GS and EAC areas. Both meridional and zonal HRM transports in these three areas are compared. The x -axis gives HRM transports calculated by using the ratio of locally-referenced potential density gradients. The y -axis presents the HRM transport calculated by the heights of neutral tangent planes calculated using all the information of vertical casts. The color indicates the depths and colorbar shows the depths in meters. . . . 89
- 3.20 Two ways of calculating HRM transport have been compared in the ACC area. Both meridional and zonal HRM transports in these three areas are compared. The x -axis gives HRM transports calculated by using the ratio of locally-referenced potential density gradients. The y -axis presents the HRM transport calculated by the heights of neutral tangent planes calculated using all the information of vertical casts. The color indicates the depths and colorbar shows the depths in meters. . . . 90
- F.1 Vertical cross-section through three boxes of a coarse-resolution ocean model, with the central box showing three boxes of a finer resolution ocean model that has three times the horizontal resolution compared with the coarse resolution model. For the fine resolution boxes, the slopes of the density surfaces are given by the lines from the central point to the dots at points on the fine-scale grid boxes, while for the coarse-resolution data the slopes of the density surfaces are determined by the lines from the central point to the other two dots at the centre (horizontally) of the coarse-resolution boxes. 110
- F.2 The three-dimensional view of two-triangle calculation for transports. . . 112

List of Abbreviations

ACC	Antarctic Circumpolar Current
DDI	Double Diffusive Interleaving
EAC	East Australian Current
FD	finger-diffusive
FF	finger-finger
FN	finger-nondouble-diffusive
GM	Gent and McWilliams (1990) scheme
GS	Gulf Stream
HRM	Horizontal Residual Mean
MOM	Modular Ocean Model
PW	petawatts
TDFS	total diapycnal flux of salt
TDFΘ	total diapycnal flux of Conservative Temperature
TEOS10	Thermodynamic Equation of Seawater 2010
TRM	Temporal Residual Mean

List of Symbols

α	thermal expansion coefficient of seawater defined by $\alpha = -\rho^{-1}(\partial\rho/\partial\Theta) _{p,S_A}$
β	saline contraction coefficient of seawater defined by $\beta = \rho^{-1}(\partial\rho/\partial S_A) _{p,\Theta}$
γ	locally-referenced potential density
γ_f	buoyancy flux ratio of finger interfaces, fixed at 0.5 throughout this paper
γ_{diff}	buoyancy flux ratio of diffusive interfaces
γ_{diff}^S	buoyancy flux ratio of diffusive interfaces at steady state
γ_x	density gradient in x direction
γ_y	density gradient in y direction
γ_z	density gradient in z direction
$\bar{\gamma}_z$	density gradient in z direction for temporal mean density
$\eta'_a(x, t)$	perturbation height of density surface
Θ	conservative Temperature [IOC et al. (2010)]
Θ_l	the gradient of Conservative Temperature in the direction of motion of an intrusion (or leaf)
κ	diffusivity
$\hat{\lambda}$	the growth rate
ν	viscosity
ρ_0	seawater density taken to be $1030 \text{ kg} \cdot \text{m}^{-3}$
σ	Prandtl number
$\bar{\phi}$	half the density variance at z , with $\bar{\phi} \equiv \frac{1}{2}\overline{(\gamma')^2}$
Ψ^x	the eastward Eulerian-mean streamfunction
Ψ^y	the northward Eulerian-mean streamfunction

Ψ_{HRM}^x	the eastward quasi-Stokes HRM streamfunction
Ψ_{HRM}^y	the northward quasi-Stokes HRM streamfunction
Ψ_{TRM}^x	the eastward quasi-Stokes TRM streamfunction
Ψ_{TRM}^y	the northward quasi-Stokes TRM streamfunction
Ψ_{Total}^x	the eastward quasi-Stokes streamfunction
Ψ_{Total}^y	the northward quasi-Stokes streamfunction
a^s	the absolute value of the ratio of the vertical flux of salt across the diffusive interface to that across the finger interface in steady state
\hat{B}	the proportionality constant between the salt flux across a finger interface and the salinity difference across the interface
\hat{B}^S	the proportionality constant between the salt flux across a finger interface and the salinity difference across the interface at steady state
c_p^0	the constant value of the specific heat at constant pressure
\hat{D}	the flux coefficient of momentum
D_0	the initial flux coefficient of momentum
D^{SS}	the flux coefficient of momentum at steady state
F^x, F^y, F^z	the fluxes of x, y, z momentum
F^{SA}, F^{Θ}	the fluxes of Absolute Salinity and Conservative Temperature
h	the vertical wavelength of the intrusions, being twice the thickness of a single intrusion
$-H$	the height of sea floor
L^x	the mean slope of the locally-referenced potential density surface in the x direction
L_E^x	the mean slope of the locally-referenced potential density surface in the x direction to the east of the tracer point
L_W^x	the mean slope of the locally-referenced potential density surface in the x direction to the west of the tracer point
L^y	the mean slope of the locally-referenced potential density surface in the y direction
L_N^y	the mean slope of the locally-referenced potential density surface in the y direction to the north of the tracer point
L_S^y	the mean slope of the locally-referenced potential density surface in the y direction to the south of the tracer point

N	buoyancy frequency
R_ρ	environmental stability ratio
R_ρ^f	stability ratio of “finger” interface
R_ρ^{diff}	stability ratio of “diffusive” interface
S_A	Absolute Salinity [(IOC et al., 2010)]
S_{A_l}	the gradient of Absolute Salinity in the direction of motion of an intrusion (or leaf)
\bar{u}	the temporally averaged zonal velocity
\bar{u}_0	the Eulerian mean zonal velocity at $x = 0$ and $z = \langle \bar{z}_a \rangle$
\bar{u}_y	the meridional shear of the temporally averaged zonal velocity
\bar{u}_z	the vertical shear of the temporally averaged zonal velocity
$\langle \bar{u} \rangle$	the resolved-scale Eulerian zonal velocity
$\langle \bar{u} \rangle_x$	the zonal shear of the resolved-scale Eulerian zonal velocity
$\langle \bar{u} \rangle_z$	the vertical shear of the resolved-scale Eulerian zonal velocity
\bar{u}_N	the vertically averaged zonal velocity to the north of a tracer point
\bar{u}_S	the vertically averaged zonal velocity to the south of a tracer point
\bar{u}_{upper}	the meridionally averaged zonal velocity above a tracer point
\bar{u}_{lower}	the meridionally averaged zonal velocity below a tracer point
u'	perturbation of zonal velocity
\bar{v}	the temporally averaged meridional velocity
\bar{v}_0	the Eulerian mean meridional velocity at $x = 0$ and $z = \langle \bar{z}_a \rangle$
\bar{v}_x	the zonal shear of temporally averaged meridional velocity
\bar{v}_z	the vertical shear of temporally averaged meridional velocity
$\langle \bar{v} \rangle$	the resolved-scale Eulerian meridional velocity
$\langle \bar{v} \rangle_x$	the zonal shear of the resolved-scale Eulerian meridional velocity
$\langle \bar{v} \rangle_z$	the vertical shear of the resolved-scale Eulerian meridional velocity
\bar{v}_E	the vertically averaged meridional velocity to the east of a tracer point
\bar{v}_W	the vertically averaged meridional velocity to the west of a tracer point
\bar{v}_{upper}	the zonally averaged meridional velocity above a tracer point
\bar{v}_{lower}	the zonally averaged meridional velocity below a tracer point

v'	perturbation of meridional velocity
w'	perturbation of vertical velocity
X	non-dimensional salinity perturbation variable defined as $X = (2\beta S') / (\frac{1}{2}h\beta\bar{S}_{A_z})$
Y	non-dimensional temperature perturbation variable defined as $Y = (2\alpha\Theta') / (\frac{1}{2}h\beta\bar{S}_{A_z})$
$z_a(x, t), z_a(y, t)$	the instantaneous height of a density surface
$\langle \bar{z}_a \rangle$	the spatially and temporally averaged height of the locally-referenced potential density surface
$\bar{z}_a(x), \bar{z}_a(y)$	temporal average of $z_a(x, t)$ and $z_a(y, t)$, respectively
z_E	height of the density surface at the eastern cast of the target tracer point
z_N	height of the density surface at the northern cast of the target tracer point
z_S	height of the density surface at the southern cast of the target tracer point
z_W	height of the density surface at the western cast of the target tracer point
Δx	the zonal scale of grid box
Δy	the meridional scale of grid box
Δz	the vertical scale of grid box
δz	the height difference between average height of the neural density surface and the height being considered

Chapter 1

Introduction

The ocean is profoundly affected by the presence of small-scale thermohaline structures. The mean distribution, advective transport and diffusive redistribution of temperature and salinity control ocean dynamics by setting the density of seawater and its spatio-temporal variability. The general circulation of the oceans is primarily forced at large scales, by surface wind and buoyancy forcing as well as tidal forces and geothermal heating. Yet a cascade of energy from the $O(10^6 m)$ scales of the forcing to the $O(10^{-2} m)$ scales of the dissipation must keep the circulation in balance. The generation of small-scale property gradients is an integral aspect of this energy cascade and, ultimately, a key regulating factor of the circulation. At the small scale, temperature and salinity gradients set the rate of irreversible mixing and the frictional dissipation of isotropic turbulence. At $O(1 - 100 m)$, they reflect dissipative processes such as the small-scale overturning of internal waves – the subsurface analogue of surface waves breaking on beaches – or double diffusive interleaving – a layering and mixing phenomenon related to the slower molecular diffusion of salt relative to heat. At $O(100 m - 1 km)$, thermohaline structure often arises from submesoscale fronts and their instabilities, which can extract energy from larger scales and catalyze its transfer to dissipative scales. At $O(1 - 100 km)$, temperature and salinity variance is largely the product of stirring by mesoscale eddies, which remain unresolved by most global ocean models employed for climate projections. Small-scale thermohaline structures are therefore ubiquitous and central to the momentum and energy balance of the ocean, but often difficult to observe and model. Understanding their physics and how they relate to the larger-scale

circulation is a major challenge for the understanding and modelling of the ocean's role in climate.

Both the mixing and transport of these two properties play crucial roles in the ocean. Diapycnal mixing - mixing across density surfaces - is a key process controlling the ocean stratification and meridional overturning. Recent observations indicate that diapycnal mixing is highly heterogeneous in the ocean, with weak mixing in much of the open ocean [Ledwell et al. (1993), Ledwell et al. (2011)] and much stronger mixing in the vicinity of rough topography [Ledwell et al. (2000)] and in frontal regions such as the Drake Passage [St. Laurent et al. (2012)]. More specifically, Ledwell et al. (2011) claimed that the diapycnal diffusivity in the ocean interior is on the order of $10^{-5} m^2 s^{-1}$ by analysing observational data, and St. Laurent et al. (2012) demonstrated that the magnitude of diapycnal mixing is largely amplified in the frontal regions in Drake Passage to the order of $10^{-4} m^2 s^{-1}$. Diapycnal mixing also contributes significantly to the overturning circulation of the deep ocean because mixing across density surfaces changes the density of seawater and hence enables it to rise or sink. For example, Melet et al. (2012) showed that there was a roughly 10% difference in the amplitude of the Indo-Pacific meridional overturning circulation between two tidal mixing parameterizations.

Given the vital role of small-scale thermohaline structures in the ocean, there is great interest in understanding the nature of these structures and evaluating their effects on large-scale ocean circulation. Typically, efforts have focussed on two main approaches: to better understand small-scale physical processes; and to capture the effects of unresolved small-scale dynamics on the resolved scale of ocean models. There is no clear distinction between these two approaches and often they are interwoven and complementary. Intuitively, refining the grid resolution can greatly improve an ocean model's ability to represent the mesoscale eddy field and accept parameterizations of subgridscale processes, at the cost of increased computational effort. However, increasing the resolution, though effective and important, is not sufficient. The process of refining model resolution must be accompanied by a proper and adjusted representation of newly resolved and still unresolved physical processes. As the resolution of ocean models steadily improves, there will be a continued need to parameterize unresolved

scales and physical processes for the foreseeable future.

The need to parameterize physical processes on unresolved scales is illustrated by double diffusive convection. Double diffusive convection is a type of diapycnal mixing caused by different rates of diffusion of two density-affecting water properties. In the ocean, these are temperature and salinity, both of which contribute to the water density but have molecular diffusivities that differ by two orders of magnitude. The molecular diffusivity of salt is two orders of magnitude smaller than that of heat. Double diffusive convection results in two distinct types of fluid motion, called the *salt finger* type and *diffusive* type, respectively. When hot saline water lies above cold fresh seawater, it sets up a salt finger type double diffusion because narrow fingers of fluid from the upper layer can lose more heat than salt and so become denser and then sink. The overlying water falls in the form of saline columns, hence named salt fingers. The diffusive type of double diffusion occurs when the cold fresh water overlies warm salty water. This type of double diffusive convection exhibits sharp quasi-horizontal interfaces. Double diffusive processes not only re-distribute the temperature and salinity fields in the ocean, but also affect the distribution of other chemical and microbial components. Therefore, it has been considered an important oceanographic process. However, there are still significant gaps in our understanding of double diffusive mixing processes and their representation in ocean models.

After Stern (1960) introduced double diffusion into oceanographic research, double diffusive convection and the associated small-scale thermohaline structures has been found to be ubiquitous in the ocean and is suspected to be important for ocean dynamics. Persistent staircases developed by double diffusive convection of salt and heat have been well documented in the Tyrrhenian Sea within the Mediterranean [Johannessen and Lee (1974), Zodiatis and Gasparini (1996)], in the eastern North Atlantic [Tait and Howe (1968)], and in the western tropical North Atlantic [Mazeika (1974), Boyd and Perkins (1987), Boyd (1989), Schmitt et al. (1987)]. The existence of fine-scale thermohaline interleaving at ocean fronts has been reported as well. Joyce et al. (1978) and Toole (1981) reported double diffusive intrusions in the Antarctic polar front. The similar structure has been observed at mid-latitudes by Gregg and McKenzie (1979) and Gregg (1980). Williams (1981) reported active double diffusive intrusions in the

Gulf Stream using his shadowgraph device, and Schmitt and Georgi (1982) also found strong intrusions in the North Atlantic Current. The ubiquitous occurrence of these fine-scale thermohaline structures indicates that they are important factors in estimating the fluxes and the budgets of heat and salt. The distinct role of double diffusive mixing in the ocean is now well recognized in oceanography.

Abundant observational evidence has motivated efforts to deepen understanding of these processes. Significant progress has come from laboratory experiments and theoretical analysis. Interestingly, the first known laboratory experiment was done about one hundred years before Stern (1960) introduced double diffusive convection into oceanic research. Jevons (1857) performed a heat-sugar double diffusive experiment and correctly attributed the phenomenon to the difference in the diffusivities of heat and sugar. Turner (1965) first investigated the transfer of heat and salt fluxes across a diffusive interface. Huppert (1971) employed Turners results to a series of diffusive interfaces and obtained flux laws of heat and salt for double diffusive interfaces. Other variant experiments had general agreement with Hupperts findings. For example, Marmorino and Caldwell (1976) investigated a wider range of heat fluxes, as low as observations in parts of the ocean. The measurements of interfacial heat flux agreed with Hupperts flux laws. Turner (1967) and Schmitt (1979) showed how the salt flux varied as the $4/3$ power of the salinity difference in two-layer tank experiments. Laboratory fluxes laws found by McDougall and Taylor (1984) was used for fluxes across the finger interface, as summarized in Appendix C, together with Hupperts fluxes law. Detailed reviews on several aspects of double diffusive convection are available from Schmitt (1994), Ruddick and Gargett (2003) and Kunze (2003).

Numerical models are mathematical equations operated by numerical time-stepping procedures. Adjusting assumptions and parameters of a numerical model frees researchers from limitations of theory and observation and allows researchers to comprehensively understand and mimic the real world. Numerical modelling studies have also shed light on the impact of double diffusive processes on the large-scale ocean circulation. Gargett and Holloway (1992) have made the first attempt at estimating the impact from implementing unequal diffusivities for heat and salt in a numerical model. The results suggest that the magnitude and sense of the thermohaline circula-

tion, and the water mass characteristics of intermediate and deep water are all sensitive to the unequal diffusivities of heat and salt. The different diffusivities resulted in noticeable differences in meridional transports because the ocean was forced into different advective-diffusive equilibriums which involve the upgradient buoyancy flux. They also emphasised that it was the diffusivity ratio that governs the steady-state characteristics of coarse resolution models, rather than the particular choice of each diffusivity. Following their work, Zhang et al. (1998) demonstrated the sensitivity of numerical models to the double diffusive parameterizations by comparing results from three numerical experiments. The double-diffusive parameterization of Zhang et al. (1998) lessened the meridional overturning rate by 22% compared to the constant diffusivity parameterization for the small-scale mixing processes and by 10% the amount in Gargett and Holloway (1992). Their work proved that different parameterization of double diffusive convection can result in sizeable changes in numerical models' meridional overturning circulation. These sensitivity tests suggest that more research in understanding double diffusive processes is required.

Numerical models aim to simulate the real ocean as accurately as possible, yet small-scale structures are never fully resolved by numerical models. The resolution of models can prohibit the inclusion of processes that have smaller scales than the model grid box. The contribution of these small-scale structures is thus inadequately calculated or omitted by the model. For example, the spatial scale of salt fingers is so small (order 0.01m) compared with the size of grid boxes in global ocean models that they are usually not resolved and have to be parameterized in numerical models.

Rintoul and Wunsch (1991) have discussed the importance of the unresolved subgrid-scale processes by comparing the differences between estimates of circulation from a series of inverse models. These authors found that the unresolved spatial correlations in some models significantly changed the estimates of tracer fluxes. Fanning and Weaver (1997) conducted a horizontal resolution sensitivity study of the heat transport in a coupled climate model. The results of their simulations showed that the atmospheric heat transport is decreased to counteract the increase in oceanic heat transport. The ocean heat transport due to the baroclinic gyre transport was enhanced by a factor of 5 from the 4 degree to the 1/4 degree resolution. Their results point to limitations

inherent in simulating the real ocean due to the resolution of ocean models. Penduff et al. (2010) simulated mean sea-surface heights and sea-level anomalies with the same model at 2, 1, 1/2 and 1/4 degree resolution. The comparison has shown that the model resolution has great influence on the global sea-surface variability pattern. Gulev et al. (2007) compared the estimates of water mass transformation in the North Atlantic between 1 degree and 1/6 degree ocean simulation with the identical configuration and analysed the noticeable differences in the surface transformation rates. They claimed that 1/6 degree high resolution provided adequate representation of eddies in the tropics and mid-latitudes and enhanced the process of water mass transformation compared to the 1 degree coarse resolution model. Interestingly, the higher resolution did not guarantee better ability of resolving eddies everywhere. They therefore urged more future developments on the understanding of the sensitivity of ocean models to model resolutions in various aspects. Another striking example is the work of Treguier et al. (2005) in which a quantitative comparison was made between high-resolution models in the North Atlantic subpolar gyre. The comparison demonstrated very different patterns of deep convection and also showed a large drift in watermass properties with a salinization in the Labrador Sea. It is clear that the resolution of models have profound influences on many aspects in ocean studies. Those sensitivity studies raised a consensus among oceanic researchers that capturing the effects of these unresolved small-scale structures is a persistent obstacle that needs to be overcome. Studies of Gulev et al. (2007) and Treguier et al. (2005) also exemplify that the resolution refining process must be accompanied by a proper and adjusted representation of the newly resolved and still unresolved physical processes. The continuous need to parameterize these motions for the foreseeable future will not vanish. To summarise, research on small-scale structures in the ocean should have high priority in oceanic and climate studies. Although many observational and theoretical studies have been made, a full understanding of these small-scale process still awaits further advancement in observational capabilities and theoretical models.

Along with limited horizontal resolution in ocean models goes the limited ability to resolve mesoscale eddy activity. Mesoscale eddies have typical horizontal scales of order 100km. Ocean models with a horizontal resolution of order 1 degree have almost no

ability to reproduce these mesoscale eddy motions, and even at $1/4$ degree resolution the mesoscale eddy activity is rather weak. Gent and McWilliams (1990) introduced a parameterization scheme for this mesoscale eddy activity that has since been widely adopted in the ocean modelling community. Our present understanding of this scheme for parameterizing mesoscale eddies owes much to the pioneering work of Andrews and McIntyre (1976) who formulated the zonal transformed Eulerian mean approach for use in the atmosphere. The separation of the flow into its zonal average and the deviations therefrom has been a dominant paradigm for analyses of the general atmospheric circulation. Since Eliassen and Palm (1961), residual-mean theory has provided an elegant framework with which to understand eddy-mean flow interaction. The basic idea of residual mean theory is that tracers are advected not by the Eulerian mean velocity, but by the “residual” velocity. The form of this residual velocity depends on the particular formalism. The residual mean concept has totally changed our understanding of the zonally integrated atmospheric circulation and has been extended to understand the effect of humidity [Stone and Salustri (1984)], to the use of isentropic coordinates [Andrews et al. (1987)], and to applications in the middle and upper troposphere [e.g. Trenberth (1986)].

Inspired by Andrews and McIntyre (1976), this residual-mean interpretation of the Gent and McWilliams (1990) parameterization scheme was extended to the oceanic case where the averaging is over time, and the velocity fields are three-dimensional [rather than the two-dimensional zonal-averaged case of Andrews and McIntyre (1976)]. Gent et al. (1995) quantified the effects of the Gent and McWilliams (1990) parameterization and found an eddy-induced meridional overturning streamfunction peaking at 18 Sv in the Antarctic Circumpolar Current. McDougall and McIntosh (2001) subsequently showed that the Gent and McWilliams (1990) parameterization of the eddy flux was in fact a parameterization of a type of residual circulation. McDougall and McIntosh (2001) argued that the Gent and McWilliams (1990) eddy parameterization scheme is essentially a parameterization of the quasi-Stokes velocity of the Temporal Residual Mean (TRM) circulation. Succinctly, TRM applied a temporal and thickness-weighted averaging procedure in which both the scalar variables and the velocity components become the thickness-weighted isopycnal versions. The horizontal component of the

TRM velocity is the sum of the Eulerian mean velocity and a velocity that accounts for the contribution of eddies to the horizontal flux of fluid below a certain density surface. This TRM horizontal velocity is equivalent to the thickness-weighted mean velocity in density coordinates. In other words, Gent and McWilliams (1990) includes the eddy-induced horizontal density flux due to unresolved *temporal* correlations between temperature (or salinity) and the horizontal velocity. It remains a primary challenge and demand of coarse-resolution ocean models to understand and quantify the effects of vital properties (such as salinity and temperature) advected with the residual mean velocities.

In this thesis, we focus on two specific aspects of small-scale thermohaline structures: the implications of double diffusive mixing, and the impact of limited spatial resolution on horizontal tracer transports. We first examine double diffusive interleaving and its finite-amplitude equilibration. This work extends the analysis of Toole and Georgi (1981), who constructed a model of double-diffusive interleaving for infinitesimal perturbations using linear stability analysis and showed that these quasi-horizontal intrusions can be driven by the vertical buoyancy fluxes of double-diffusive convection. In their studies, the vertical profiles are smooth, continuous functions of the vertical coordinate, with the vertical structure function being harmonic and the nonlinear advection terms turning out to be zero. McDougall (1985a) showed that the same growing intrusions occurred whether the environment was rotating or not, and McDougall (1985b) made a start at studying these interleaving motions at finite amplitude. He showed that it was feasible that steady-state balances could be achieved for both heat and salt. Building on McDougall's work, our study assumes an intrusion structure with sharp interfaces as being more consistent with ocean observations than the harmonic vertical structure.

The flux laws found in laboratory experiments opened the opportunity to show if such steady-state balances could be achieved with the fluxes across the double-diffusive interfaces taken from those laboratory flux laws. The laboratory-based law of the diffusive fluxes of heat and salt is taken from Huppert (1971) and the fluxes in the salt fingering case described by the expression found by McDougall and Taylor (1984). In this thesis, a finite-amplitude model of double-diffusive interleaving is formed by

integrating the temperature and salinity equations of each intrusion forward in time using the Runge-Kutta integration technique. Each layer is taken to be well-mixed in the vertical, separated by relatively sharp interfacial regions where the double-diffusive fluxes originate. The vertical length scale of the intrusions, and their slope with respect to the isopycnals are taken from the linear stability analysis.

Following McDougall (1985a), there are three regimes as the intrusions evolve: firstly each interface is of the “finger” type. In the linear stability analysis, each alternative finger interface grows at the expense of its neighbor. We start our model with a small (but finite) disturbance and the model allows the interleaving motions to grow to finite amplitude thereafter using realistic flux laws while still in this “finger-finger” regime. This stage is followed by a stage where each alternate interface ceases to be a finger interface and instead becomes stably stratified in both temperature and salinity. A third stage follows in which each alternative interface becomes of the “diffusive” type in which cool fresh water overlies warmer saltier fluid. Ultimately, the system can reach a steady state and the properties of the relations among variables in the steady state are examined. Combining the theoretical and laboratory work further revealed the condition for double diffusive intrusions to achieve an equilibrium and gave implications in modelling double diffusive interleaving structure.

The remainder of the thesis aims at estimating unresolved spatial correlations due to the limited spatial resolution of an ocean model with the aim of deliberately injecting the induced transports into an ocean model. The ocean models have first been developed in z -coordinates. The z -coordinate ocean models have been conventional and are still in active use nowadays. However, ocean models in isopycnal coordinates have gained popularity because researchers have widely accepted that the stirring and mixing of tracers by mesoscale eddies mainly happen along locally-referenced potential density surfaces [Griffies (2004); McDougall and Jackett (2005) and McDougall et al. (2014)]. The widely adopted Gent and McWilliams (1990) parameterization for mesoscale eddies was originally motivated in isopycnal coordinates. These authors realized that the epineutral diffusion of scalars would be affected by lateral variations of the thickness between pairs of closely spaced isopycnals, and they proposed a parameterization that acted as a sink of gravitational potential energy via the diffusion of this thickness. At

first, it seemed that the Gent and McWilliams (1990) scheme was a diffusive process because the coefficient in the extra advection of tracers was called the “thickness diffusivity” and it caused a diapycnal transport. In hindsight, the clearest description is that the Gent and McWilliams (1990) scheme is a representation of an extra eddy-induced advection by a three dimensional non-divergent velocity [Gent (2011)]. McDougall and McIntosh (2001) showed that the Gent and McWilliams (1990) parameterization scheme essentially represents the horizontal density flux due to unresolved temporal correlations between temperature (or salinity) and the horizontal velocity, and it can be understood as a parameterization to arrive at the residual-mean velocity in an ocean model. It had long been recognized that tracers (including temperature and salinity) are not advected by the Eulerian-mean velocity, and Gent et al. (1995) showed that the Gent and McWilliams (1990) scheme was in fact an extra velocity that advects temperature and salinity.

McDougall and McIntosh (2001) then provided a physical interpretation of this extra quasi-Stokes velocity field; namely that it is the contribution of eddies to the transport of seawater that is denser than the appropriately averaged density at the point in question. This physical interpretation and a Taylor series expression for the perturbation velocities and perturbation tracers showed that the streamfunction of Gent and McWilliams (1990), when added to the Eulerian-mean streamfunction, actually transports tracers in the same manner as would an eddy-resolving model, and that the horizontal residual velocity is actually the thickness-weighted horizontal velocity obtained by temporally averaging in density coordinates. McDougall and McIntosh (2001) named their work temporal residual mean (TRM) theory following the common concept of residual mean circulation in atmospheric studies, more specifically Andrews and McIntyre (1976). Notice that the TRM conducts temporal averaging rather than the zonal averaging in Andrews and McIntyre (1976). Before this interpretation, McDougall and McIntosh (1996) had already produced an application of Gent and McWilliams (1990) for slightly different averaging in a z -coordinate ocean model. McDougall and McIntosh (2001) also demonstrated an intuitive link between the quasi-Stokes velocity of the TRM circulation (which is based in Cartesian coordinates) and the eddy-induced extra advection caused by thickness-weighted averaging, which is the

natural way of averaging in density coordinates. TRM is very important because it retains the adiabatic nature of the Gent and McWilliams (1990) parameterization and in the meantime allows the interpretation of results from z-coordinate models.

In the same way as the temporal correlations are considered in the quasi-Stokes TRM streamfunction, unresolved spatial correlations between temperature and horizontal velocity will contribute horizontal density fluxes that should also be included in ocean models. Therefore, McDougall (1998) suggested that the same physical integrating procedure could be done in space rather than in time, and in so doing, an ocean model could represent the effects of the spatial correlations between the velocity and tracer fields that have not been represented in models to date. McDougall (1998) thus considered the effect of spatial resolution limitations on the horizontal transport of seawater that is denser than the isopycnal whose average height is the height being considered. The term Horizontal Residual Mean (HRM) was coined to describe the total velocity that would include the extra advection of seawater of this density class due to unresolved spatial correlations. The eddy-induced advection of the HRM circulation can be regarded as the adiabatic way of including the horizontal density fluxes due to unresolved spatial correlations. The importance of this type of unresolved spatial correlation to oceanic meridional heat transport has been discussed by Rintoul and Wunsch (1991).

Although McDougall (1998) hypothesized the concept of HRM, there has been no work done regarding this idea for nearly two decades. In this thesis, I propose a method of approximating the transport of scalar quantities due to spatial correlations that are unresolved by ocean models. The method introduces an extra non-divergent advection which is calculated from resolved model fields via a Taylor-series approximation. Moreover, I demonstrate that the method of calculating the streamfunction from coarsely-resolved model fields gives a good approximation to the corresponding transport of seawater that would be available in a finer resolution ocean model. This HRM streamfunction does not involve a parameterization. Rather, it is an estimate of the transport induced by the spatial correlation between the scalar and velocity fields, and the calculation is directly made using the variables available in the ocean model. Finally, we diagnose the contribution of the extra non-divergent advection to

basin-scale meridional heat and mass transports contained in a model snapshot.

The method I propose can be incorporated into ocean models to include the unresolved spatial correlations. In a forward model, the slope of the neutral tangent plane is estimated by taking the ratio of horizontal and vertical density gradients. We have calculated the HRM transports in both meridional and zonal directions using the density gradient ratio as the slope of neutral tangent plane. The comparison between the HRM transports calculated in two ways has shown that the method is not sensitive and therefore will be feasible to be incorporated into forward ocean models. Although we put a limit of 10^{-2} to the slope of neutral tangent plane, experimentally the limit has no significant importance since only a small amount of slopes exceeded the limit. The actual implementation certainly needs a full understanding of features of the model to which the HRM method applies and awaits future efforts.

The HRM theory is a spatial analogue of TRM. These two theories are based on a common ground and were in completed form when being used together. There have been other residual mean theories proposed, for example Eden (2010) and Eden (2012) who interpreted the scalar variables as the Eulerian-mean versions, while adopting a version of the residual mean for the velocity field. On a more theoretical level, a fully Lagrangian averaging framework could be envisaged, but to date there has not been a practical implementation of this approach. Rather, the fully Lagrangian framework is a theoretical construct to which all other forms of averaging can be compared.

The eddy closure of the GM scheme (the TRM advection) have been extensively studied in the literature from Gent et al. (1995) to the present day, with perhaps 200 papers addressing this issue. The thesis touches on the main practical requirements of a workable TRM quasi-Stokes streamfunction, namely that it be tapered appropriately near the oceans boundaries. Since the HRM closure scheme of this thesis requires no parameterization, I have not further expounded on the parameterizations that are specific to the TRM/GM scheme, since this is not relevant to our HRM approach.

The thesis is organised as follows. Double diffusive interleaving structures are examined as they progress from linear instability towards finite amplitude in chapter 2. We start from the model equations and go through regime by regime, using flux laws to characterize the heat and salt fluxes across the intrusion interfaces and determine

the conditions needed to reach steady state. In the end, we analyse the properties in steady state and discuss possible implications one can draw from the results. In chapter 3, we evaluate the HRM streamfunction as a method that estimates the transport induced by unresolved spatial correlations. We also demonstrate the diagnosis of a practical method that approximates the transport of seawater that is denser than the isopycnal whose spatially and temporally averaged height is the height one is considering. The possibility of implementing the HRM streamfunction into ocean models, for example Modular Ocean Model, has been proposed by showing that the calculation of the HRM transport can use available data in the MOM without additional complexity. A summary of the findings and discussions will be placed in chapter 4.

Chapter 2

Double Diffusive Interleaving: Properties of the Steady-State Solution

2.1 Introduction

Toole and Georgi (1981) built a theoretical model of double-diffusive interleaving using a linear stability analysis and showed that these quasi-horizontal intrusions are driven by the vertical buoyancy fluxes of double-diffusive convection. McDougall (1985a) showed that the same growing intrusions occurred whether or not the environment was rotating, and McDougall (1985b) made a start at studying these interleaving motions at finite amplitude. He hypothesized that it may be possible that the growth of the intrusions might be arrested at finite amplitude when every second interface changes its nature from the finger type to the diffusive type. The reason for this possible steady state is that the ratio of the fluxes of heat and salt across the two types of double-diffusive interfaces is quite different. In a steady state there needs to be a three-way balance between three processes (1) advection, (2) finger flux divergences, and (3) diffusive flux divergences, and this three-way balance needs to occur in both heat and salt.

While McDougall (1985b) showed that it was feasible that steady-state balances could be achieved for both heat and salt, it remained to be shown if such steady-state balances could be achieved with the fluxes across the double-diffusive interfaces taken

from the laboratory flux laws; these fluxes having been measured in one-dimensional laboratory experiments.

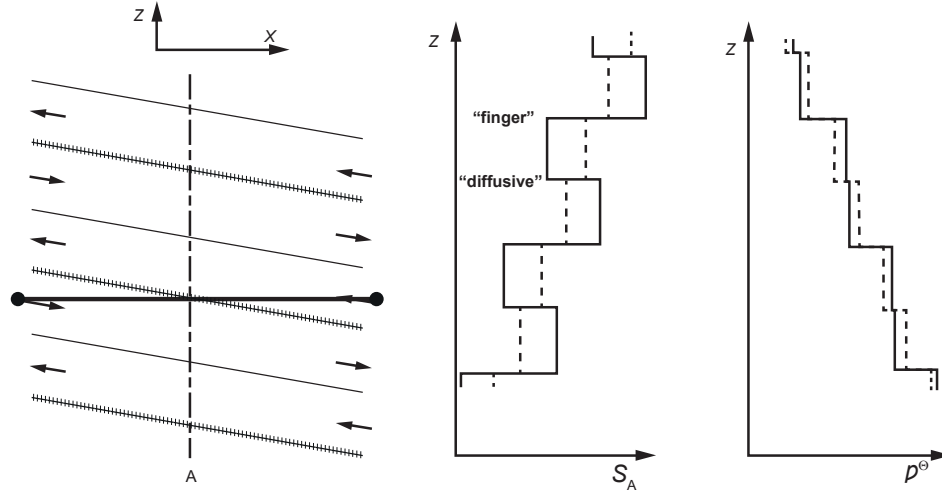


Figure 2.1: The sketch at the left is a vertical cross section through the frontal region showing the direction of cross-frontal motion of the intrusions and their slopes. The interfaces with vertical short lines represent the dominant finger interfaces. On the right-hand side, the two graphs show the Absolute Salinity and the density profiles at position A. The dashed lines indicate the initial state without perturbations, and the full lines show the profiles at a later stage.

In this chapter we form a finite-amplitude model of double-diffusive interleaving by integrating the temperature and salinity equations of each intrusion forward in time using the Runge-Kutta integration technique. Each layer is taken to be well-mixed in the vertical, separated by relatively sharp interfacial regions where the double-diffusive fluxes originate. The vertical length scale of the intrusions, and their slope with respect to the isopycnals are taken from the linear stability analysis. Following McDougall (1985b), there are three regimes as the intrusions evolve: firstly each interface is of the finger type (see Fig. 2.1). In the linear stability analysis, each alternative finger interface grows at the expense of its neighbour. We start our model with a small (but finite) disturbance and the model allows the interleaving motions to grow to finite amplitude thereafter using realistic flux laws while still in this “finger-finger” regime. This stage

is followed by a stage where each alternate interface ceases to be a finger interface and instead becomes stably stratified in both temperature and salinity. A third stage follows in which each alternative interface becomes of the diffusive type in which cool fresh water overlies warmer saltier fluid (see Fig. 2.2 and 2.3).

The laboratory fluxes laws obtained by McDougall and Taylor (1984) and Huppert (1971) did not directly lead to steady interleaving solutions. In order to achieve a steady state, an exaggeration factor is introduced to adjust the fluxes across the diffusive interface given by laboratory. The steady state can only be achieved in the presence of this factor and we tested a range of values for this factor. The choice of exaggeration factor has been elaborated in section 2.6.

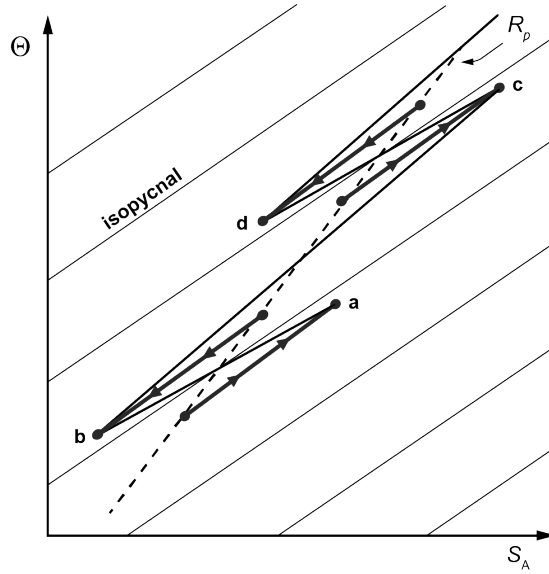


Figure 2.2: Conservative Temperature - Absolute Salinity diagram showing the evolution of the properties of the double-diffusive intrusions with time. The initial properties lie on the dashed line with slope $R_\rho \equiv \alpha \bar{\Theta}_z / \beta \bar{S}_{A_z}$. The arrowed lines connect the initial and final points of several layers.

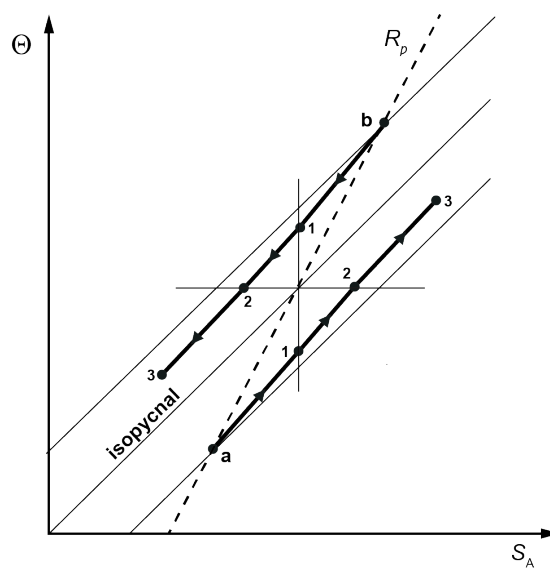


Figure 2.3: Absolute Salinity - Conservative Temperature diagram showing the evolution of the subservient finger interface between layers a and b. From a to 1, it is a finger interface and then from 1 to 2 is a non-double-diffusive interface. At last, from 2 to 3 is a diffusive interface. In the steady state, a diffusive interface exists between points 3 on this diagram.

2.2 The model equations

For reference purposes there is a list of symbols at the beginning of this thesis. We write down the basic conservation equations of intrusion motion following Toole and Georgi (1981) and McDougall (1985a). We assume an initial state of rest with horizontal isopycnals. We take the salinity and temperature variables to be those of the International Thermodynamic Equation of Seawater 2010 (TEOS-10), namely Absolute Salinity S_A and Conservative Temperature Θ [IOC et al. (2010), McDougall (2003), Graham and McDougall (2013)]. These variables vary along the initially horizontal isopycnal surfaces with S_A and Θ increasing in the positive x direction so that $\bar{S}_{Ay} = 0$ and

$$\beta \bar{S}_{Ax} = \alpha \bar{\Theta}_x. \quad (2.1)$$

The overbars indicate the state before interleaving sets in, and α and β are defined from the equation of state $\rho = \rho(S_A, \Theta, p)$ by

$$\alpha = -\frac{1}{\rho} \frac{\partial \rho}{\partial \Theta} \Big|_{S_A, p} \quad \text{and} \quad \beta = \frac{1}{\rho} \frac{\partial \rho}{\partial S_A} \Big|_{\Theta, p}. \quad (2.2)$$

The conservation equations for momentum, continuity, Absolute Salinity and Conservative Temperature are [see equations (3) - (8) of (McDougall, 1985a)]

$$u'_t - f v' = -\rho^{-1} p'_x - \nabla \cdot F^x, \quad (2.3)$$

$$v'_t + f u' = -\rho^{-1} p'_y - \nabla \cdot F^y, \quad (2.4)$$

$$w'_t = -\rho^{-1} p'_z - g(\beta S'_A - \alpha \Theta') - \nabla \cdot F^z, \quad (2.5)$$

$$u'_x + v'_y + w'_z = 0, \quad (2.6)$$

$$\beta S'_{At} + u' \beta \bar{S}_{Ax} + w' \beta \bar{S}_{Az} = -\beta \nabla \cdot F^{S_A}, \quad \text{and} \quad (2.7)$$

$$\alpha \Theta'_t + u' \alpha \bar{\Theta}_x + w' \alpha \bar{\Theta}_z = -\alpha \nabla \cdot F^\Theta, \quad (2.8)$$

where F^x , F^y and F^z are the fluxes of x , y and z momentum, and F^{S_A} and F^Θ are the fluxes of Absolute Salinity and Conservative Temperature caused by double-diffusive convection.

In some studies [e.g. Toole and Georgi (1981) and Walsh and Ruddick (1998)] these double-diffusive fluxes are assumed to be directed down the respective salinity and temperature gradients with eddy diffusion coefficients that depend on whether the

vertical gradients are conducive to the salt-fingering type of double-diffusion, or to the diffusive type. In these studies, the vertical profiles are smooth, continuous functions of the vertical coordinate; often the vertical structure function is harmonic and the nonlinear advection terms turn out to be zero. We follow McDougall (1985a) and McDougall (1985b) and adopt a different strategy which we believe is more consistent with applications to the ocean and with comparisons to the laboratory-determined flux laws. We take the values of Absolute Salinity and Conservative Temperature and their respective perturbations to be constant in the vertical within each intrusion layer, with sharp property differences across the sheared interfaces that separate the quasi-horizontally moving intrusions. In this way we are able to apply the laboratory flux laws that describe the fluxes of heat and salt across sharp interfaces (as opposed to down smooth gradients).

Since we assume Absolute Salinity to be piecewise constant in the vertical direction, the vertical profile of perturbations in this study is a square wave. The vertical flux of salt due to finger double-diffusive convection F^{SA} is negative, which indicates a downward flux. During the linearly unstable growing solution, each interface is of the finger type, with each alternate interface being either a dominant or subservient finger interface.

In McDougall's model, \hat{B} is taken as the proportionality constant between the salt flux across a finger interface and the salinity difference across the interface during the linearly unstable growth phase; that is, $\beta F_f^{SA} = \hat{B} \beta \Delta S_A^f$. During this initial exponential growth phase the fluxes are a linearization of the 4/3 flux laws. Thereafter we adopt the finite amplitude result that the fluxes are proportional to the 4/3 power of the property contrasts instead of the 3/3 power which has been used in previous studies. We consider the mean vertical stratification to be in the finger sense, that is, in this work we take $\beta \bar{S}_{Az} > 0$ (with height z defined positive upwards) and $R_\rho = \alpha \bar{\Theta}_{Az} / \beta \bar{S}_{Az} > 1$. Initially each interface is in the finger sense and as the perturbations S'_A grow, the salinity contrast across one interface increases by $2S'_A$ and the salinity contrast across the other interface decreases by $2S'_A$. The difference between the fluxes of salt across adjacent interfaces is then $\pm 4\hat{B}S'_A$.

The vertical wavenumber of the intrusions is defined as \hat{m} and the vertical wave-

length is $h = 2\pi/\hat{m}$, with the height of an individual intrusion being $\frac{1}{2}h$. The right-hand side of the salt conservation equation 2.7 during this linearly unstable growth phase is then

$$-\beta \nabla \cdot F^{SA} = -\frac{4\hat{B}\beta S'_A}{\frac{1}{2}h} = -\frac{4}{\pi}\hat{B}\hat{m}\beta S'_A = -B\hat{m}\beta S'_A \quad (2.9)$$

where we have defined $B = 4\hat{B}/\pi$ for convenience. Similarly, the divergences of the fluxes of momentum in equations 2.3, 2.4 and 2.5 are given by

$$-\nabla \cdot (F^x, F^y, F^z) = -\frac{4\hat{D}}{\frac{1}{2}h}(u', v', w') = -D\hat{m}(u', v', w') \quad (2.10)$$

where \hat{D} is the flux coefficient of momentum, and we simply use $D = 4\hat{D}/\pi$ for convenience.

This study starts with the exponentially growing linearly unstable solutions of McDougall (1985a), and the essential features of that study are summarized in Appendix A. We follow McDougall (1985b) in assuming that the isopycnals do not slope so that the horizontal gradients of Absolute Salinity and Conservative Temperature are balanced in their effects on density, that is, $\beta\bar{S}_{Ax} = \alpha\bar{\Theta}_x$, where x is the horizontal cross-frontal coordinate. Consider one layer with thickness of $h/2$, where $h = 2\pi/\hat{m}$ is the vertical wavelength of the disturbance. In the present model, the flux divergences are interpreted in terms of lower and upper fluxes bounding an individual intrusion. Integrating the conservation equation 2.7 over the thickness of an individual layer gives

$$\frac{1}{2}h\beta S'_{At} + \frac{1}{2}hu'\beta\bar{S}_{Ax} + \frac{1}{2}hw'\beta\bar{S}_{Az} = \beta F_{lower}^{SA} - \beta F_{upper}^{SA}. \quad (2.11)$$

Several properties of the growing interleaving motion are set during the exponentially growing phase, namely, the slope of the intrusion to the horizontal s , the dimensionless vertical wavenumber m , and the ratio of the perturbation horizontal and vertical velocities. The slope of the interleaving motions with respect to the isopycnals s is the solution of the following cubic equation [from McDougall (1985a)]

$$\tilde{s}^3 4(1 + \epsilon_z)\epsilon_z(\sigma - 1 - \epsilon_z) + \tilde{s}^2 4(1 + \epsilon_z)(1 + 2\epsilon_z - \sigma) + \tilde{s}(\sigma - 4 - 5\epsilon_z) + 1 = 0, \quad (2.12)$$

while the vertical wavenumber \tilde{m} is given by

$$\tilde{m} = \tilde{s}\sqrt{\sigma}\left\{\sigma - \left[\frac{1}{2\tilde{s}} - (1 + \epsilon_z)\right]^2\right\}^{-\frac{1}{2}} \quad (2.13)$$

and the vertical and horizontal velocity perturbations are related by

$$w' = -su'. \quad (2.14)$$

Here we have introduced the shorthand notations

$$\tilde{s} = \frac{s}{\epsilon_x}, \quad \text{and} \quad \tilde{m} = \frac{\sqrt{\sigma}m}{\epsilon_x},$$

and the dimensionless vertical wavenumber m , slope of the intrusions to the horizontal s , and the Prandtl number σ , are given by

$$m = \frac{B\hat{m}}{N}, \quad s = \frac{\hat{k}}{\hat{m}}, \quad \sigma = \frac{D}{B},$$

where ϵ_x and ϵ_z are defined by

$$\epsilon_x = \frac{(1 - \gamma_f)g\beta\bar{S}_{Ax}}{N^2} \quad \text{and} \quad \epsilon_z = \frac{(1 - \gamma_f)g\beta\bar{S}_{Az}}{N^2} = \frac{(1 - \gamma_f)}{(R_\rho - 1)}.$$

These relationships have been written in terms of the following properties of the background mean oceanic stratification, namely, the stability ratio R_ρ and the square of the buoyancy frequency N :

$$R_\rho = \frac{\alpha\bar{\Theta}_z}{\beta\bar{S}_{Az}}, \quad N^2 = g(\alpha\bar{\Theta}_z - \beta\bar{S}_{Az}) = g\beta\bar{S}_{Az}(R_\rho - 1),$$

and γ_f is the buoyancy-flux ratio of the fluxes across the salt-finger interfaces. Equations 2.12, 2.13 and 2.14 above are the finite-Prandtl number solutions, and we will adopt this finite-Prandtl number case in this work, as Ruddick et al. (1989) and Smyth and Kimura (2007) considered that the appropriate value of Prandtl number is to be $O(1)$ or less.

Equation 2.11 is now simplified by using the known ratio of the vertical and horizontal velocity perturbations (from equations 2.12, 2.13 and 2.14 above), and eliminating w' gives

$$\frac{1}{2}h\beta S'_{At} + \frac{1}{2}hu'\beta\bar{S}_{Ax}(1 - \tilde{s}\epsilon_z) = \beta F_{lower}^{S_A} - \beta F_{upper}^{S_A}. \quad (2.15)$$

Similarly, equation 2.8 becomes

$$\frac{1}{2}h\alpha\Theta'_t + \frac{1}{2}hu'\beta\bar{S}_{Ax}(1 - \tilde{s}R_\rho\epsilon_z) = \alpha F_{lower}^{\Theta} - \alpha F_{upper}^{\Theta}. \quad (2.16)$$

In what follows it proves convenient to use the following nondimensional salinity and temperature variables X and Y , defined by

$$X = \frac{2\beta S'_A}{\frac{1}{2}h\beta\bar{S}_{Az}}, \quad \text{and} \quad Y = \frac{2\alpha\Theta'}{\frac{1}{2}h\beta\bar{S}_{Az}}. \quad (2.17)$$

We now discuss the relationship between the perturbation horizontal velocity u' and the density perturbation. During the exponentially growing stage the momentum equation is deduced from equations 2.11, 2.13 and (38) of McDougall (1985b), as follows (under the assumption of the slope of the interleaving motions, s , is small)

$$-\hat{\lambda}u' = sg(\alpha\Theta' - \beta S'_A) + D^0\hat{m}u' \quad (2.18)$$

and initially the perturbation horizontal velocity u' is

$$u'_0 = -\frac{g(\alpha\Theta' - \beta S'_A)}{\sqrt{\sigma}N} \frac{\tilde{s}}{\tilde{m}} \left[1 + \frac{1}{\sqrt{\sigma}} \left(1 - \frac{\tilde{s}^2}{\tilde{m}^2} \right)^{\frac{1}{2}} \right]^{-1}, \quad (2.19)$$

which is derived from the linearly unstable momentum equation [see equation (39) of McDougall (1985a)]. If a steady state is reached, the rate of change of the horizontal velocity perturbation (corresponding to the term on the left-hand side of equation 2.18) needs to vanish, or otherwise the intrusion velocity will continue to accelerate. Under this assumption, the steady-state versions of the two terms on the right-hand side of equation 2.18 will balance each other out, implying that the horizontal velocity perturbation and the density perturbation in the steady state are related by

$$u'_{ss} = -\frac{D^0}{D^{ss}} \frac{g(\alpha\Theta' - \beta S'_A)}{\sqrt{\sigma}N} \frac{\tilde{s}}{\tilde{m}}. \quad (2.20)$$

Beginning at equation 2.18, we have allowed the possibility that the value of the turbulent viscosity may increase from D^0 to D^{ss} as steady state is approached. During the process of evolution, we assume that the ratio of the perturbation horizontal velocity to the density perturbation will change linearly with Y and is represented by

$$u' = -\frac{g(\alpha\Theta' - \beta S'_A)}{\sqrt{\sigma}N} \left[G^0 + (G^{ss} - G^0) \frac{(Y - Y_0)}{(R_\rho - Y_0)} \right], \quad (2.21)$$

where

$$G^0 = \frac{\tilde{s}}{\tilde{m}} \left[1 + \frac{1}{\sqrt{\sigma}} \left(1 - \frac{\tilde{s}^2}{\tilde{m}^2} \right)^{\frac{1}{2}} \right]^{-1} \quad \text{and} \quad G^{ss} = \frac{D^0}{D^{ss}} \frac{\tilde{s}}{\tilde{m}}. \quad (2.22)$$

This rather arbitrary linear function of Y allows the velocity perturbation to be that of the exponentially growing solution at the initial condition (X_0, Y_0) , while ensuring that the ratio of the velocity and density perturbations becomes constant at $Y = R_\rho$ well before any possible steady state is reached. That is, the linear function of Y of

equation 2.21 provides a credible way of transitioning between equation 2.19 and 2.20. For $Y > R_\rho$, we use equation 2.20.

Substituting equation 2.21 into equation 2.15 and dividing both sides \hat{B} leads to

$$\frac{\pi}{\hat{m}\hat{B}}\beta S'_{At} - \frac{\pi}{\hat{m}\hat{B}}\beta \bar{S}_{Ax}(1 - \tilde{s}\epsilon_z)\frac{g}{\sqrt{\sigma}N}(\alpha\Theta' - \beta S'_A)G(Y) = \frac{\beta F_{lower}^{SA} - \beta F_{upper}^{SA}}{\hat{B}}, \quad (2.23)$$

where (from equation 2.21)

$$G(y) \equiv G(\tilde{s}, R_\rho, Y) = G^0 + (G^{ss} - G^0)\frac{Y - Y_0}{R_\rho - Y_0}.$$

Dividing both sides of equation 2.23 by $\frac{1}{4}h\beta\bar{S}_{Az}$ and using nondimensional time $t = \hat{t}\pi^{-1}\hat{m}\hat{B}$, we find

$$X_t = \frac{4}{(1 - \gamma_f)}\frac{1}{\tilde{m}}(1 - \tilde{s}\epsilon_z)(Y - X)G(Y) = \frac{2}{\frac{1}{2}h\beta\bar{S}_{Az}}\frac{\beta F_{lower}^{SA} - \beta F_{upper}^{SA}}{\hat{B}}. \quad (2.24)$$

Similarly, the equation 2.16 becomes

$$Y_t - \frac{4}{(1 - \gamma_f)}\frac{1}{\tilde{m}}(1 - \tilde{s}\epsilon_z R_\rho)(Y - X)G(Y) = \frac{2}{\frac{1}{2}h\beta\bar{S}_{Az}}\frac{\alpha F_{lower}^\Theta - \alpha F_{upper}^\Theta}{\hat{B}} \quad (2.25)$$

To choose the initial starting point for the model, we take a small value of X , X_0 , and use the relationship between X_0 and Y_0 which applies during the exponentially growing linearly unstable solution (see equation B.1 in Appendix B).

For the results we present in this chapter, we have taken the initial value of X_0 to be 0.1, but we have demonstrated that the results are insensitive to this starting value by also doing some cases with $X_0 = 0.01$ and $X_0 = 0.2$. In summary, the cases with $X_0 = 0.01$ yielded values of X and Y at the steady-state that were typically larger than those obtained with $X_0 = 0.1$ by only 10^{-4} , while the cases with $X_0 = 0.2$ yielded values of X and Y at the steady-state that were typically smaller than those obtained with $X_0 = 0.1$ by only 10^{-3} . This demonstrates that the solutions are quite insensitive to our choice of $X_0 = 0.1$ as the initial condition where the growth of the interleaving changes from being the linearly unstable solution to one based on the finite-amplitude laboratory flux laws.

The sensitivity to the initial condition was tested in another way by deliberately disobeying the ratio of the initial values of X and Y as given by equation B.2 in Appendix B. We multiplied the right-hand side of equation B.2 by the factor 0.8 so that the initial value of the temperature perturbation was only 80% that of the linearly

growing solution. This changed the steady-state values of X and Y by only 10^{-2} , or less than 0.5% of these steady-state values. On the basis of these two types of tests, we conclude that the model is quite insensitive to details of the initial conditions.

In this work, we adopt the finite-amplitude laboratory-based expressions for the double-diffusive fluxes of heat from Huppert (1971) and of salt, from McDougall and Taylor (1984), at all stages of the numerical integration after the initial condition at $X_0 = 0.1$. The laboratory flux laws for both finger interfaces and diffusive interfaces are described in Appendix C. Note that in this entire study we take the flux ratio of salt fingers to be $\gamma_f = 0.5$.

Last, we present the salinity and temperature contrasts across finger and diffusive interfaces in terms of nondimensional variables X and Y . For the dominant finger interfaces, the property contrasts across them [see Fig. 2.1, adopted from McDougall (1985b)] are

$$\begin{aligned}\beta\Delta S_A^f &= \frac{h}{2}\beta\bar{S}_{Az} + 2\beta S'_A = \frac{h}{2}\beta\bar{S}_{Az}(1 + X) \quad \text{and} \\ \alpha\Delta\Theta^f &= \frac{h}{2}\alpha\bar{\Theta}_z + 2\alpha\Theta' = \frac{h}{2}\beta\bar{S}_z(R_\rho + Y),\end{aligned}\tag{2.26}$$

and the finger stability ratio is

$$R_\rho^f \equiv \frac{\alpha\Delta\Theta^f}{\beta\Delta S_A^f} = \frac{(R_\rho + Y)}{(1 + X)},\tag{2.27}$$

while for the other interfaces, the “subservient” finger interfaces across which the salinity contrast decreases with time,

$$\begin{aligned}\beta\Delta S_A^f &= \frac{h}{2}\beta\bar{S}_{Az} - 2\beta S'_A = \frac{h}{2}\beta\bar{S}_{Az}(1 - X) \quad \text{and} \\ \alpha\Delta\Theta^f &= \frac{h}{2}\alpha\bar{\Theta}_z - 2\alpha\Theta' = \frac{h}{2}\beta\bar{S}_z(R_\rho - Y),\end{aligned}\tag{2.28}$$

$$R_\rho^f \equiv \frac{\alpha\Delta\Theta^f}{\beta\Delta S_A^f} = \frac{(R_\rho - Y)}{(1 - X)}.\tag{2.29}$$

After sufficient time we anticipate that these subservient finger interfaces will become stably stratified with respect to both temperature and salinity, and after more time has elapsed, these interfaces will be stratified in the diffusive sense of double-diffusive convection. After this time, the property contrasts across them are

$$\begin{aligned}\beta\Delta S_A^{\text{diff}} &= 2\beta S'_A - \frac{h}{2}\beta\bar{S}_{Az} = \frac{h}{2}\beta\bar{S}_{Az}(X - 1) \quad \text{and} \\ \alpha\Delta\Theta^{\text{diff}} &= 2\alpha\Theta' - \frac{h}{2}\alpha\bar{\Theta}_z = \frac{h}{2}\beta\bar{S}_{Az}(Y - R_\rho),\end{aligned}\tag{2.30}$$

and the diffusive stability ratio is

$$R_\rho^{\text{diff}} \equiv \frac{\beta \Delta S_A^{\text{diff}}}{\alpha \Delta \Theta^{\text{diff}}} = \frac{(X-1)}{(Y-R_\rho)}. \quad (2.31)$$

2.3 The transition to finite amplitude in the finger-finger (FF) regime

The evolution of double-diffusive interleaving goes through three regimes: the finger-finger (FF) regime with finger interfaces at each interface, the finger-nondouble-diffusive (FN) regime with nondiffusive interfaces as each alternate interface, and the finger-diffusive (FD) regime with diffusive interfaces alternating with finger interfaces (see Fig. 2.3). As explained above, we transition from the linearly unstable growing solution to having the interfacial fluxes determined by the laboratory flux laws at a very early part of the FF stage when $X = X_0 = 0.1$. We ensure that the laboratory flux law expressions are joined in a continuous fashion to the exponentially growing linearly-unstable solutions that are used to initialize our model intrusions. In this study, the value of the finger flux ratio γ_f is fixed at 0.5 throughout the three regimes.

The integration remains in the FF regime until X reaches 1 (see equation 2.29). In this regime, both upper and lower interfaces are finger interfaces. More specifically, in the intrusion we are considering the lower finger interface is dominant and the upper finger interface is subservient. The evolution equations for the nondimensional variables X and Y in this finite amplitude FF regime are

$$X_t - \frac{4}{(1 - \gamma_f)} \frac{1}{\tilde{m}} (1 - \tilde{s}\epsilon_z)(Y - X)G(Y) = -\frac{4X_0}{A(X_0, Y_0)} A(X, Y), \quad (2.32)$$

and

$$Y_t - \frac{4}{(1 - \gamma_f)} \frac{1}{\tilde{m}} (1 - \tilde{s}\epsilon_z R_\rho)(Y - X)G(Y) = -\gamma_f \frac{4X_0}{A(X_0, Y_0)} A(X, Y), \quad (2.33)$$

where

$$A(X, Y) = \left\{ \frac{(1 + X)^{\frac{4}{3}}}{\left[\frac{(R_\rho + Y)}{(1 + X)} - 0.5 \right]} - \frac{(1 - X)^{\frac{4}{3}}}{\left[\frac{(R_\rho - Y)}{(1 - X)} - 0.5 \right]} \right\}. \quad (2.34)$$

These equations 2.32 - 2.34 are derived in Appendix D. The nondimensional equations 2.32 and 2.33 are used in regime FF, that is, from the initial value of $X = X_0 = 0.1$ until x reaches 1.

2.4 The integration in the finger-nondouble-diffusive (FN) regime

In the FN regime, the upper interface is not double-diffusive so that the fluxes of heat and salt across it are set to zero. In this FN regime, the lower interface remains a finger interface. This regime lasts while $X > 1$ and $Y < R_\rho$, and the evolution equations 2.24 and 2.25 become (see the first part of equation 2.34, and equations 2.32 and 2.33 for motivation)

$$X_t - \frac{4}{(1 - \gamma_f)} \frac{1}{\tilde{m}} (1 - \tilde{\epsilon}_z)(Y - X)G(Y) = -\frac{4X_0}{A(X_0, Y_0)} \frac{(1 + X)^{\frac{4}{3}}}{\left[\frac{(R_\rho + Y)}{(1 + X)} - 0.5\right]}, \quad (2.35)$$

$$Y_t - \frac{4}{(1 - \gamma_f)} \frac{1}{\tilde{m}} (1 - \tilde{\epsilon}_z R_\rho)(Y - X)G(Y) = -\gamma_f \frac{4X_0}{A(X_0, Y_0)} \frac{(1 + X)^{\frac{4}{3}}}{\left[\frac{(R_\rho + Y)}{(1 + X)} - 0.5\right]}. \quad (2.36)$$

2.5 The integration in the finger-diffusive (FD) regime

In the FD regime, the lower interface remains a finger interface and is parameterized exactly as in the FN regime. The fluxes across the upper interface are obtained by using laboratory diffusive flux laws (see Appendix C). Combining the contributions from the lower and upper interfaces, equation 2.24 now becomes

$$\begin{aligned} X_t - \frac{4}{(1 - \gamma_f)} \frac{1}{\tilde{m}} (1 - \tilde{s}\epsilon_z)(Y - X)G^{ss} \\ = -\frac{4X_0}{A(X_0, Y_0)} \frac{(1 + X)^{\frac{4}{3}}}{\left[\frac{(R_\rho + Y)}{(1 + X)} - 0.5\right]} - 0.7674\gamma_{\text{diff}} \frac{4X_0}{A(X_0, Y_0)} \frac{(Y - R_\rho)^{\frac{10}{3}}}{(X - 1)^2} \end{aligned} \quad (2.37)$$

where the flux ratio of the diffusive interface γ_{diff} is given by equations C.2 and C.3 in Appendix C, and the 0.7674 number is actually (from equations C.1 and C.4)

$$0.7674 \approx \frac{3.8 \times 0.085}{0.19} \left(\frac{\kappa_T}{\nu}\right)^{\frac{1}{3}}$$

which is the numerical factor that arises from substituting the laboratory diffusive flux of heat into equation 2.24, where ν is the viscosity. This same term gives rise to the following term of the right-hand side of equation 2.25:

$$-\frac{2}{\frac{h}{2}\beta\tilde{S}_{Az}} \frac{\alpha F_{\text{upper}}^\Theta}{\tilde{B}} = -0.7674 \frac{4X_0}{A(X_0, Y_0)} \frac{(Y - R_\rho)^{\frac{10}{3}}}{(X - 1)^2}, \quad (2.38)$$

and hence, in the FD regime, the evolution equation for Y (equation 2.25) is

$$\begin{aligned} Y_t - \frac{4}{(1 - \gamma_f)} \frac{1}{\tilde{m}} (1 - \tilde{s}\epsilon_z R_\rho)(Y - X)G(Y) \\ = -\gamma_f \frac{4X_0}{A(X_0, Y_0)} \frac{(1 + X)^{\frac{4}{3}}}{\left[\frac{(R_\rho + Y)}{(1 + X)} - 0.5\right]} - 0.7674 \frac{4X_0}{A(X_0, Y_0)} \frac{(Y - R_\rho)^{\frac{10}{3}}}{(X - 1)^2}. \end{aligned} \quad (2.39)$$

Last, we mention that if the density difference across the diffusive interface goes to zero, the integration cannot be continued since the layers above and below this interface would physically homogenize, and this is not part of our model. This occurs when $(Y - X) \geq (R_\rho - 1)$. If this condition is detected, the numerical integration is stopped.

2.6 The feasibility of the steady state

McDougall (1985b) suggested that a steady state would be possible once the fluxes across each alternate interface are in the diffusive sense, and it is the primary purpose of this chapter to find out the conditions under which such a steady state is achieved. In the steady state the double-diffusive fluxes across the finger and the diffusive interfaces must work together to balance the advective fluxes of both heat and salt so that the temporal derivatives Θ_t and S_t are both equal to zero. However, McDougall (1985b) only demonstrated the feasibility of such a steady state. In this chapter, we incorporate the laboratory flux laws and we investigate the conditions under which a steady state is actually achieved.

Fig. 2.1 [adapted from McDougall (1985b)] shows a sketch of a series of interleaving layers, in which the dominant finger interfaces are indicated by the short vertical lines. The two panels on the right show the Absolute Salinity and the density profiles at position A. The dashed lines represent the initial state in which the perturbations are zero and the full lines indicate a later state when the perturbations have grown to finite amplitude and the flow is in the FD regime. Above the dominant finger interfaces, the salt-finger salt flux reduces the salinity of the intrusion layer; however, the horizontal advection of salt dominates so that actually the salinity of this layer increases with time in the growing solution. In McDougall (1985a), it is shown that the perturbation Conservative Temperature is greater than the perturbation Absolute Salinity (both expressed in terms of density) during the initial growth phase. This implies that the density contrast across the dominant salt finger interface increases with time while that across the subservient finger interface decreases with time in the FF regime.

Fig. 2.2 [adapted from McDougall (1985b)] is a $S_A - \Theta$ diagram that shows the evolution of the layer properties. The layer properties initially lie on a line with slope $R_\rho = \alpha\bar{\Theta}_z/\beta\bar{S}_{Az}$. The Conservative Temperature and the Absolute Salinity change in the ratio $\alpha\Theta_0/\beta S_0$ of equation (40) of McDougall (1985a). Each successive layer has the opposite sign of change. Fig. 2.3 [adapted from McDougall (1985b)] shows the evolution of the subservient finger interface between layers with properties a and b. Starting as finger interfaces (from points a to 1), the subservient interfaces evolve to be not double-diffusive interfaces (between points 1 and 2) when the interface is

stable in both temperature and salinity contrasts. After the cold fresh water overlies the warm salty water, the interfaces become diffusive interfaces (between points 2 and 3). Eventually, the finger fluxes, the diffusive fluxes and the advective fluxes may reach a steady-state balance for both temperature and salinity. This stage is called steady state because the temporal rates of change of both temperature and salinity are zero.

As stated at the beginning of this section, the steady state occurs when the sum of the finger flux divergence term, the diffusive flux divergence term and the advective flux divergence term is zero, which implies that $\alpha\Theta_t = \beta S_{At} = 0$. In the FF regime, the diffusive flux does not appear, and during this stage, the growing solution is shown in Fig. 2.4(a) with both the temporal derivative terms and the advective terms being larger than the finger flux divergence term. This balance applies until points 1 in Fig. 2.3, and we should be mindful that in this study, even in this FF regime, the fluxes obey the finite-amplitude laboratory-determined flux laws. Fig. 2.4(b) corresponds to the period between points 1 and 2 of Fig. 2.3, where the rate of increase of the finger flux divergence is approximately halved because each alternate interface is stably stratified with respect to both Θ and S . During this FN regime it is clear that a steady state is not possible between just a finger flux divergence and the advective term; the temporal term and the advective term are observed to be larger than the finger flux divergence.

The feasibility of achieving a steady state is shown in Fig. 2.4(c). Diffusive fluxes emerge as the evolution reaches point 2, and these diffusive fluxes increase with time thereafter. Together with the finger fluxes, it is possible to reach a balance. We will now examine this process of reaching a steady state with our model.

We started at (X_0, Y_0) , with $X_0 = 0.1$ and with Y_0 determined from equation (40) of McDougall (1985a). The differential equations for X and Y are then integrated forward in time. We have done this for a range of values of the stability ratio of the water column R_ρ . To our surprise we found that a steady state was not possible with the laboratory flux laws. Rather, the subservient interface was always driven to be statically unstable in the FD regime. If this occurred in practice, the two layers bounding this interface would overturn and mix, resulting in a doubling of the vertical wavelength, as sometimes occurred in Ruddick (1984). In order to achieve a steady state, it became clear that the fluxes across the diffusive interface needed to be stronger relative to those across

the finger interface (or equivalently, the fluxes across the finger interfaces needed to be weaker with respect to those across the diffusive interface). For this reason we ran the model for a range of values of an exaggeration factor where we replaced the 0.7674 number that represents the strength of the diffusive interfaces in equations 2.37 - 2.39 with 0.7674 multiplied by an “exaggeration factor” which we varied from 5 to 40. One way to rationalize such an exaggeration factor is that the oceanic interfaces have much smaller property contrasts across them than do double-diffusive interfaces in the laboratory and perhaps this affects the strengths of the finger and diffusive interfaces in different ways.

The equations apply to any finite Prandtl number, and we show results for values of Prandtl number σ equal to 0.3, 1 and 10, but we mainly illustrate our results using $\sigma = 1$. To begin with, Fig. 2.5 shows contours of the steady state values of the nondimensional salinity and temperature perturbations, denoted (X^s, Y^s) plotted as a function of R_ρ and the exaggeration factor for the three selected values of Prandtl number σ . The similarity in those three pairs of figures is obvious. The values of X^s and Y^s depend more on the environmental stability ratio than on the exaggeration factor. In each of these panels the lower left corners are blank, which indicates that no steady states were found; in these regions, the diffusive flux divergence is unable to balance the advective and finger terms. With increasing R_ρ , when the basic stratification is less fingering favorable, the exaggeration factor required to achieve a steady state appears to be smaller. The results throughout this chapter for $\sigma = 10$ are almost identical to those for an infinite Prandtl number.

The evolution of X and Y towards the steady-state values X^s and Y^s is illustrated in Fig. 2.6(a). Once the steady state had been reached, the solution was perturbed a little in X and Y , and the integration was continued. The stable spiraling towards the steady-state values X^s and Y^s as illustrated in Fig. 2.6(b) was a characteristic feature of all the steady states.

The stability ratios of both the finger and diffusive interfaces at steady state can be calculated from equations 2.27 and 2.31, and the values for $\sigma = 1$ are shown in Fig. 2.7. The stability ratio of the diffusive interfaces are mostly near 2 or greater than 2, and this can be understood from equations C.2 and C.3 in Appendix C, which describe

the flux ratio across the diffusive interfaces. If the stability ratio across these diffusive interfaces becomes much less than 2 and approaches 1, then the flux ratio increases from 0.15 and approaches 1. In this limit it is clear from the angle of the diffusive flux vector on Fig. 2.4(c) that a steady-state balance is not possible as the flux of density across the finger interfaces is too strong. Note that when a steady state is not possible and the diffusive interface overturns, its stability ratio passes through 1.0 at that time. It appears that the only steady states that are possible have the stability ratio of the diffusive interfaces substantially greater than 1.0, with numbers greater than 1.6 being apparent from Fig. 2.7(a).

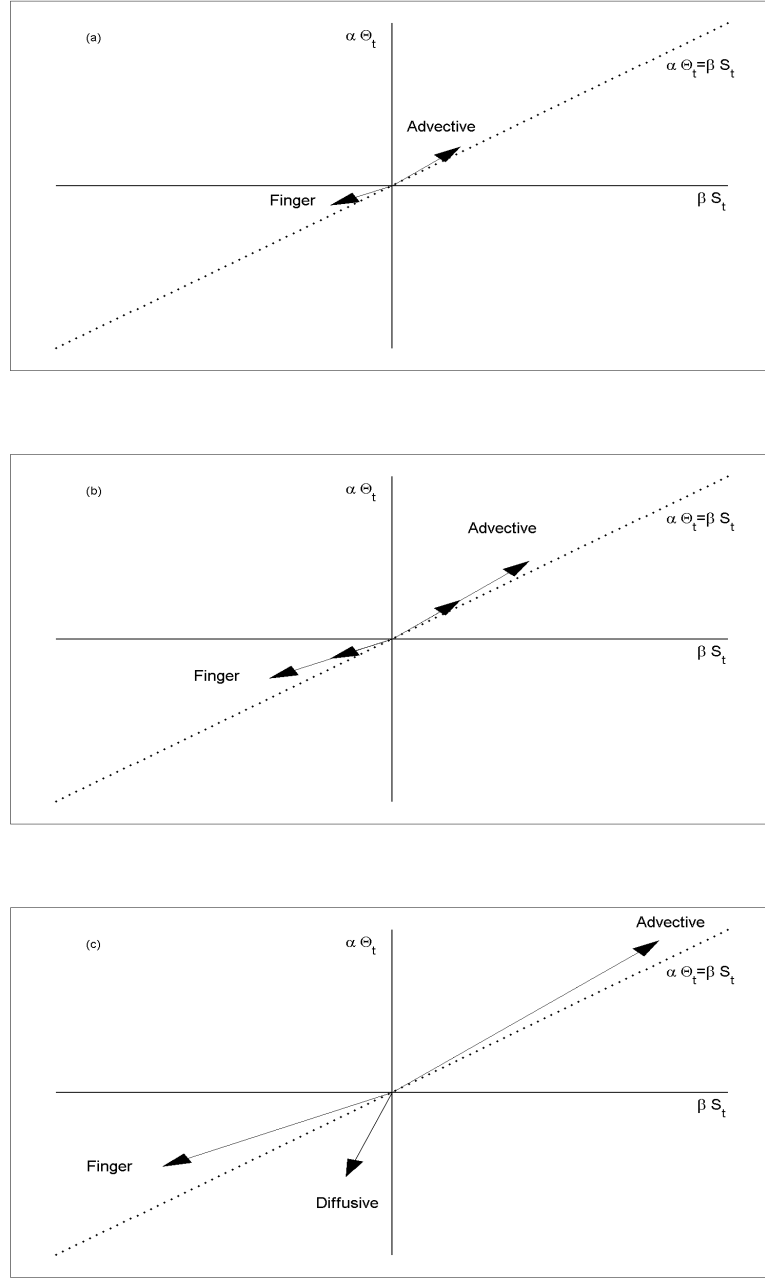


Figure 2.4: Contributions to the temporal derivative vector $(\alpha\Theta_t, \beta S_{At})$ from the double-diffusive fluxes and the advective terms. (a) The stage from points a to 1 in Fig. 2.3; this is the growing solution of the linear stability analysis of McDougall (1985a). (b) A sketch of the terms applying at the points 2 of Fig. 2.3. (c) Beyond points 2, the diffusive fluxes begin to grow and allow the possibility of a steady state solution in which $(\alpha\Theta_t, \beta S_{At})$ is $(0,0)$.

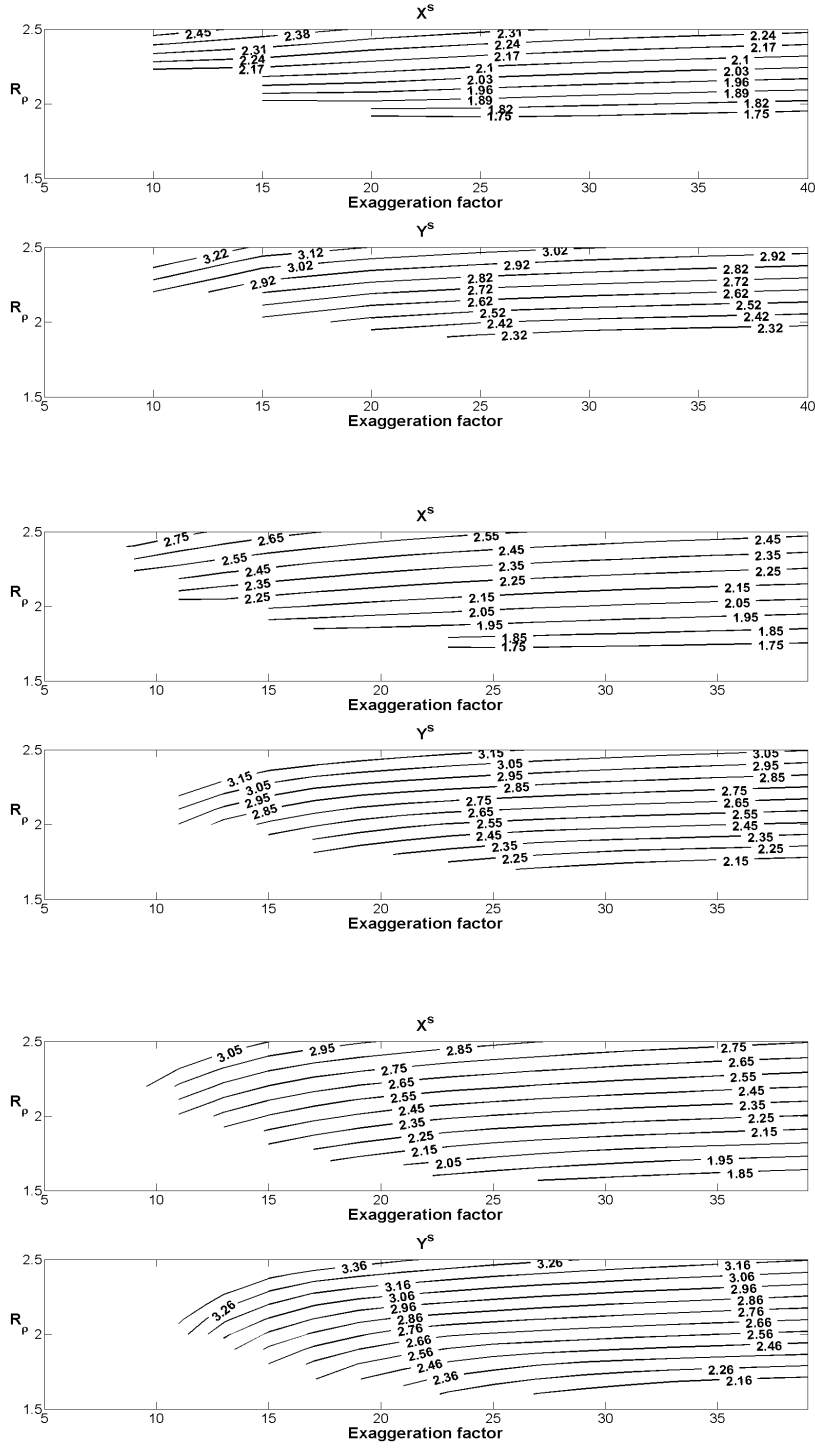


Figure 2.5: Contours of the nondimensional salinity and temperature variables X^s and Y^s of the steady state points with respect to the exaggeration factor and R_ρ . Three values for Prandtl number are selected: (top two) $\sigma = 0.3$, (middle two) $\sigma = 1$ and (bottom two) $\sigma = 10$.

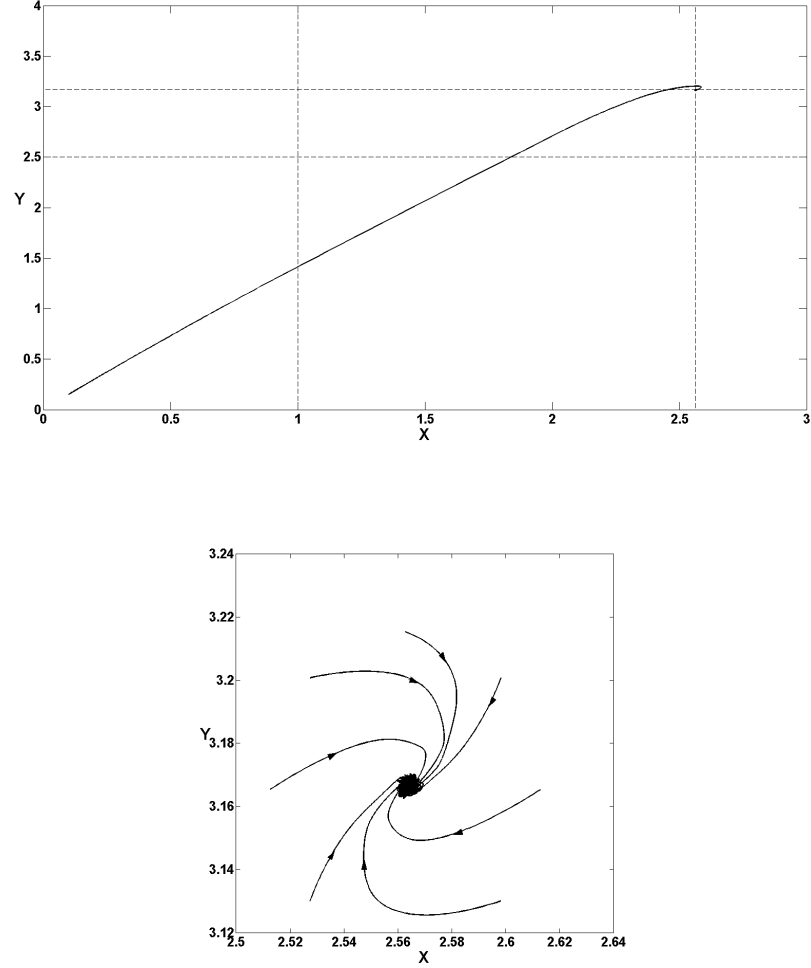


Figure 2.6: (top) A typical evolution of the nondimensional salinity and temperature variables X and Y towards the steady-state values at the end of the hook near the upper right-hand of the figure. (bottom) The loci of seven artificially perturbed points around the steady state point. These two panels are for the exaggeration factor $ef = 25$, $R_\rho = 2.5$ and $\sigma = 1$.

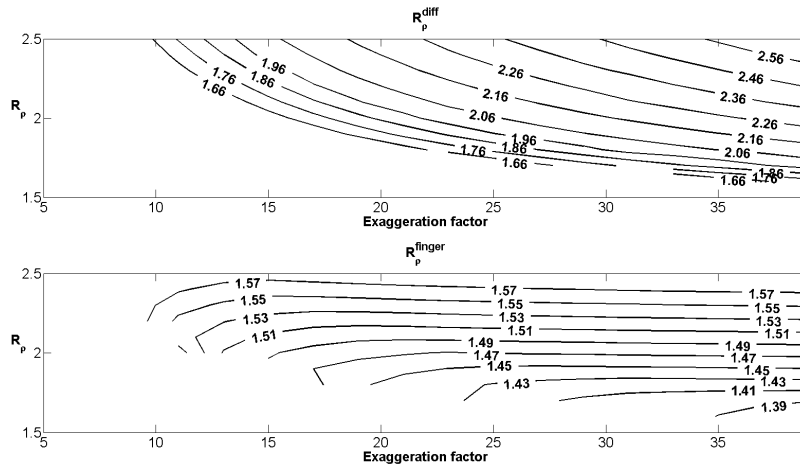


Figure 2.7: The stability ratios of the (top) diffusive and (bottom) finger interfaces at the steady state for $\sigma = 1$.

2.7 The relations among variables in the steady state

Notice that, in the steady state, the expressions of the vertical fluxes of salt across the finger and the diffusive interfaces correspond respectively to the first and second right-hand side term of equation 2.37. The absolute value of the ratio of the vertical flux of Absolute Salinity S_A across the diffusive interface to that across the finger interface in steady state is labeled a^s and is given by

$$\left| \frac{F_{\text{diff}}^{S_A}}{F_{\text{f}}^{S_A}} \right| = a^s = ef \times 0.7674 \gamma_{\text{diff}}^s \frac{(Y^s - R_\rho)^{\frac{10}{3}} \left(\frac{R_\rho - Y^s}{1 + X^s} - 0.5 \right)}{(X^s - 1)^2 (1 + X^s)^{\frac{4}{3}}}, \quad (2.40)$$

where ef is the exaggeration factor. Similarly, the expressions of the vertical fluxes of Conservative Temperature across the finger and the diffusive interfaces in the steady state, can be calculated from the two terms on the right-hand side of equation 2.39, which gives

$$\left| \frac{F_{\text{diff}}^\Theta}{F_{\text{f}}^\Theta} \right| = \frac{F_{\text{diff}}^\Theta}{F_{\text{diff}}^{S_A}} \frac{F_{\text{diff}}^{S_A}}{F_{\text{f}}^{S_A}} \frac{F_{\text{f}}^{S_A}}{F_{\text{f}}^\Theta} = \frac{a^s}{\gamma_{\text{diff}}^s \gamma_{\text{f}}}. \quad (2.41)$$

The values of a^s and $a^s/(\gamma_{\text{diff}}^s \gamma_{\text{f}})$ at each steady state point is shown in Fig. 2.8 as a function of the exaggeration factor ef and R_ρ . It is easy to notice that different values of Prandtl number do not have significant impact on the values of a^s and $a^s/(\gamma_{\text{diff}}^s \gamma_{\text{f}})$. For most of the steady-state solutions, the ratio of the diffusive to finger salt flux a^s is about 0.1, while the ratio of the diffusive to finger temperature flux $a^s/(\gamma_{\text{diff}}^s \gamma_{\text{f}})$ is about 1.0.

From equation (41) of McDougall (1985a), we have

$$\frac{\alpha \Theta_l}{\beta S_{A_l}} = 1 - \frac{\tilde{s}(1 - \gamma_{\text{f}})}{(1 - \epsilon_z \tilde{s})}, \quad (2.42)$$

where Θ_l and S_{A_l} are the gradients of Conservative Temperature and Absolute Salinity, respectively, in the direction of motion of an intrusion (or leaf). The ratio of these along-leaf gradients is set in the exponentially growing solution and remains the same in each of our three regimes. In the steady state, define \hat{B}^s by

$$\left| \beta F_{\text{f}}^{S_A} \right| = \hat{B}^s \frac{h}{2} \beta \bar{S}_{Az} (1 + X^s), \quad (2.43)$$

where $\frac{h}{2} \beta \bar{S}_{Az} (1 + X^s)$ is the salinity contrast across the finger interface in the steady state.

With the shorthand notations above, at steady state equations 2.37 and 2.39 are written as

$$-\frac{4}{(1-\gamma_f)}\left(\frac{1}{\tilde{m}}\right)(1-\tilde{s}\epsilon_z)(Y^s-X^s)G^{ss}=-2\frac{\hat{B}^s}{\hat{B}}(1+X^s)(1+a^s), \quad (2.44)$$

and

$$-\frac{4}{(1-\gamma_f)}\left(\frac{1}{\tilde{m}}\right)(1-\tilde{s}\epsilon_z R_\rho)(Y^s-X^s)G^{ss}=-2\frac{\hat{B}^s}{\hat{B}}(1+X^s)(\gamma_f+\frac{a^s}{\gamma_{\text{diff}}^s}). \quad (2.45)$$

Taking the ratio of 2.44 and 2.45 gives a relation between a^s and γ_{diff}^s , which is,

$$\frac{1}{\gamma_{\text{diff}}^s}=\frac{\alpha\Theta_l}{\beta S_{A_l}}+\frac{1}{a^s}\left(\frac{\alpha\Theta_l}{\beta S_{A_l}}-\gamma_f\right). \quad (2.46)$$

Fig. 2.9 shows the values of γ_{diff}^s , when $\sigma = 1$, at a range of steady state points as a function of the exaggeration factor and R_ρ . From equation C.3 in Appendix C, we see that γ_{diff}^s is constant when $R_\rho^{\text{diff}} \geq 2$, explaining why there are no contours in the upper-right region in Fig. 2.9.

Equation 2.44 can be rewritten using equation 2.42 to give an expression that relates a^s and the steady-state values of X and Y to the ratio of \hat{B}^s to \hat{B} , namely,

$$\frac{\hat{B}^s}{\hat{B}}=\frac{2(\frac{\tilde{s}}{\tilde{m}})^2(Y^s-X^s)(\frac{D_0}{D^{ss}})}{(1+X^s)(1+a^s)(1-\frac{\alpha\Theta_l}{\beta S_{A_l}})}, \quad (2.47)$$

which is shown in Fig. 2.10. From the above equation, X^s, Y^s, a^s and the environmental stability ratio R_ρ all contribute to this ratio, but from Fig. 2.10 we see that \hat{B}^s/\hat{B} is more sensitive to the environmental stability ratio R_ρ than to the exaggeration factor. The use of the finite-amplitude laboratory flux laws has led to an increase of \hat{B}^s over the value \hat{B} used in the linearly-growing solution of between 20% and 50%. Another relationship that applies in the steady state, this time between the steady-state values of X^s, Y^s and a^s is given by equation E.2 in Appendix E.

In the above development we have allowed for the possibility that the turbulent eddy viscosity may change as the interleaving motions grow to finite amplitude. We have investigated whether this is a significant issue by doing some cases with $D_0/D^{ss} = 1/1.4$ and the results of X^s and Y^s were no more than 10% different to those using $D_0/D^{ss} = 1$. This value of $D_0/D^{ss} = 1/1.4$ was chosen as being approximately equal

to the corresponding ratio of the change in the coefficient \hat{B} of the finger salt flux at finite amplitude (see Fig. 2.10). Since the results were rather insensitive to the value of D_0/D^{ss} , all the results in this chapter have used $D_0/D^{ss} = 1$.

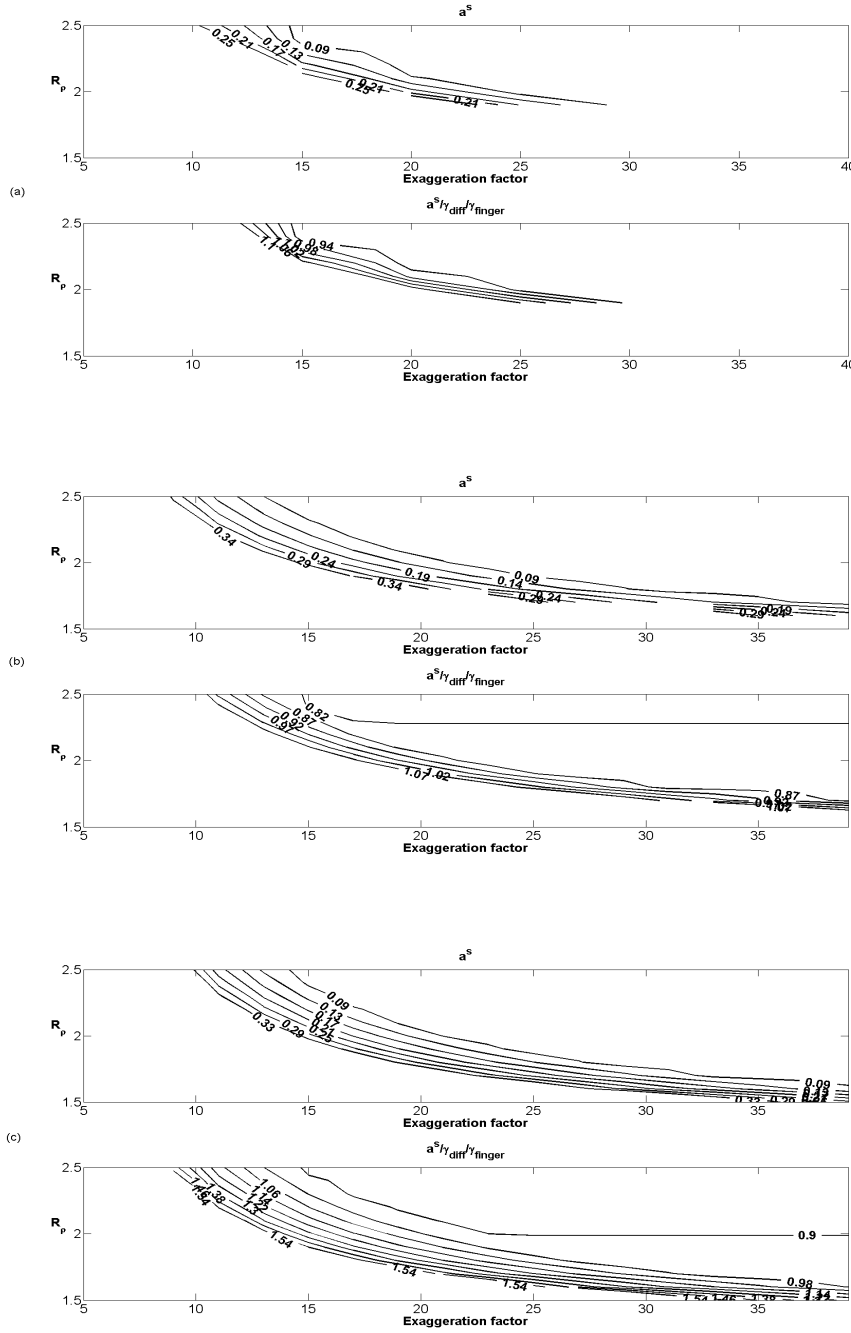
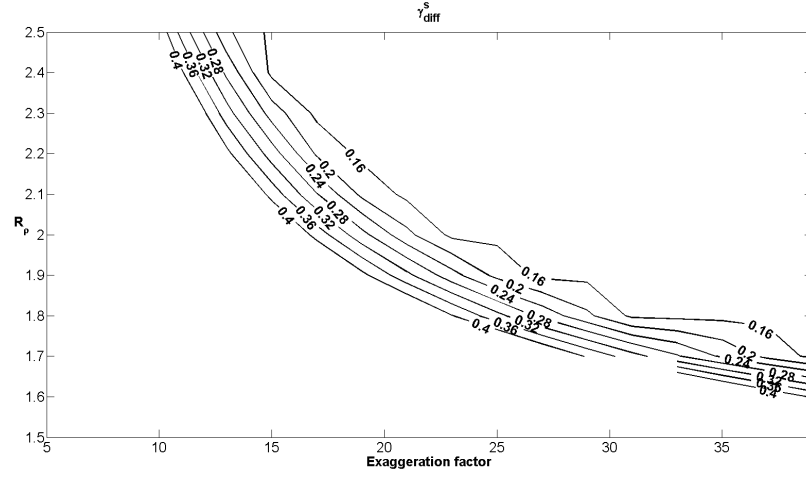
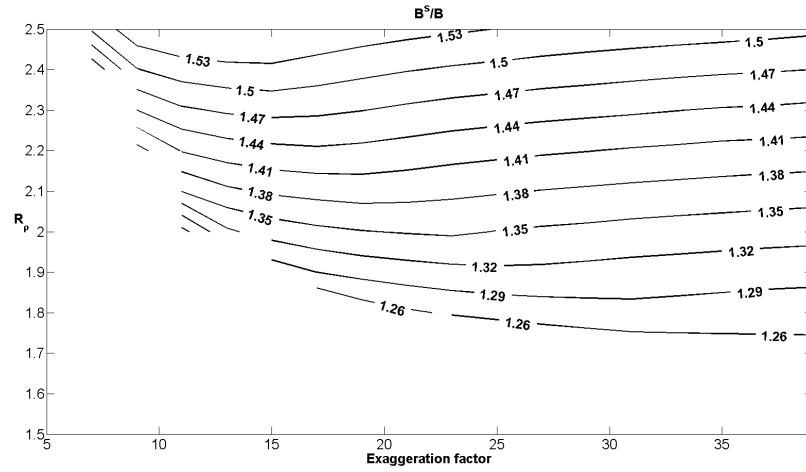


Figure 2.8: The upper panel of each pair shows the absolute value of the ratio of the vertical flux of salt across the diffusive interface to that across the finger interface in the steady state. The lower panel of each pair shows the absolute value of the ratio of the vertical flux of temperature across the diffusive interface to that across the finger interface in the steady state. Three values for Prandtl number are selected: (a) $\sigma = 0.3$, (b) $\sigma = 1$ and (c) $\sigma = 10$.

Figure 2.9: Values of γ_{diff}^s for the case of $\sigma = 1$.Figure 2.10: Values of the ratio \hat{B}^s/\hat{B} for the case of $\sigma = 1$.

2.8 The diapycnal fluxes at steady state

One of the most important features of interleaving motions is their ability to transport heat and salt across isopycnals. In the steady state there are two different types of contributions to the mean diapycnal flux of both salinity and temperature. First there is the spatial average of the double-diffusive fluxes of salt and temperature across the finger and diffusive interfaces, and this relevant average flux is simply the average of the finger and diffusive fluxes. Second, there is the area average on an isopycnal surface of the spatial correlation between the vertical velocity perturbation and the temperature (and salinity) perturbations. In turn, this advective contribution has two components: one being due to the correlated nature of the vertical velocity and the temperature and salinity perturbations at any location in space and the other due to the spatial correlation across the front of the vertical velocity and the cross-front salinity and temperature differences. This last aspect was missing from the work of McDougall (1985b) and we will find that this spatial correlation is significantly larger than the corresponding advective correlation at a fixed point in space (by a factor of about 4).

The need for the spatial correlation along the horizontal isopycnals can be understood from Fig. 2.1. The relevant salinity perturbations that should multiply the vertical velocity perturbations of the intrusions are the ones at the large dots of the left-hand panel of Fig. 2.1. The total relevant salinity perturbation is then the sum of the perturbation at a fixed point S'_A and a contribution because the two dots are separated in space in the across-front direction. The distance from the middle to the right-hand dot is $\frac{h}{4}s^{-1}$, that is, half the thickness of a single intrusion divided by the magnitude of the cross-front slope of the intrusions with respect to the density surfaces. The positive salinity perturbation at this right-hand dot is then S'_A plus $\frac{h}{4}s^{-1}\bar{S}_{Ax}$ (and \bar{S}_{Ax} is positive for the intrusions that move upwards from right to left and which have a positive S'_A). The average vertical advective salinity flux across isopycnals is then $w'(S'_A + \frac{h}{4}s^{-1}\bar{S}_{Ax})$. The total diapycnal flux of salt, TDFS, is then

$$\text{TDFS} = -\frac{1}{2}\hat{B}^s\frac{h}{2}\bar{S}_{Az}(1+x^s)(1-a^s) + w'(S'_A + \frac{h}{4}s^{-1}\bar{S}_{Ax}), \quad (2.48)$$

where the first term is the average of the salt fluxes across the finger and diffusive interfaces [with the finger flux of salt being negative (downward) and the diffusive flux

of salt being positive (upward)].

Combining equations 2.14 and 2.20 we find the following expression in the steady state for the vertical velocity in terms of the density perturbation:

$$w' = s \left(\frac{\tilde{s}}{\tilde{m}} \right) \left(\frac{D_0}{D^{ss}} \right) \frac{g(\alpha\Theta' - \beta S'_A)}{\sqrt{\sigma}N}, \quad (2.49)$$

and after a series of substitutions involving equations 2.13 and 2.47, we obtain

$$w' = \hat{B}^s (1 + X^s) (1 + a^s) \left(1 - \frac{\alpha\Theta_l}{\beta S_{A_l}} \right) (R_\rho - 1)^{-1}. \quad (2.50)$$

From the definition of ϵ_x , we have

$$S'_A + \frac{h}{4} s^{-1} \bar{S}_{Ax} = S'_A + \frac{\frac{h}{4} \bar{S}_{Az} (R_\rho - 1)}{(1 - \gamma_f) \tilde{s}}, \quad (2.51)$$

and substituting this back into equation 2.48, using equation 2.50, we find that TDFS becomes

$$\text{TDFS} = \hat{B}^s \frac{h}{4} \bar{S}_{Az} (1 + X^s) \left\{ - (1 - a^s) + (1 + a^s) \left(1 - \frac{\alpha\Theta_l}{\beta S_{A_l}} \right) \left[\frac{X^s}{(R_\rho - 1)} + \frac{1}{(1 - \gamma_f) \tilde{s}} \right] \right\}. \quad (2.52)$$

For the total diapycnal flux of Conservative Temperature (TDF Θ), a similar analysis applies, giving

$$\text{TDF}\Theta = -\frac{1}{2} \frac{\beta}{\alpha} \tilde{B}^s \frac{h}{2} \bar{S}_{Az} (1 + X^s) \left(\gamma_f - \frac{a^s}{\gamma_{\text{diff}}^s} \right) + w' (\Theta' + \frac{h}{4} s^{-1} \bar{\Theta}_x). \quad (2.53)$$

The total temperature perturbation at the right-hand big dot of Fig 2.1 is

$$\Theta' + \frac{h}{4} s^{-1} \bar{\Theta}_x = \Theta' + \frac{\frac{h}{4} \bar{S}_{Az} \frac{\beta}{\alpha} (R_\rho - 1)}{(1 - \gamma_f) \tilde{s}}, \quad (2.54)$$

and substituting this into equation 2.53 and using equation 2.50 we find

$$\text{TDF}\Theta = \frac{\beta}{\alpha} \hat{B}^s \frac{h}{4} \bar{S}_{Az} (1 + X^s) \left\{ - \left(\gamma_f - \frac{a^s}{\gamma_{\text{diff}}^s} \right) + (1 + a^s) \left(1 - \frac{\alpha\Theta_l}{\beta S_{A_l}} \right) \left[\frac{Y^s}{(R_\rho - 1)} + \frac{1}{(1 - \gamma_f) \tilde{s}} \right] \right\}. \quad (2.55)$$

Recall that the vertical flux of salt at steady state across the finger interface is

$$F_f^{S_{A^s}} = -\hat{B}^s \frac{h}{2} \bar{S}_{Az} (1 + X^s), \quad (2.56)$$

and it is convenient to express the total diapycnal fluxes in terms of $F_f^{S_{As}}$, so that equations 2.52 and 2.55 become

$$\frac{\text{TDFS}}{F_f^{S_{As}}} = \frac{1}{2}(1 - a^s) - \frac{1}{2}(1 + a^s) \left(1 - \frac{\alpha\Theta_l}{\beta S_{A_l}}\right) \left[\frac{X^s}{R_\rho - 1} + \frac{1}{(1 - \gamma_f)\tilde{s}}\right], \quad (2.57)$$

-0.29 = 0.47 - 0.15 - 0.61

$$\frac{\frac{\beta}{\alpha} F_f^{S_{As}}}{\text{TDF}\Theta} = \frac{1}{2}(\gamma_f - \frac{a^s}{\gamma_{\text{diff}}^s}) - \frac{1}{2}(1 + a^s) \left(1 - \frac{\alpha\Theta_l}{\beta S_{A_l}}\right) \left[\frac{Y^s}{R_\rho - 1} + \frac{1}{(1 - \gamma_f)\tilde{s}}\right]. \quad (2.58)$$

-0.75 = 0.04 - 0.18 - 0.61

Fig. 2.11 shows these two measures of the total diapycnal fluxes of salt and temperature as a function of the exaggeration factor and the stability ratio for Prandtl numbers of 0.3, 1 and 10. For $\sigma = 0.3$ the values of the nondimensionalized total diapycnal fluxes of salt and temperature are both significantly less than their counterparts when $\sigma = 1$ or $\sigma = 10$. For $\sigma = 1$, in the case of salt, this nondimensional measure varies from -0.48 to -0.28 while in the case of temperature, the nondimensional ratio varies from -1 to -0.7. Concentrating on the particular case when the exaggeration factor is 25 and the stability ratio is 2, equation 2.57 is about -0.29 and equation 2.58 is about -0.75. At these values of the exaggeration factor and the stability ratio we see from Fig. 2.8 that $a^s \approx 0.06$ and $a^s/(\gamma_f \gamma_{\text{diff}}^s) \approx 0.83$ so that the leading terms on the right-hand sides of equations 2.57 and 2.58 are $\frac{1}{2}(1 - a^s) \approx 0.47$ and $\frac{1}{2}(\gamma_f - a^s/\gamma_{\text{diff}}^s) \approx 0.04$. These are the average fluxes across the double-diffusive interfaces, and they are positive. It follows that the dominant contributions to the total diapycnal fluxes of heat and salt in these steady-state intrusions come from the advection of salt and heat, that is, from the spatial correlations of $w'(S'_A + \frac{h}{4}s^{-1}\bar{S}_{Ax})$ for salt and of $w'(\Theta' + \frac{h}{4}s^{-1}\bar{\Theta}_x)$ for temperature (see equations 2.48 and 2.53). The first of the spatial correlation terms, $w'S'_A$ and $w'\Theta'$ represent the contribution from the correlations at a given point in space, while the second terms $\frac{h}{4}s^{-1}w'\bar{S}_{Ax}$ and $\frac{h}{4}s^{-1}w'\bar{\Theta}_x$, represent the correlations arising from doing the spatial average in the horizontal direction (see Fig. 2.1), and these are the dominant terms.

The numbers that appear in the second line of equations 2.57 and 2.58 represent the values of the terms above them when the exaggeration factor is 25 and the stability ratio is 2. It is seen that the salt flux across the finger interfaces dominates that across

the diffusive interfaces, and the resulting average salt flux is directed downward (0.47), in the downgradient direction. It is the vertical advection of the salinity perturbations in the intrusions (-0.76) that overpowers this downgradient salt diffusion, and most of the negative contribution of this advection comes from the horizontal spatial salinity correlation (-0.61), not the salinity perturbation at a fixed location (-0.15).

The corresponding situation for temperature is apparent from the numbers on the second line of equation 2.58. It is seen that the temperature flux across the finger interfaces slightly exceeds that across the diffusive interfaces, and the resulting average salt flux is directed downward (+0.04), in the downgradient direction. It is the vertical advection of the temperature perturbations in the intrusions (-0.79) that counteracts this small downgradient temperature diffusion, and most of the negative contribution of this advection comes from the horizontal spatial correlation (-0.61), not from the temperature and vertical velocity correlations at a fixed location (-0.18).

These results for the dominance of the upgradient advection of both salt and heat are in agreement with the inferences made by McDougall (1985b), but it must be said that McDougall (1985b) ignored the dominant advective correlation, namely that between the vertical velocity and the horizontally varying salinity and temperature fields. The take-home message from this analysis of the total diapycnal flux of salt and heat in double-diffusive intrusions at finite-amplitude steady state is that the total diapycnal flux of salt is $\sim 38\%$ smaller ($-0.29/0.47 \approx -0.62$) than one might deduce from purely knowledge of the fluxes across the finger and diffusive interfaces, and, most importantly, the total salt flux is going in the opposite direction to these driving interfacial double-diffusive fluxes. That is, the total diapycnal flux of salt is upgradient, in the sense of a negative diffusion coefficient. The corresponding take-home message for the total diapycnal flux of temperature is that it is 19 times ($-0.75/0.04 = -18.75$) what would be deduced from only knowledge of the fluxes across the finger and diffusive interfaces. Again, this flux of temperature is upgradient, in the sense of a negative diapycnal diffusivity of temperature.

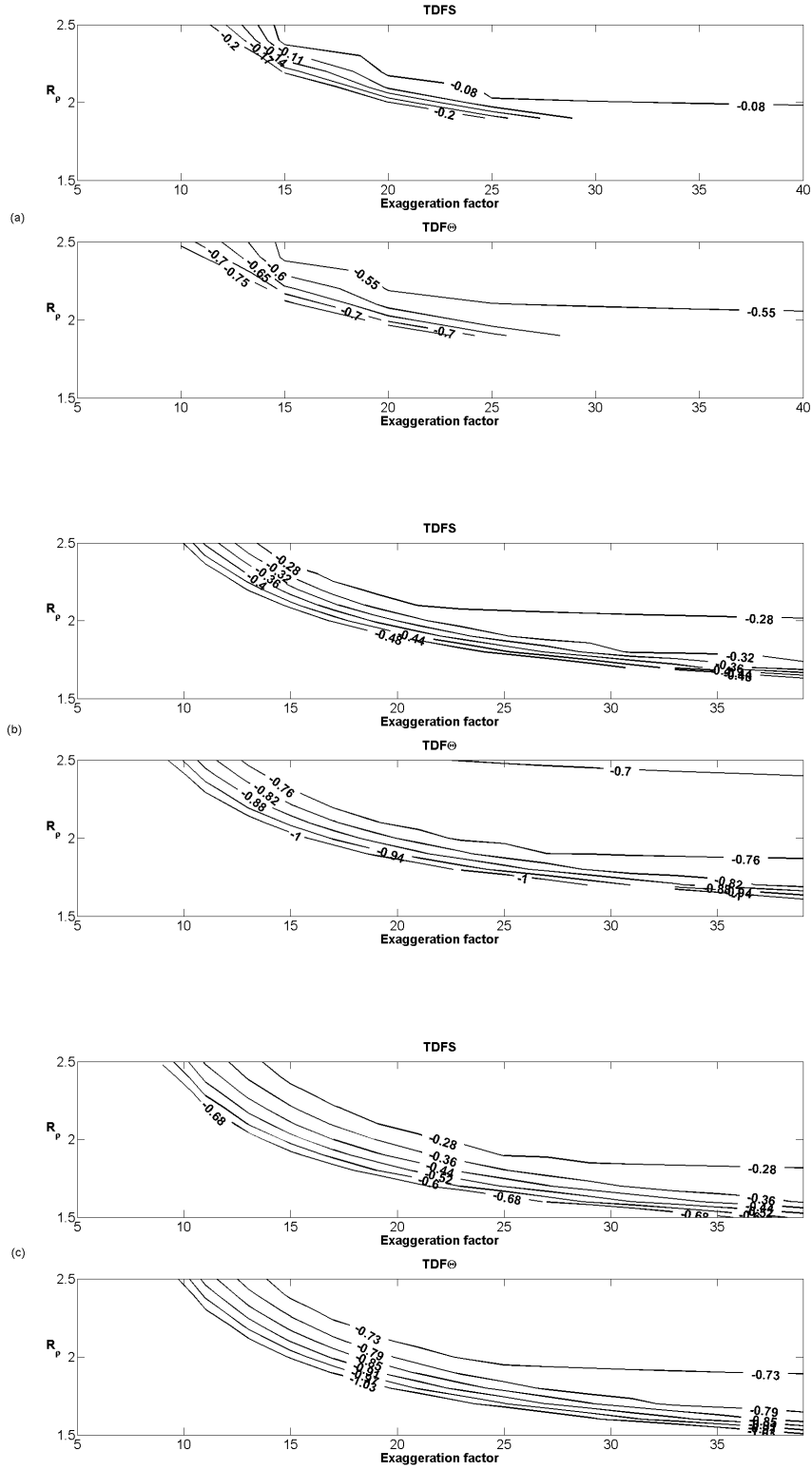


Figure 2.11: The values of the total diapycnal fluxes in terms of F_f^{SAs} . These panels are plots of equations 2.57 and 2.58 and the values are substantially negative. Three values for Prandtl number are selected: (a) $\sigma = 0.3$, (b) $\sigma = 1$ and (c) $\sigma = 10$.

2.9 Discussion

McDougall (1985b) gave a plausible analysis of the feasibility of the existence of a steady state for finite-amplitude double-diffusively driven intrusions by analysing how the double-diffusive fluxes and advective fluxes evolve and finally balance in both temperature and salinity, and he developed expressions for some properties of the steady state such as the vertical velocity and the total diapycnal fluxes.

The present chapter extends the approach of McDougall (1985b), and consequently the basic assumptions of this model are the same as that of McDougall (1985a) and McDougall (1985b). We take the buoyancy-flux ratio of salt fingers γ_f as the fixed value 0.5, and we consider only the case where the salinity and temperature of the ocean increase with height so that the basic stratification is salt-fingering favourable. Moreover, we take the vertical structure of the property perturbations to be square-waved since we believe this is appropriate when considering laboratory-based flux laws that vary as the $4/3$ power of property contrasts. The laboratory flux laws are taken from McDougall and Taylor (1984) for finger interfaces and from Huppert (1971) for diffusive interfaces.

This study complements those of Walsh and Ruddick (1998), Merryfield (2000) and Mueller et al. (2007) who have studied the formation of intrusions in a continuously stratified fluid, specifying turbulent diffusivities for salt, heat and momentum as functions of the stability ratio and the Froude number. Walsh and Ruddick (1998) confirmed that a steady state is possible and that this is achieved after each alternate interface is in the diffusive sense. These studies had the double-diffusive fluxes as general power laws of the stability ratio, whereas we have adopted the laboratory-based flux laws, albeit with an extra multiplicative exaggeration factor for the diffusive flux law. In addition, in contrast to these papers, we concentrate on the magnitude and signs of the total diapycnal fluxes of heat and salt in the steady-state intrusions. In this study, we made a linear transition from the initial state to the steady state (referring to equations 2.19 - 2.22), based on the momentum equation. This fundamental assumption is made because it is inappropriate to apply the momentum equation of the exponentially growing solution through all three stages, and we certainly know that if a steady state is achieved, the growth rate with respect to time has to be zero,

which gives another equation for the horizontal velocity (equation 2.20). This linear transitioning of the momentum equation is an assumption that is not needed at large values of the turbulent Prandtl number.

The main result of the present chapter is that we have been able to achieve steady-state double-diffusively driven intrusions by using the laboratory flux laws, but that in order to find these steady-state solutions we have found that the strength of the fluxes across the diffusive interfaces need to be increased significantly (by at least an order of magnitude) above the laboratory-determined values, relative to the laboratory-based finger fluxes. One way of rationalizing this need for an “exaggeration ratio” is that the laboratory experiments are performed with interfacial property contrasts that are much larger than oceanic ones. Another explanation might be that when an interface is near to becoming statically unstable, convectively driven turbulence is established and this will change the effective flux ratio of heat and salt across the interface. This effect was parameterized in the study of Mueller et al. (2007) but has not been included in the present study.

We have also quantified the total diapycnal fluxes of heat and salt, taking into account the advection of the perturbations in the steady state as well as the interfacial double-diffusive fluxes themselves. An important new aspect of this study is the realization that it is the spatial correlations of the diapycnal velocity of the intrusions with the temperature and salinity perturbations that make the largest contribution to the upgradient fluxes of heat and salt (see the large -0.61 numbers in equations 2.57 and 2.58); this important feature was missed by previous studies, including that of McDougall (1985b) and it is the spatial correlation that makes the total diapycnal flux of salt be upgradient. We have shown that the total diapycnal fluxes of both Absolute Salinity and Conservative Temperature are upgradient, that is, both are in the sense of a negative vertical diffusion coefficient.

Perhaps the largest assumption that we have made is that if a steady state is achieved in salinity and temperature, then a steady state will also be achieved in momentum so that the lateral velocity of the interleaving motions becomes constant rather than continuing to accelerate. This assumption is not needed for very large Prandtl number (since the left-hand side of equation 2.18 tends to zero at infinite Prandtl num-

ber), but it was invoked via our equations 2.21 and 2.22, which ensure that if or when the salt and heat equations evolve to a steady state, then the interleaving velocity will also approach a constant value at this stage. As a partial test of the sensitivity of our results to this assumption, we have performed some runs where $G(Y)$ was simply put equal to the initial value G^0 . In practice, this means that at all stages of the process the velocity of the intrusions will be accelerating since equation 2.18 indicates that the dimensional growth rate $\hat{\lambda}$ would remain positive. For the case $\sigma = 1$ we find that a steady state in temperature and salinity is still reached in this situation with $G(Y) = G^0$, albeit at values of X^s and Y^s that are reduced by approximately 15% and 5%, respectively. In this situation, the minimum exaggeration factor required to reach a steady state in temperature and salinity is larger by approximately 30%, and, interestingly, the ratio of the negative diffusivities of temperature and salinity is still close to unity, with the figure corresponding to Fig. 2.12 (b) showing a rather uniform increase of only 0.05. This indicates that our conclusions are not very sensitive to the proportionality factor between the horizontal velocity and the density perturbation of each intrusion (see equations 2.21 and 2.22). However, if a steady state is to be achieved then the horizontal velocity also needs to converge to a constant and for noninfinite Prandtl numbers, this aspect of this study remains an assumption.

These effective negative diffusion coefficients for both temperature and salinity (and density) when considering the total effect of both double diffusion and advection will surely have implications for how these interleaving motions can or should be parameterized in intermediate-scale and large-scale ocean models. For example, we suggest that it is appropriate to take the vertical eddy diffusivity of temperature and salinity in an ocean model (which represents regular small-scale turbulent mixing) and to reduce it differently for temperature and for salinity to account for double-diffusive interleaving while running an ocean model. It would be wise of course to not let the total eddy diffusivity of either temperature or salinity to go negative, or the numerical model will surely exhibit instabilities.

If a certain negative vertical diffusivity for salinity were decided upon to represent the effects of double-diffusive interleaving in an ocean model, then the magnitude of the appropriate negative vertical diffusivity for temperature would be larger by the

ratio $\alpha\text{TDF}\Theta/(R_\rho\beta\text{TDFS})$ and we plot this ratio in Fig. 2.12. It is seen that when the Prandtl number is not less than 1, this ratio $\alpha\text{TDF}\Theta/(R_\rho\beta\text{TDFS})$ is not a particularly strong function of the stability ratio R_ρ and that it is not very different from unity over much of Fig. 2.12, especially for exaggeration factor less than 20. This suggests that for $\sigma \geq 1$ finite-amplitude double-diffusively driven interleaving has the net effect of simply reducing the vertical turbulent diffusivity of both temperature and salinity and therefore of density, thus making it harder to balance the diapycnal transport implied by the production rate of bottom water. In other words, since double-diffusively driven interleaving motion acts like a negative diffusivity of heat, salt and density with almost equal negative vertical diffusion coefficients, a given amount of upward diapycnal motion requires larger turbulent diapycnal mixing in order to combat the effects of the interleaving process. Thus we see that double-diffusively driven interleaving acts in a similar fashion to thermobaricity and cabbeling Klocker and McDougall (2010) in that the presence of these three processes means that more intense mixing from the breaking of internal gravity waves is required in order to achieve a given amount of diapycnal advection.

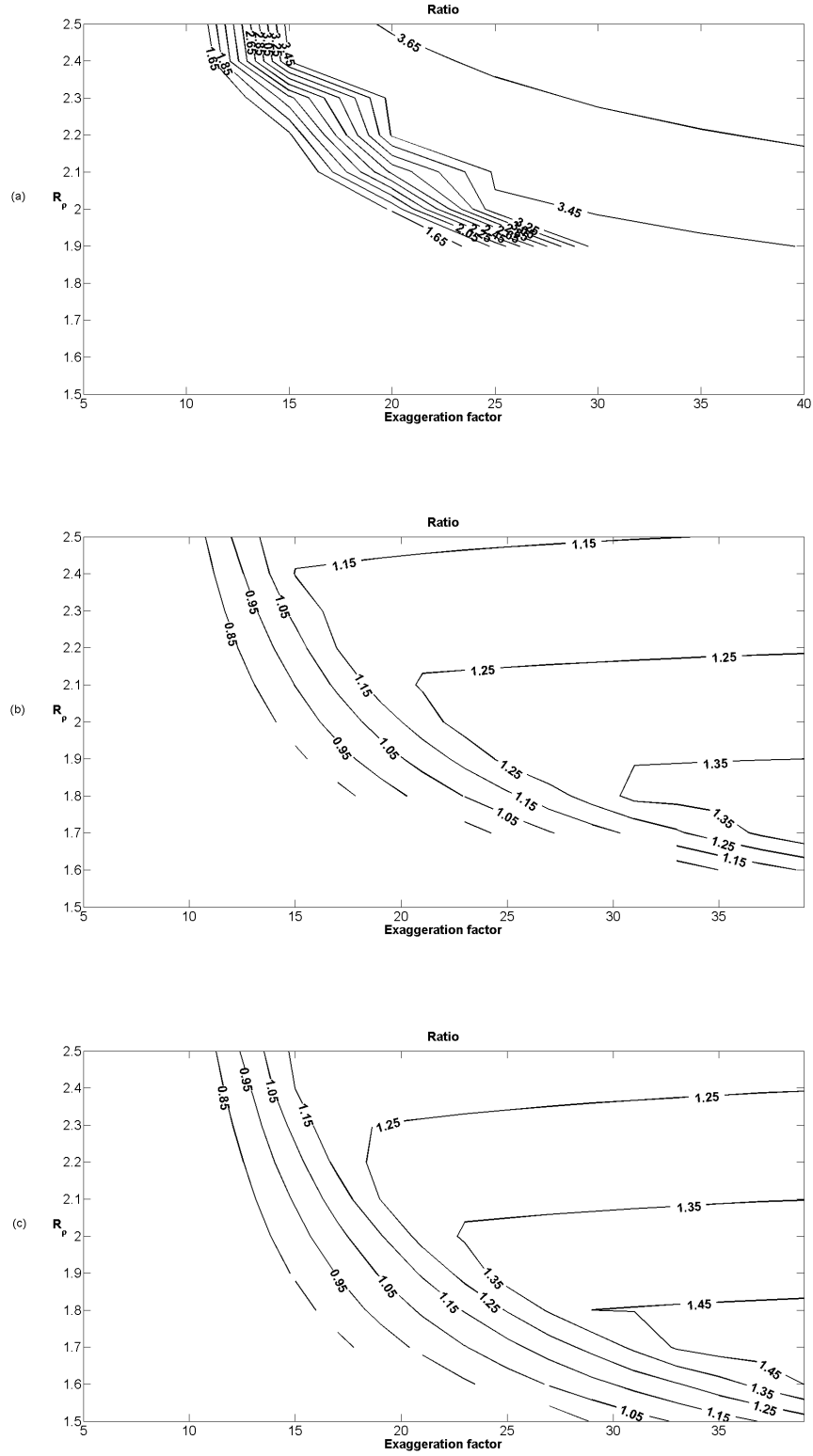


Figure 2.12: The ratio $\alpha TDF\Theta / (R_\rho \beta TDFS)$, being the ratio of the negative effective vertical diffusion coefficient for temperature to that for salt. This is the ratio of the numbers in the two panels in Fig. 2.11, divided by R_ρ . Three values of the Prandtl number are selected: (a) $\sigma = 0.3$, (b) $\sigma = 1$ and (c) $\sigma = 10$.

Chapter 3

Horizontal Residual Mean: Addressing the Limited Spatial Resolution of Ocean Models

3.1 Introduction

The stirring and mixing of tracers by mesoscale eddies in the ocean interior is thought to occur along locally-referenced potential density surfaces [Griffies (2004); McDougall and Jackett (2005); McDougall et al. (2014) and McDougall et al. (2017)]. The justification for this “epineutral” direction of mesoscale mixing relies on the observation that density overturns in the ocean interior are observed only at small scales ($< 1\text{m}$) during active three-dimensional turbulence. The mixing due to such small-scale three-dimensional turbulence is best understood and parameterized as isotropic turbulent diffusion (although this type of mixing is often called “diapycnal mixing”). The remaining mixing processes in the ocean interior occur along locally-referenced potential density surfaces as if there were no small-scale density overturns [McDougall et al. (2014)]. This decomposition is justified by ocean observations at the fine- and micro-scales and motivates the standard approach, in oceanographic theory and modelling, of representing mixing of tracers as the sum of epineutral mixing by mesoscale eddies and isotropic mixing by small-scale turbulence.

A key development in modelling ocean mixing was made by Gent and McWilliams

(1990). These authors realized that the epineutral diffusion of scalars would be affected by lateral variations of the thickness between pairs of closely spaced isopycnals, and they proposed a parameterization that acted as a sink of gravitational potential energy via the diffusion of this thickness. At the time it was thought that the Gent and McWilliams (1990) parameterization acted in a diabatic manner, increasing the amount of diapycnal mixing. However, Gent et al. (1995) showed that the parameterization could be represented as an extra non-divergent velocity that advects ocean tracers in an adiabatic and isohaline manner.

McDougall and McIntosh (2001) subsequently showed that the Gent and McWilliams (1990) procedure was a parameterization of the eddy contribution to the Temporal Residual Mean (TRM) circulation. The concept of residual mean circulation is common in atmospheric science, where the mean circulation is calculated from a zonal average [Andrews and McIntyre (1976)]. By contrast, the TRM velocity involves temporal averaging at a fixed longitude and latitude. The TRM theory of McDougall and McIntosh (2001) introduced a two-dimensional quasi-Stokes streamfunction to represent the extra non-divergent advection due to eddies (the quasi-Stokes velocity). The total TRM velocity is then the sum of the Eulerian mean velocity and the eddy-induced quasi-Stokes velocity. McDougall and McIntosh (2001) showed that the product of the lateral diffusivity and the slope of isopycnals used by Gent and McWilliams (1990) can be regarded as a parameterization of the quasi-Stokes streamfunction.

McDougall and McIntosh (2001) also demonstrated an intuitive link between the quasi-Stokes velocity of the TRM circulation (which is based in Cartesian coordinates) and the eddy-induced extra advection caused by thickness-weighted averaging, which is the natural way of averaging in density coordinates. They showed that the quasi-Stokes velocity corresponds to the contribution of mesoscale eddies to the horizontal transport of seawater of a certain density class; namely, seawater that is denser than the density surface whose time-mean height is the height being considered. Thus, in TRM theory, eddy effects are implemented in the conservation equation for the scalar variables (such as temperature and salinity) by modifying both the advective velocity and the advected scalar field. This is in contrast to recent work on representing the role of mesoscale eddies in ocean models by parameterizing eddy effects directly in the

momentum equation [e.g. Young (2012); Maddison and Marshall (2013); Porta Mana and Zanna (2014)].

The Gent and McWilliams (1990) parameterization essentially represents the horizontal density flux due to unresolved *temporal* correlations between temperature (or salinity) and the horizontal velocity. In the same way, unresolved *spatial* correlations between temperature and horizontal velocity will contribute horizontal density fluxes that should be included in ocean models which carry scalar fields and velocities on a relatively coarse spatial grid. This type of unresolved spatial correlation, and its importance for the oceanic meridional heat transport, has been discussed by Rintoul and Wunsch (1991). They found that spatial smoothing significantly reduced the estimate of the northward heat flux across 36°N in the Atlantic, due to missing spatial correlations between velocity and temperature. Therefore, insufficient spatial resolution in the western boundary currents of geostrophic box inversions or numerical ocean simulations may result in under-estimation of the meridional heat flux.

McDougall (1998) considered the effect of spatial resolution limitations on the horizontal transport of seawater that is denser than the isopycnal whose average height is the height being considered. The term Horizontal Residual Mean (HRM) was coined to describe the total velocity that would include the extra advection of seawater of this density class due to the unresolved spatial correlations. McDougall (1998) also proposed an expression for the eddy-induced HRM streamfunction in terms of the vertical and horizontal shears of the resolved horizontal velocity and the resolved-scale slope of density surfaces. Thus, just as the quasi-Stokes advection of the TRM circulation can be regarded as the adiabatic way of including the horizontal density fluxes due to unresolved temporal correlations between temperature and horizontal velocity, so the eddy-induced advection of the HRM circulation can be regarded as the adiabatic way of including the horizontal density fluxes due to unresolved spatial correlations.

In this chapter, we translate the idea in McDougall (1998) of calculating the HRM streamfunction into a practical method that approximates the transport of seawater that is denser than the isopycnal whose spatially and temporally averaged height is the height one is considering. Expressions for approximating the transport are presented in section 3.2. In section 3.3 we demonstrate that the method of calculating the

streamfunction from coarsely-resolved model fields gives a good approximation to the corresponding transport of seawater that would be available in a finer resolution ocean model. In sections 3.4 and 3.5 we diagnose the contribution of the extra non-divergent advection to basin-scale meridional heat and mass transports contained in a model snapshot. Section 3.6 justifies the non-tapering choice of the HRM method. Section 3.7 demonstrates an alternative way of calculating the HRM transport. By comparison, we showed that the method we proposed is adaptable to different ocean models. We summarize findings in section 3.8.

3.2 Expressions for the extra non-divergent advection of HRM

3.2.1 The expression of McDougall (1998) for the HRM streamfunction

The three-dimensional residual mean concept of McDougall (1998) provides an expression for the spatially integrated transport of ‘marked fluid’, being the fluid that lies below the density surface whose average height is the height being considered. The bulk of this transport is due to the resolved velocity on the coarse-resolution grid; part is due to subgrid-scale spatial variations of horizontal velocity and density, and part is due to any unresolved temporal correlations of the horizontal velocity and density. The mean northward transport of marked fluid is given by the left-hand side of 3.1 and this has been decomposed into the three terms on the right-hand side by McDougall (1998) as

$$\begin{aligned}
 & \int_{-\Delta x/2}^{\Delta x/2} \overline{\int_{-H}^{\bar{z}_a(x) + \eta'_a(x,t)} v dz} dx = \\
 & \int_{-\Delta x/2}^{\Delta x/2} \int_{-H}^{\langle \bar{z}_a \rangle} \bar{v} dz dx + \int_{-\Delta x/2}^{\Delta x/2} \int_{\langle \bar{z}_a \rangle}^{\bar{z}_a(x)} \bar{v} dz dx + \int_{-\Delta x/2}^{\Delta x/2} \overline{\int_{\bar{z}_a(x)}^{\bar{z}_a(x) + \eta'_a(x,t)} v dz} dx,
 \end{aligned} \tag{3.1}$$

where v is the northward velocity, x is zonal distance and z is height. The over-bars represent a temporal average and the angle brackets denote a boxcar x -average over distance Δx . The sea floor is at $z = -H$ and $\langle \bar{z}_a \rangle$ is the spatially and temporally averaged height of the locally-referenced potential density surface whose instantaneous height at longitude x is

$$\begin{aligned}
 z_a(x, t) &= \bar{z}_a(x) + \eta'_a(x, t) + \dots \\
 &= \langle \bar{z}_a \rangle + L^x x + \eta'_a(x, t) + \dots,
 \end{aligned} \tag{3.2}$$

and the perturbation height $\eta'_a(x, t)$ has zero temporal average. L^x is the mean slope of the locally-referenced potential density surface in the x direction. Fig. 3.1 illustrates the different heights used in equations 3.1 and 3.2. The curved line shows a snapshot of the instantaneous height of a density surface $z_a(x, t)$, which is a function of longitude

and time. $\bar{z}_a(x)$ is the temporal average of $z_a(x, t)$ and is illustrated by the sloping straight blue line in Fig. 3.1. $\langle \bar{z}_a \rangle$ is the average height of $\bar{z}_a(x)$, namely the temporal and spatial average of the instantaneous density surface $z_a(x, t)$. It is independent of time and location, hence is considered as the height at which the transport is calculated.

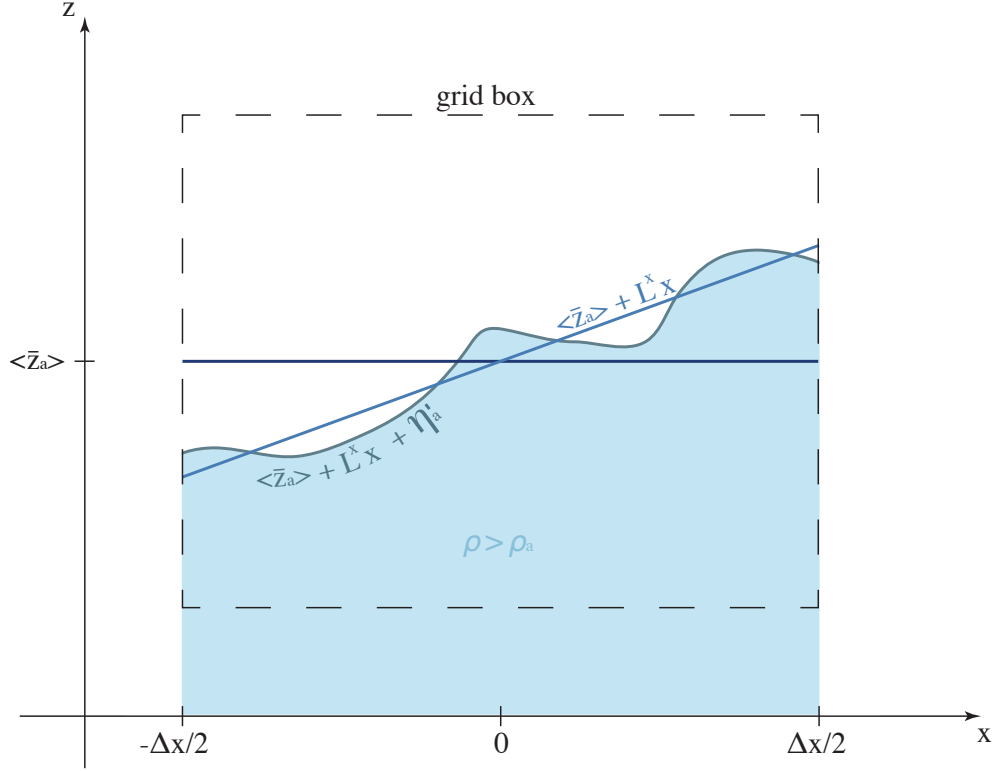


Figure 3.1: An illustration of the different height variables in equations 3.1 and 3.2. The curved line shows a snapshot of the instantaneous height of a density surface, which is denoted as $z_a(x, t)$ [see 3.2]. $\bar{z}_a(x)$ is illustrated by the straight blue line. $\langle \bar{z}_a \rangle$ is the average height of $\bar{z}_a(x)$, namely the temporal and spatial average of the instantaneous density surface $z_a(x, t)$.

The first term on the right hand side of equation 3.1 can be written as

$$\Delta x \int_{-H}^{\langle \bar{z}_a \rangle} \langle \bar{v} \rangle dz \quad (3.3)$$

so that this term gives the transport from the bottom of the ocean up to $\langle \bar{z}_a \rangle$ due to

the resolved-scale Eulerian velocity $\langle \bar{v} \rangle$, noting that Δx is the absolute value of the horizontal width of the model grid box in the x direction. We interpret the resolved northward velocity of a coarse resolution ocean model as the boxcar x -average of the temporal mean velocity at fixed height, $\langle \bar{v} \rangle$. Since the geostrophic relationship inherently yields the spatially averaged velocity rather than, say, the velocity at the centre of the face, this is the only interpretation that is consistent with geostrophy. Hence the first term in equation 3.1 is the northward flux of marked fluid that can be calculated using the model's resolved velocity.

In order to evaluate the second term in equation 3.1, the Eulerian-mean northward velocity \bar{v} is written as a spatial Taylor series,

$$\bar{v} = \bar{v}(x, z) = \bar{v}_0 + \bar{v}_x x + \bar{v}_z(z - \langle \bar{z}_a \rangle) + \dots \quad (3.4)$$

where \bar{v}_x and \bar{v}_z are understood to be evaluated at $z = \langle \bar{z}_a \rangle$ and at the centre of the box in the x direction (that is, at $x = 0$), while \bar{v}_0 is independent of both x and z . Substituting this Taylor series into the middle term in equation 3.1, McDougall (1998) obtained

$$\int_{-\Delta x/2}^{\Delta x/2} \int_{\langle \bar{z}_a \rangle}^{\bar{z}_a(x)} \bar{v} dz dx = \frac{1}{12} \langle \bar{v} \rangle_x L^x [\Delta x]^3 + \frac{1}{24} \langle \bar{v} \rangle_z (L^x)^2 [\Delta x]^3 + O([\Delta x]^4). \quad (3.5)$$

The transport anomaly due to the horizontal shear (first term on the right-hand side of equation 3.5) clearly depends on this shear $\langle \bar{v} \rangle_x$, times the horizontal distance. Whether this anomaly of volume transport should be added to or subtracted from the Eulerian-mean transport also depends on the sign of the slope L^x of the density surface. On the other hand, the transport anomaly due to the vertical shear (second term on the right-hand side of equation 3.5) involves the perturbation velocity which is the product of this shear $\langle \bar{v} \rangle_z$, with the vertical height anomaly, itself proportional to L^x . As a result, this transport anomaly attracts an additional power of the slope: it is proportional to $\langle \bar{v} \rangle_z (L^x)^2$, which has the same sign as the vertical shear. The analogue to equation 3.5, for the eastward transport is

$$\int_{-\Delta y/2}^{\Delta y/2} \int_{\langle \bar{z}_a \rangle}^{\bar{z}_a(y)} \bar{u} dz dy = \frac{1}{12} \langle \bar{u} \rangle_y L^y [\Delta y]^3 + \frac{1}{24} \langle \bar{u} \rangle_z (L^y)^2 [\Delta y]^3 + O([\Delta y]^4). \quad (3.6)$$

The inner integral of the third term in equation 3.1 is what appears in the Taylor series analysis of the TRM theory of McDougall and McIntosh (2001) so that we can write this integral as

$$\overline{\int_{\bar{z}_a(x)}^{\bar{z}_a(x)+\eta'_a(x,t)} v dz} = \left(-\frac{\overline{v'\gamma'}}{\bar{\gamma}_z} + \frac{\bar{v}_z}{\bar{\gamma}_z} \frac{\bar{\phi}}{\bar{\gamma}_z} \right) \Big|_{z=\bar{z}_a(x)} + O(\alpha^3), \quad (3.7)$$

which is the northward component of the quasi-Stokes streamfunction of the purely temporal-residual-mean velocity, evaluated at the height $z = \langle \bar{z}_a \rangle$. In equation 3.7, γ stands for the locally-referenced potential density, and $\bar{\phi} \equiv \frac{1}{2} \overline{(\gamma')^2}$ is half the density variance at height z . The overbar denotes a temporal average and the prime indicates perturbation. The last term in equation 3.1 is thus Δx times the streamfunction of the TRM quasi-Stokes velocity.

Hence the contribution of unresolved spatial correlations to the HRM streamfunction arises from the second term on the right-hand side of equation 3.1, which, when written using a spatial Taylor series, becomes equations 3.5 and 3.6. These expressions are the focus of the present work. The right-hand sides of equations 3.5 and 3.6 do not require a parameterization, but rather can be evaluated using the variables that are available to a coarse-resolution ocean model. McDougall (1998) derived the above equations but no diagnosis or evaluation of the horizontal residual mean transport has been conducted to date. McDougall (1998) also hypothesized that the first term in the right-hand sides of equation 3.5 would be the dominant term in western boundary currents, which we will confirm in our study.

In the following, we will use numerical output from the MOM5 ocean model [Griffies 2012], run at a horizontal resolution of 1/4 degree. The output is from a 300-year control run from a coupled ocean, ice, atmosphere ACCESS (Australian Community Climate and Earth-System Simulator) model configuration. The model we used is MOM5 (Modular Ocean Model). This model uses B-grid with velocities located at the northeastern lower vertex of each tracer box. MOM5 is a tripolar global model. The output is calculated globally, but the HRM method is demonstrated in only three most significant areas, which are the Gulf Stream area, the East Australian Current area and the Antarctic Circumpolar Current area. We boxcar averaged the model output over three grid boxes to construct a coarse-resolution data set. The 1/4-degree and

3/4-degree datasets are then used to calculate the transport separately. The results are compared to demonstrate that the HRM Taylor series expressions of equations 3.5 and 3.6, which rely on the coarse-resolution data, do approximately capture the horizontal transport of the fine-resolution model output.

3.2.2 Estimating the HRM streamfunction from coarse-resolution model fields

The horizontal residual mean (HRM) transport is the total transport of water of a certain density class induced by the sum of the Eulerian-mean velocity of a coarse-resolution model and plus the extra velocity that arises from the spatial correlations of velocity and density within a grid box of a coarse-resolution ocean model that are not captured by the model data at this coarse spatial resolution. The additional quasi-Stokes streamfunction of the TRM transport is also needed to account for the unresolved temporal correlations of mesoscale eddies in a coarse-resolution model.

This right-hand side of equation 3.8 is calculated using a spatial Taylor series expansion from a certain height $\langle \bar{z}_a \rangle$ to a locally-referenced potential density surface whose height $z_a(x)$ is assumed to be a linear function of its zonal position. In this study, $\langle \bar{z}_a \rangle$ is the depth level of an ocean model and in order to evaluate the streamfunction on a sufficiently small horizontal footprint, we allow the linear variation of $z_a(x)$ to be different to the west and to the east of the central longitude. The name “residual” applies to the total transport, which includes the Eulerian mean streamfunction as well as the extra streamfunction that we calculate below and also the quasi-Stokes streamfunction of the TRM formulation.

Equation 3.8 below calculates the extra transport (extra compared with the Eulerian mean transport) in the northward direction that is denser than the density surface whose average height is $\langle \bar{z}_a \rangle$.

$$\begin{aligned}
\int_{-\Delta x/2}^{\Delta x/2} \int_{\langle \bar{z}_a \rangle}^{\bar{z}_a(x)} (\bar{v} - \bar{v}_0) dz dx &= \frac{1}{24} \langle \bar{v} \rangle_x L_E^x [\Delta x]^3 + \frac{1}{24} \langle \bar{v} \rangle_x L_W^x [\Delta x]^3 \\
&+ \frac{1}{48} \langle \bar{v} \rangle_z (L_E^x)^2 [\Delta x]^3 + \frac{1}{48} \langle \bar{v} \rangle_z (L_W^x)^2 [\Delta x]^3 \\
&\text{height-adjustment term} + O([\Delta x]^4).
\end{aligned} \tag{3.8}$$

The Eulerian-mean spatially-averaged velocity evaluated at fixed height is labeled \bar{v}_0 . The first four terms on the right-hand side here are equivalent to the two terms on the right-hand side of equation 3.5, with each term now applying to either the eastern or western half of the box of width Δx . There is an additional term that must appear in 3.8 because with different slopes, L_E^x to the east and L_W^x to the west, the straight lines emanating from $\langle \bar{z}_a \rangle$ to the heights z_E and z_W respectively describe a surface whose average height over the length Δx of the box is greater than $\langle \bar{z}_a \rangle$ by

$$\begin{aligned}
\delta z &= \frac{1}{8} (z_E - \langle \bar{z}_a \rangle) + \frac{1}{8} (z_W - \langle \bar{z}_a \rangle) \\
&= \frac{1}{8} (L_E^x - L_W^x) \Delta x.
\end{aligned} \tag{3.9}$$

The heights z_E and z_W are the heights of the locally-referenced potential density surface that also passes through height $\langle \bar{z}_a \rangle$ at the central longitude. The casts that contain the points at z_E and z_W are separated by $2\Delta x$ in the west-east direction, being vertical casts of the coarse-resolution model to the east and west of the central cast.

Fig.3.2 illustrates the coarse and fine resolution grids considered here. The scale of the grid box in the low-resolution model is three times that of the fine resolution grid box, as shown in the central low-resolution box in Fig.3.2. The left-hand side of equation 3.8 is integrated up to the density surface whose heights are based on the tracer and velocity data that is available to the fine-resolution model. This integration of the transport using the fine-resolution model data is described in Appendix F. The right-hand side of equation 3.8 is calculated using the coarse-resolution data. The corresponding values are illustrated in Fig.3.2. Notice that the velocities are not on vertices of grid boxes as they should be in B-grid models. This is because the velocities used for calculating velocity shears are spatially averaged. More specifically, \bar{v}_W and \bar{v}_E are the average of velocities at upper and lower vertices of the western and eastern edges of the face, respectively. \bar{v}_{upper} and \bar{v}_{lower} are average velocities of adjacent vertices on

the upper and lower edges of a grid box face. They are averaged zonally for calculating the vertical shear in equation 3.13 and meridionally for the vertical shear in equation 3.14. In the remainder of this section we describe this procedure in more detail.

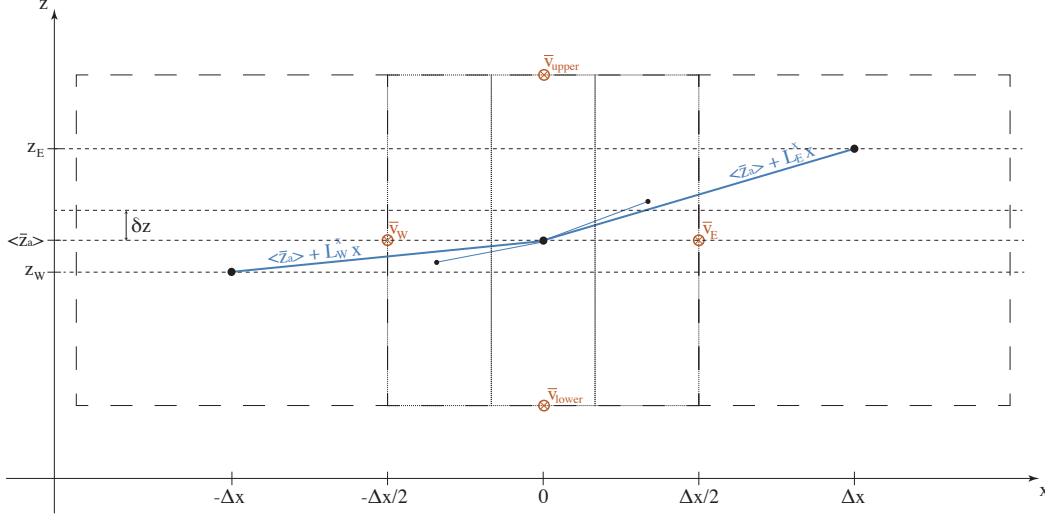


Figure 3.2: Vertical cross-section through three boxes of a coarse-resolution ocean model, with the central box showing three boxes of a finer resolution ocean model that has three times the horizontal resolution compared with the coarse resolution model. At the fine resolution boxes, density surfaces follow the lines from the central point to the small dots at points. The small dots mark intersects of the density surfaces and the tracer casts. At the coarse-resolution, density surfaces follow the lines from the central point to the larger dots. The large dots mark intersects of density surfaces and the tracer casts. The corresponding heights of intersects are denoted z_W for the western intersect and z_E for the eastern intersect. \bar{v}_W , \bar{v}_E , \bar{v}_{upper} and \bar{v}_{lower} are averaged velocities on the vertical and zonal directions, respectively. The velocities available in the model are originally on vertices of grid boxes. $\langle \bar{z}_a \rangle$ is the height that tracers are at and δz is the difference between the average height of density surfaces and $\langle \bar{z}_a \rangle$.

In the absence of the fifth term on the right-hand side of equation 3.8, this right-hand side would represent the Taylor series approximation to a density surface whose average height is $\langle \bar{z}_a \rangle + \delta z$. We take the vertical variation of the northward velocity across the whole width of the box at the height of the density surface to be approximately $\langle \bar{v} \rangle_z$

(which is actually the vertical gradient of the northward velocity evaluated at the fixed height $\langle \bar{z}_a \rangle$). The fifth term is responsible for the transport induced by allowing L_E^x and L_W^x to be different and it can be written in a form to be readily evaluated in a forward ocean model. The average perturbation northwards velocity along the thick blue line within the central low-resolution box is $\frac{1}{8}\langle \bar{v} \rangle_z (L_E^x - L_W^x) \Delta x$. The average perturbation northwards velocity that accounts for the average height adjustment is the extra velocity $\frac{1}{8}\langle \bar{v} \rangle_z (L_E^x - L_W^x) \Delta x - \frac{1}{2}\langle \bar{v} \rangle_z \delta z$, which can be simplified as $+\frac{1}{2}\langle \bar{v} \rangle_z \delta z$. The corresponding extra transport is $+\frac{1}{2}\langle \bar{v} \rangle_z \delta z$ times the area $|\delta z| \delta x$. All scenarios of different L_E^x and L_W^x lead to one additional term $-\frac{1}{2}\langle \bar{v} \rangle_z (\delta z)^2 \Delta x$ to be add on to equation 3.8. In any case, we find this term to be small compared with the other terms in equation 3.8. The complete equation 3.8 is given as

$$\begin{aligned} \int_{-\Delta x/2}^{\Delta x/2} \int_{\langle \bar{z}_a \rangle}^{\bar{z}_a(x)} (\bar{v} - \bar{v}_0) dz dx &= \frac{1}{24} \langle \bar{v} \rangle_x L_E^x [\Delta x]^3 + \frac{1}{24} \langle \bar{v} \rangle_x L_W^x [\Delta x]^3 \\ &+ \frac{1}{48} \langle \bar{v} \rangle_z (L_E^x)^2 [\Delta x]^3 + \frac{1}{48} \langle \bar{v} \rangle_z (L_W^x)^2 [\Delta x]^3 \\ &- \frac{1}{2} \langle \bar{v} \rangle_z (\delta z)^2 \Delta x + O([\Delta x]^4). \end{aligned} \quad (3.10)$$

On the coarse-resolution model grid, the values of the northward velocity can be estimated at the centres of the eastern, western, upper and lower edges of the northern face of each grid. In terms of these velocities the velocity shears are $\langle \bar{v} \rangle_x = (\bar{v}_E - \bar{v}_W)/\Delta x$ and $\langle \bar{v} \rangle_z = (\bar{v}_{upper} - \bar{v}_{lower})/\Delta z$, while the slopes of the density surface are $L_W^x = (\langle \bar{z}_a \rangle - z_W)/\Delta x$ and $L_E^x = (z_E - \langle \bar{z}_a \rangle)/\Delta x$. We note again that z_W and z_E are defined at the centres of the coarse-resolution boxes on either side of the central box. Using these expressions, the right-hand side of equation 3.10 can be written in terms of these coarse-resolution model variables as

$$\begin{aligned} \int_{-\Delta x/2}^{\Delta x/2} \int_{\langle \bar{z}_a \rangle}^{\bar{z}_a(x)} (\bar{v} - \bar{v}_0) dz dx &= \frac{1}{24} (\bar{v}_E - \bar{v}_W) (z_E - z_W) \Delta x \\ &+ \frac{1}{48} \frac{(\bar{v}_{upper} - \bar{v}_{lower})}{\Delta z} \left[(z_E - \langle \bar{z}_a \rangle)^2 + (z_W - \langle \bar{z}_a \rangle)^2 - 24(\delta z)^2 \right] \Delta x + O([\Delta x]^4). \end{aligned} \quad (3.11)$$

Using the expression 3.9 for δz , equation 3.11 can be rearranged as

$$\begin{aligned}
& \int_{-\Delta x/2}^{\Delta x/2} \int_{\langle \bar{z}_a \rangle}^{\bar{z}_a(x)} (\bar{v} - v_0) dz dx = \frac{1}{24} (\bar{v}_E - \bar{v}_W) (z_E - z_W) \Delta x \\
& + \frac{1}{48} \frac{(\bar{v}_{upper} - \bar{v}_{lower})}{\Delta z} \left[\frac{5}{8} (z_E - \langle \bar{z}_a \rangle)^2 + \frac{5}{8} (z_W - \langle \bar{z}_a \rangle)^2 - \frac{3}{4} (z_E - \langle \bar{z}_a \rangle) (z_W - \langle \bar{z}_a \rangle) \right] \Delta x \\
& + O([\Delta x]^4).
\end{aligned} \tag{3.12}$$

A more compact form of this equation is

$$\begin{aligned}
& \int_{-\Delta x/2}^{\Delta x/2} \int_{\langle \bar{z}_a \rangle}^{\bar{z}_a(x)} (\bar{v} - v_0) dz dx = \frac{1}{24} (\bar{v}_E - \bar{v}_W) (z_E - z_W) \Delta x \\
& + \frac{1}{48} \frac{(\bar{v}_{upper} - \bar{v}_{lower})}{\Delta z} \left[\frac{5}{8} (z_E - z_W)^2 + \frac{1}{2} (z_E - \langle \bar{z}_a \rangle) (z_W - \langle \bar{z}_a \rangle) \right] \Delta x + O([\Delta x]^4).
\end{aligned} \tag{3.13}$$

Correspondingly, the expression for the extra streamfunction of the HRM in the x direction is

$$\begin{aligned}
& \int_{-\Delta y/2}^{\Delta y/2} \int_{\langle \bar{z}_a \rangle}^{\bar{z}_a(y)} (\bar{u} - u_0) dz dy = \frac{1}{24} (\bar{u}_N - \bar{u}_S) (z_N - z_S) \Delta y \\
& + \frac{1}{48} \frac{(\bar{u}_{upper} - \bar{u}_{lower})}{\Delta z} \left[\frac{5}{8} (z_N - z_S)^2 + \frac{1}{2} (z_N - \langle \bar{z}_a \rangle) (z_S - \langle \bar{z}_a \rangle) \right] \Delta y + O([\Delta y]^4).
\end{aligned} \tag{3.14}$$

where, in this case, δz is

$$\begin{aligned}
\delta z &= \frac{1}{8} (z_N - \langle \bar{z}_a \rangle) + \frac{1}{8} (z_S - \langle \bar{z}_a \rangle) \\
&= \frac{1}{8} (L_N^y - L_S^y) \Delta y.
\end{aligned} \tag{3.15}$$

The right-hand sides of equations 3.13 and 3.14 are expressions for the contribution of the HRM transport of unresolved spatial correlations across the width of the boxes of horizontal size Δx and Δy . The corresponding streamfunction of the extra HRM velocity is found by dividing these equations by Δx and Δy respectively, so that

$$\Psi_{HRM}^y = \frac{1}{24} \langle \bar{v} \rangle_x (L_E^x + L_W^x) [\Delta x]^2 + \frac{1}{48} \langle \bar{v} \rangle_z \left[\frac{5}{8} (L_E^x + L_W^x)^2 - \frac{1}{2} L_E^x L_W^x \right] [\Delta x]^2 + O([\Delta x]^3), \tag{3.16}$$

$$\Psi_{HRM}^x = \frac{1}{24} \langle \bar{u} \rangle_y (L_N^y + L_S^y) [\Delta y]^2 + \frac{1}{48} \langle \bar{u} \rangle_z \left[\frac{5}{8} (L_N^y + L_S^y)^2 - \frac{1}{2} L_N^y L_S^y \right] [\Delta y]^2 + O([\Delta y]^3). \quad (3.17)$$

The extra horizontal velocities due to the HRM are then the vertical derivatives of these streamfunctions, with the vertical derivative of Ψ_{HRM}^x (defined in equation 3.17) being the eastward velocity component, and the vertical derivative of Ψ_{HRM}^y (defined in equation 3.16) being the northward velocity component.

In a similar way, the extra horizontal quasi-Stokes velocity of the Gent et al. (1995) form of the TRM velocity is the vertical derivative of $(\Psi_{TRM}^x, \Psi_{TRM}^y)$. On the eastern face of a coarse-resolution box the extra TRM streamfunction is given by $\Psi_{TRM}^x = -\kappa L_E^x$ while on the northern face it is given by $\Psi_{TRM}^y = -\kappa L_N^y$. Note that the eastward and northward components of the quasi-Stokes TRM streamfunction are proportional to (minus) the slopes of the density surfaces in these directions. In contrast, the dominance of the first terms in equation 3.16 and 3.17 (demonstrated in section 3.3) implies that the *eastward* component, Ψ_{HRM}^x , is proportional to the *northward* slope of the isopycnals and the *northward* component, Ψ_{HRM}^y , is proportional to the *eastward* slope of the isopycnals. Thus, the extra advection of HRM and that of TRM act in horizontal directions that are approximately perpendicular to one another.

The streamfunction of the total velocity field is the sum of (i) the Eulerian-mean streamfunction, $(\bar{\Psi}^x, \bar{\Psi}^y)$, (ii) the quasi-Stokes TRM streamfunction, and (iii) the quasi-Stokes HRM streamfunction, that is

$$\Psi_{Total}^x = \bar{\Psi}^x + \Psi_{TRM}^x + \Psi_{HRM}^x \quad \text{and} \quad \Psi_{Total}^y = \bar{\Psi}^y + \Psi_{TRM}^y + \Psi_{HRM}^y, \quad (3.18)$$

with the eastward components being evaluated on the eastern face of each coarse-resolution box, and northward component on the northern face of each coarse-resolution box. Since the quasi-Stokes streamfunction of the HRM can be readily evaluated using the variables that are available during the running of an ocean model, its adoption should be straightforward. Moreover, the evaluation of this streamfunction can be readily adjusted to the grid on which the model is formulated. This three-dimensional quasi-Stokes velocity of the HRM can be added to the Eulerian-mean velocity and the quasi-Stokes velocity of the TRM. The resulting total velocity can be used in ocean models' higher-order advection schemes.

3.3 Assessment of the method using 1/4-degree model snapshot

We use instantaneous model output from a global MOM5 forced ocean simulation at nominally 1/4-degree resolution. In order to construct a low-resolution dataset we boxcar average the model fields over three grid boxes, obtaining a zonal resolution of 3/4 of a degree. Another way to construct a coarse-resolution dataset from the original data is to subsample over three grid boxes. I have made comparison between these two methods of forming the low-resolution data sets and the results were not significantly different. The construction of the 3/4 degree resolution data may lead to a coarser boundary at some locations. For example, if two of three averaged 1/4 degree grid boxes are land and the other is sea, then after the box-car average, the whole degree grid box represents land. A linear extrapolation from sea towards land has been implemented to complete the HRM transport for boundary cells.

The right-hand side of equation 3.13 is an explicit way of calculating the HRM extra transport of water through a face of a grid box which is centered at height $\langle \bar{z}_a \rangle$ and has a zonal width of Δx . Every value used in this calculation can be obtained after simple and fast operations on the available data from an ocean model. The heights of the density surfaces, namely z_E , z_W , z_N and z_S , are calculated on the four vertical faces of each grid box by a fast computing algorithm developed by Riha (2017) for computing approximately neutral surfaces. Transports are still calculated face by face, and one face in our coarse-resolution calculation is three times as large as a face of the fine resolution calculation that is outlined in Appendix F. The other typical way of calculating the HRM extra transport of water is to compute using slopes of neutral density surfaces, as shown in equation 3.10 using L_E^x and L_W^x . This approach requires the simultaneous calculation of density differences when running the model.

The transport of water denser than the density surface whose average height perturbation is zero is given by the left-hand sides of equations 3.13 and 3.14. It is evaluated from the fine resolution model output at 1/4-degree zonal resolution, using the method described in Appendix F. In this section we compare these fine resolution estimates of the volume transport with those produced by the HRM Taylor series approach ap-

plied to the low-resolution data (right-hand sides of equations 3.13 and 3.14). The comparison is made in three areas: the Gulf Stream, the East Australian Current and the Antarctic Circumpolar Current. In this way, we examine two western boundary current regions as well as the eddy-rich Southern Ocean. We have calculated the quasi-Stokes HRM streamfunctions in both the zonal (eastward) and meridional (northward) directions.

3.3.1 Gulf Stream

We examined the region from about $32^\circ N$ to about $39^\circ N$ and from 382m to 1300m deep. Fig. 3.3 shows the fine resolution velocity field at a depth of 414m, to illustrate some features of the chosen area. The underlying colors indicate the fine-resolution current speed and the arrows indicate the fine-resolution velocities, but shown every three grid points to avoid cluttering. Within the Gulf Stream, the northward velocity first increases and then decreases with horizontal distance from the coast.

The comparisons of the transports estimated using the fine resolution model output (labeled LHS) and the coarse-resolution output (HRM estimates) is shown in Fig. 3.4 for five consecutive coarse resolution grid boxes from the coast. That is, the left-hand most data points in this figure begin at the first coarse-resolution box adjacent to the coast, and these may occur at different longitudes for the different depths shown. The changing sign of these streamfunctions is mainly caused by the change of sign of the zonal velocity shear, $\langle \bar{v} \rangle_x$; as already mentioned, the northward velocity first increases and then decreases with distance from the coast. Fig. 3.5 shows a scatterplot comparing these high and low resolution estimates of the meridional streamfunction in the Gulf Stream region. Most of the points stay close to the one-to-one line, but there is a clear indication that the low-resolution, Taylor-series derived estimate of the transport underestimates the true transport by a few tens of percent. The larger values of the streamfunction occur at relatively shallow depths, while most values at deeper levels are smaller.

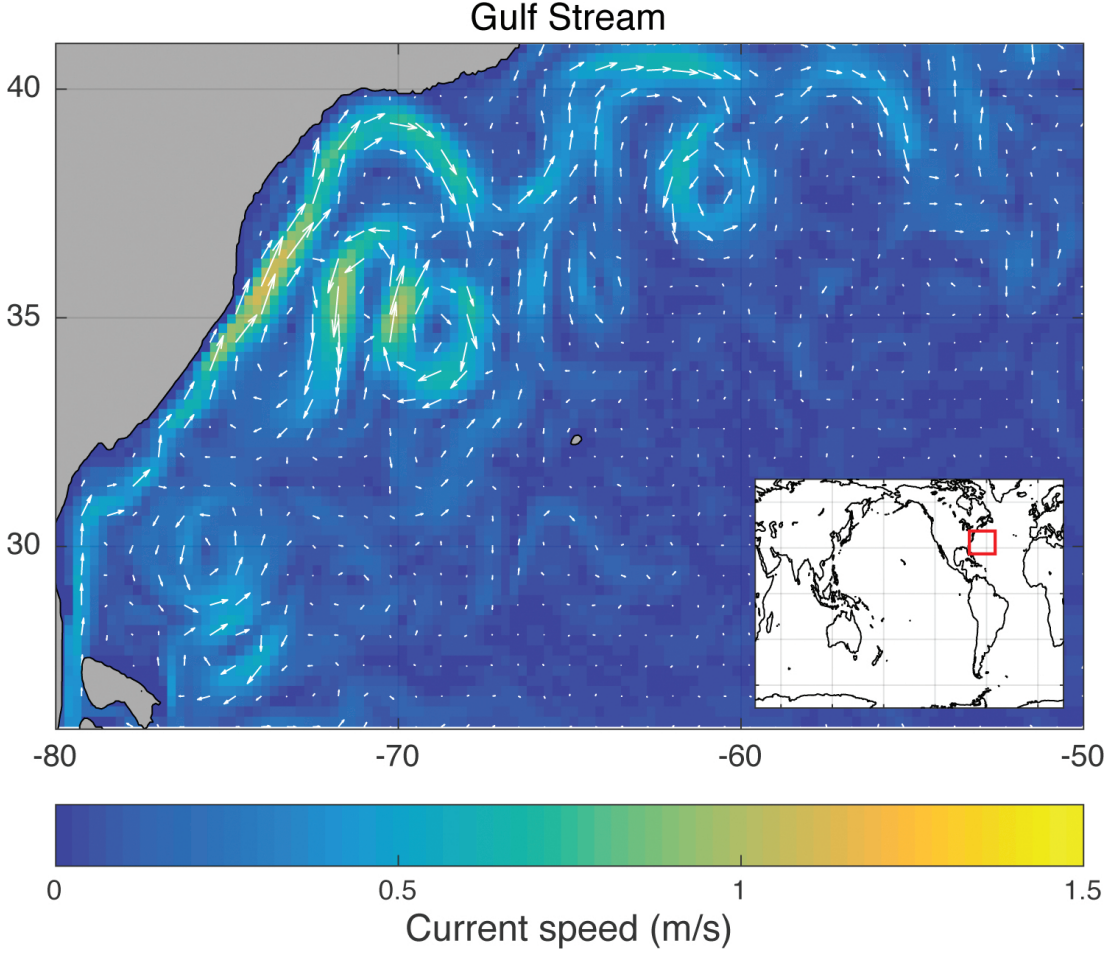


Figure 3.3: Fine-resolution current speeds of the Gulf Stream area at a depth of 414 m are shaded. Velocity arrows are overlain every three grid points.

3.3.2 East Australian Current

The region chosen for illustrating the transports in the East Australian Current is from 22S to 30S and the same depth range as in the Gulf Stream. A snapshot of the current speed at 414m is shown in Fig. 3.6 with the corresponding comparisons between the fine and coarse resolution estimates of the HRM streamfunction of equation 3.13 shown in Fig. 3.7 and 3.8. Although the coarse-resolution-based transport anomaly is generally of the same sign as the fine resolution one, the former tends to underestimate the latter by about a factor of 2. We interpret this underestimation as due to the narrowness of the simulated East Australian Current, which is confined to one or two grid cells along

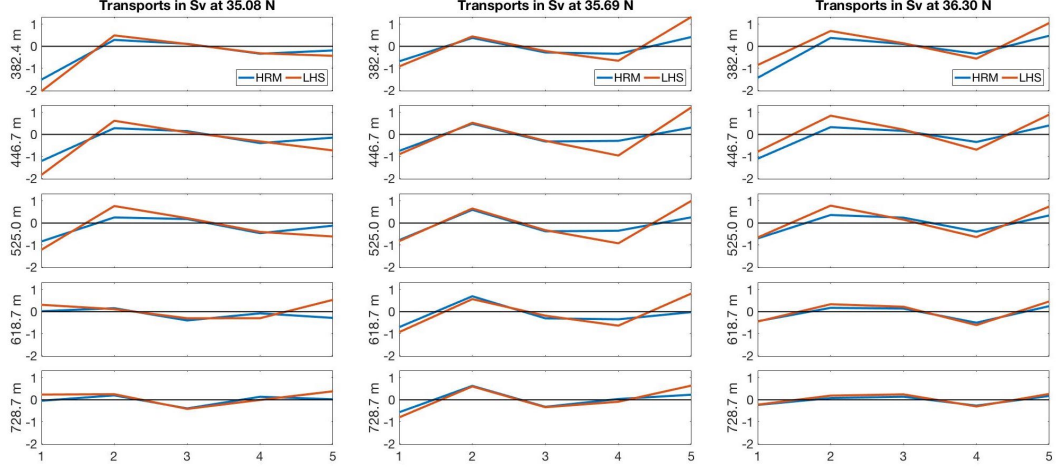


Figure 3.4: Comparison of the transports (in Sv; $1 \text{ Sv} = 10^6 m^3 s^{-1}$) calculated by the two methods at three different latitudes and five different depths in the Gulf Stream region. Red curves correspond to the two-triangle method of Appendix F which uses the high-resolution data, while the blue curves correspond to the right-hand side of equation 3.13 applied to the coarse-resolution fields. The x -axis is the number of coarse-resolution grid boxes from the coast.

the straight coast, causing partial failure of the Taylor-series approximation. Hence, in this boundary current region, the extra advection calculated from the coarse-resolution model fields only partly compensates for the missing spatial correlations. The impact of narrowness of the current also showed in the narrow start of Gulf Stream, around 30°N as shown in Fig. 3.3. The HRM method behaved poorly at that latitude.

3.3.3 Antarctic Circumpolar Current

We also show a comparison between the left and right hand sides of equations 3.13 and 3.14 for a representative subregion in the Antarctic Circumpolar Current (ACC). Fig. 3.9 shows a snapshot of the fine resolution velocity field of the chosen area at depth of 414m, illustrating the eddying nature of the ACC. Unlike previous two western boundary current areas, this area is an eddy-rich area. The eddies are predominantly eastward, as shown in Fig. 3.9. The Taylor-series approach of the quasi-Stokes HRM streamfunction quite accurately approximates the corresponding transport evaluated

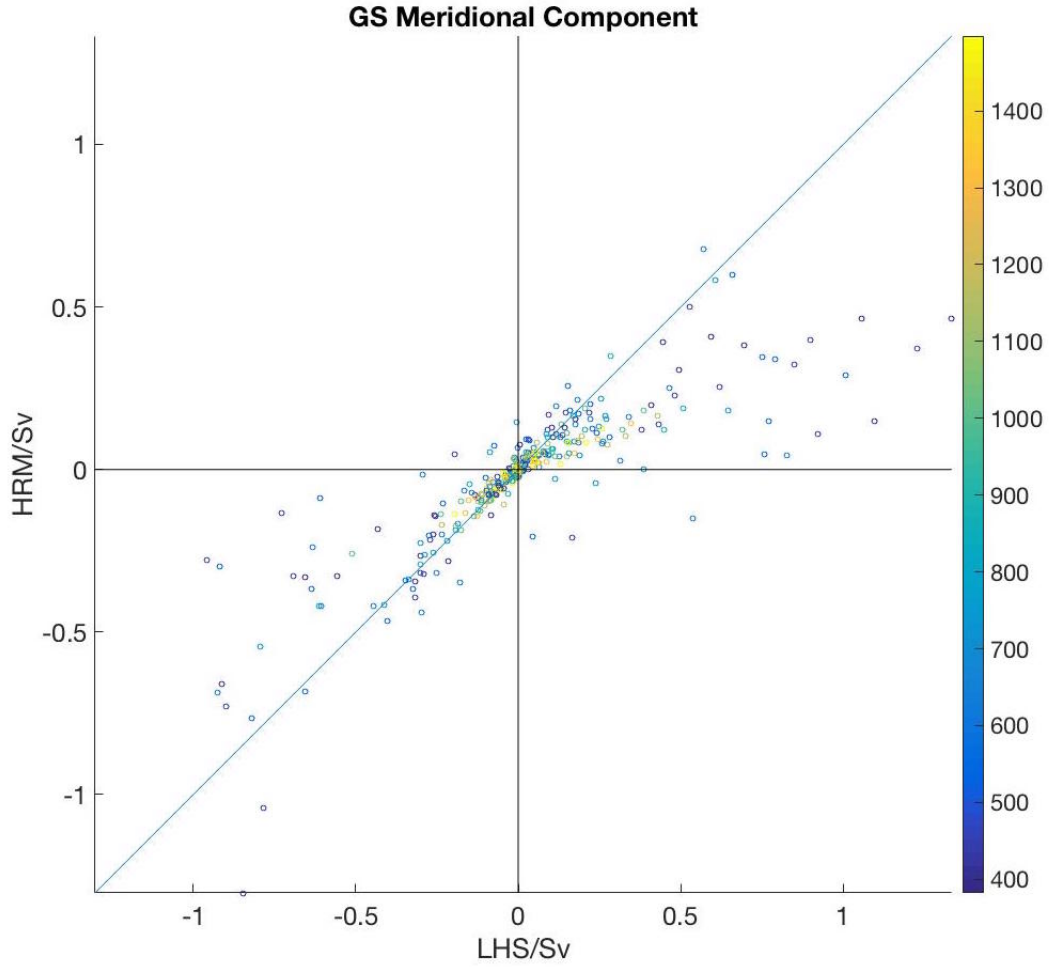


Figure 3.5: Scatter plot of transports calculated by the two methods at different latitudes from about $32^{\circ}N$ to $39^{\circ}N$ and different depths from about 382m to 1320m, in the Gulf Stream. On the x -axis is the high-resolution estimate of the streamfunction (the left-hand side of equation 3.13) and on the y -axis is the low-resolution estimate (the right-hand side of equation 3.13). The colorbar indicates the depth of the calculated transport in meters.

using the fine-resolution data, as can be seen in Fig. 3.10. These favourable results are confirmed in the scatter plots of Fig. 3.11 (a) and (b) which show results from all longitudes in the range of latitudes of the ACC.

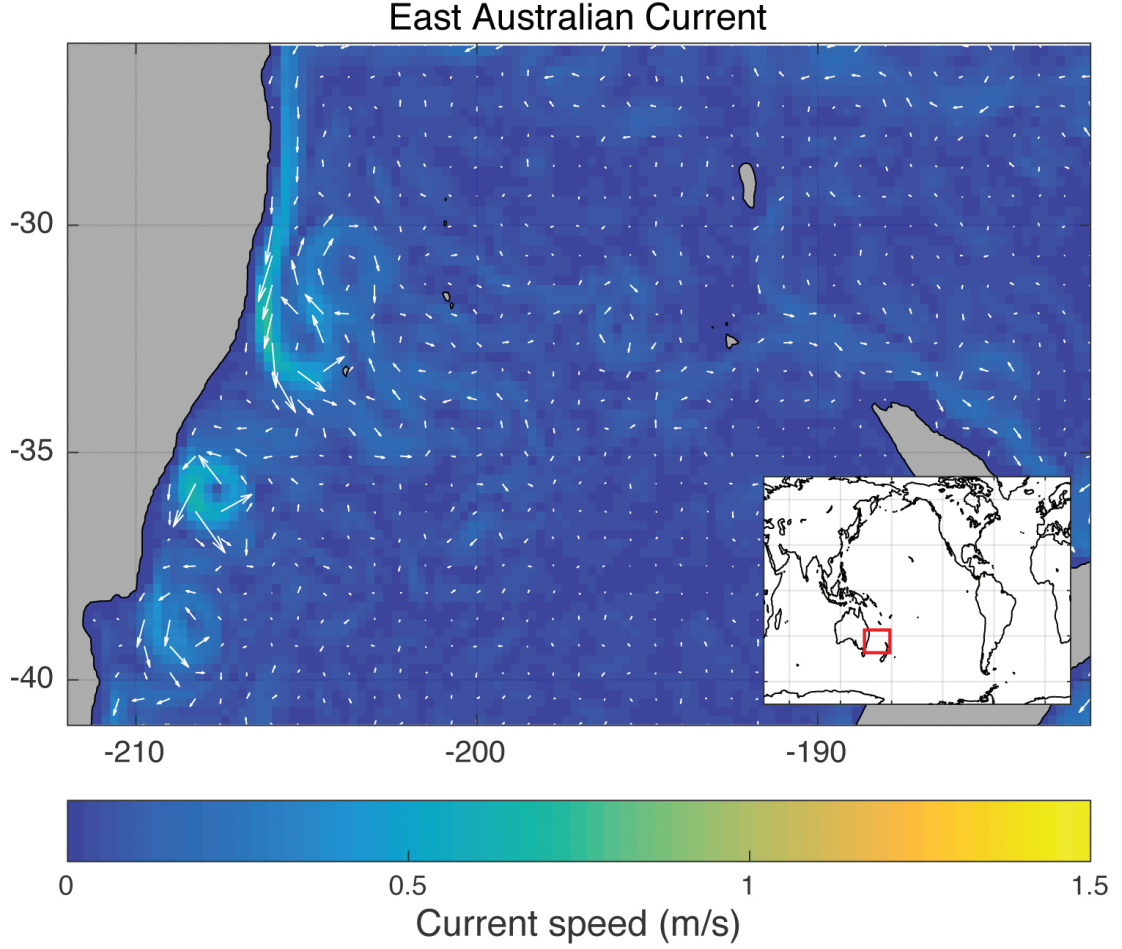


Figure 3.6: Fine-resolution current speeds of the East Australian Current area at a depth of 414 m are shaded. Velocity arrows are overlain every three grid points.

3.3.4 The dominance of the horizontal shear term compared with the vertical shear term

The first term on the right-hand side of equation 3.13 gives the transport induced by the correlation between the zonal variations of velocity and density. In all regions examined we find this first term to be significantly larger than the remaining terms of the equation, which involve the vertical shear of the horizontal velocity. This is illustrated in Fig. 3.12 and Fig. 3.13, which shows that the horizontal shear term dominates both the meridional and zonal components. Nonetheless, this dominance is less strong in the Gulf Stream region than in the East Australian Current or Antarctic

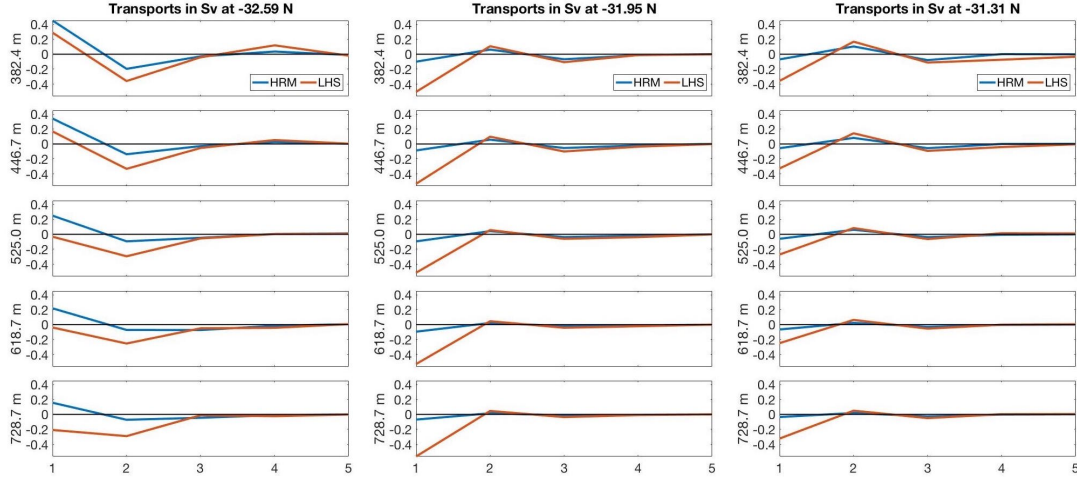


Figure 3.7: Comparison of transport calculated by two methods at three different latitudes and five different depths in the East Australia Current. Red curves correspond to the two-triangle method of Appendix F which uses the high-resolution data, while the blue curves correspond to the right-hand side of equation 3.13 applied to the coarse-resolution fields. The x -axis is the number of coarse-resolution grid boxes from the coast.

Circumpolar Current regions.

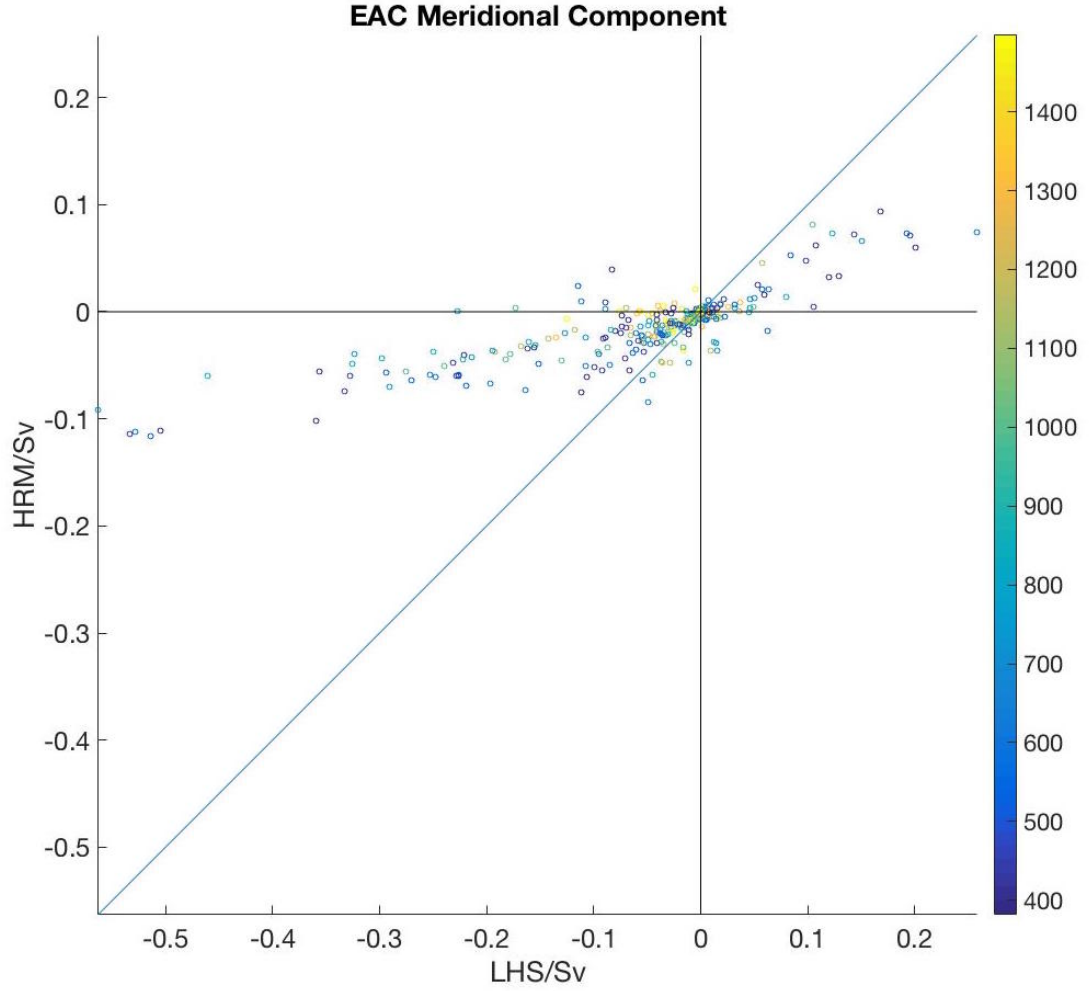


Figure 3.8: Scatter plot of transports calculated by the two methods at different latitudes from about $22^{\circ}S$ to $30^{\circ}S$ and different depths from about 382m to 1320m, in the East Australian Current. On the x -axis is the high-resolution estimate of the stream-function (the left-hand side of equation 3.13) and on the y -axis is the low-resolution estimate (the right-hand side of equation 3.13). The colorbar indicates the depth of the calculated transport in meters.

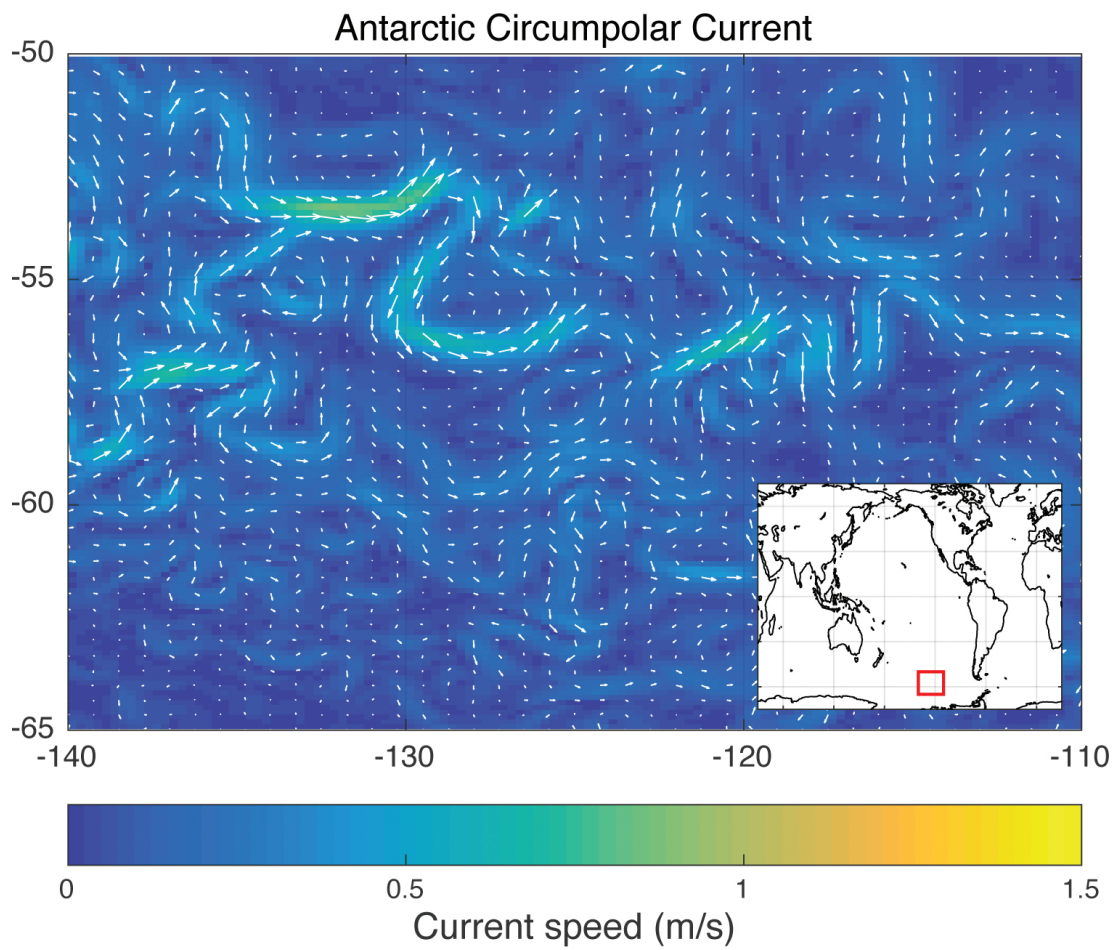


Figure 3.9: Fine-resolution current speeds in a region of the Antarctic Circumpolar Current at 414 m depth are shaded. Velocity arrows are overlain every three grid points.

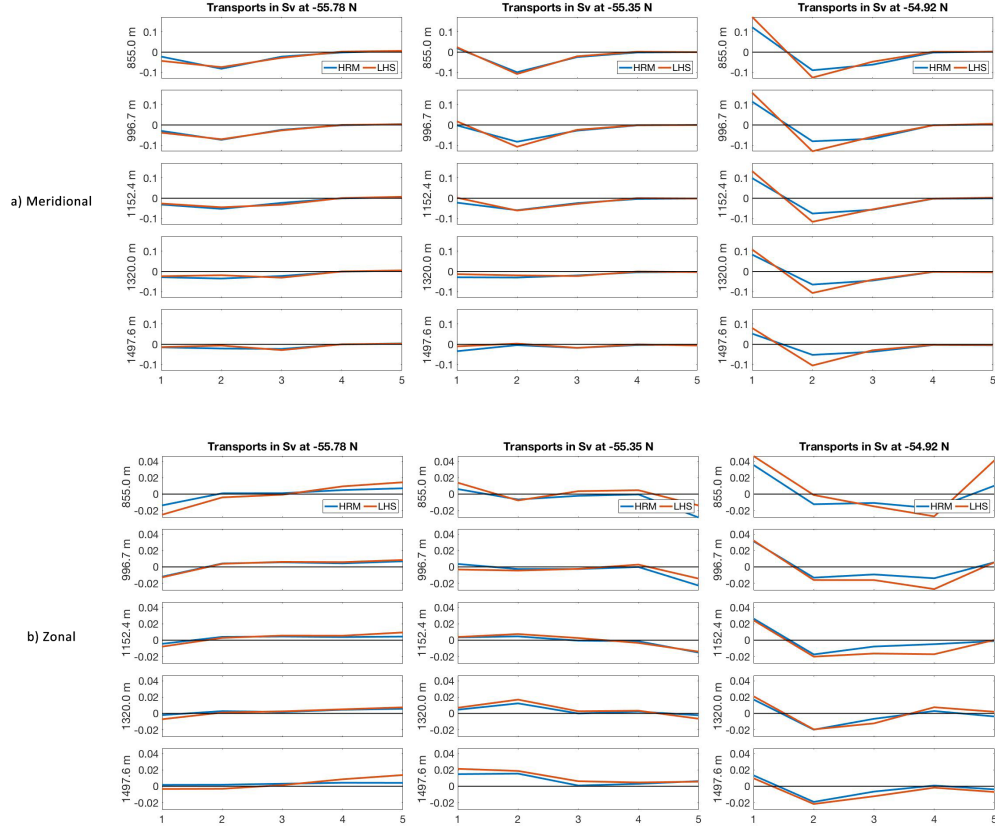
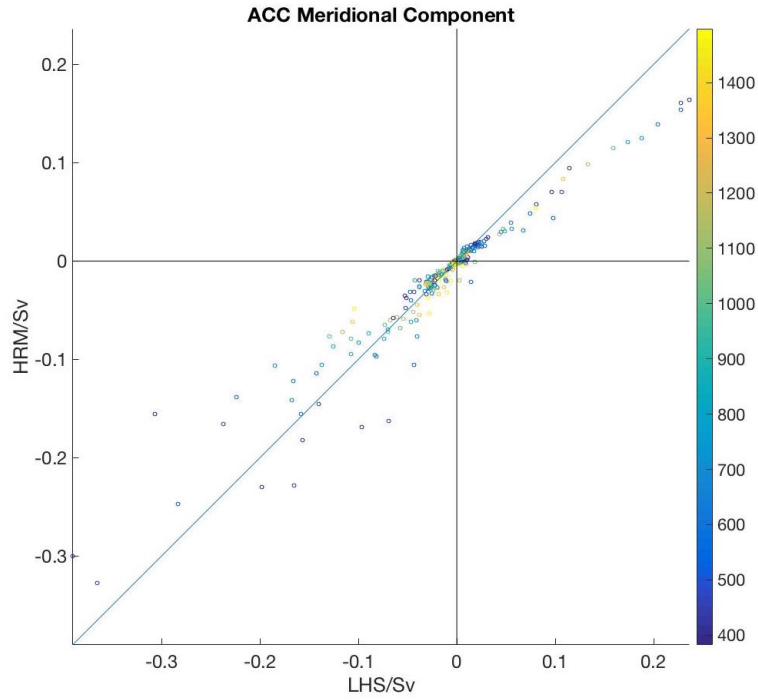
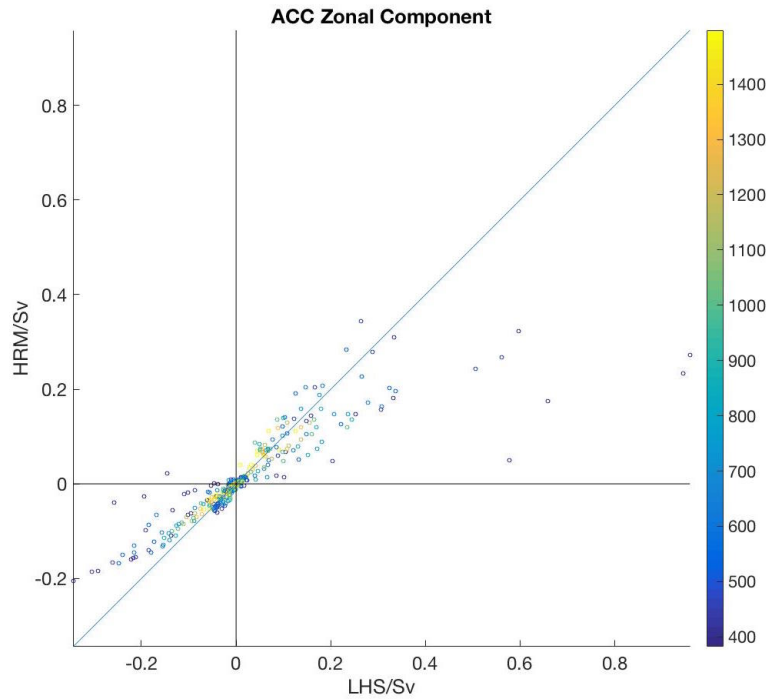


Figure 3.10: Comparison of the transport estimates in the (a) meridional and (b) zonal directions, calculated by two methods at three different latitudes and five different depths in the Antarctic Circumpolar Current. Red curves correspond to the high-resolution estimate of the transport, while blue curves correspond the low-resolution estimate. The x -axis is number of coarse-resolution grid boxes, taken as 1 to 5 starting from the coastline for all locations.



(a)



(b)

Figure 3.11: Scatter plot of transports calculated by the two methods in the (a) meridional and (b) zonal directions at different latitudes from about $58^{\circ}S$ to $60^{\circ}S$ and different depths from about 382m to 1320m, in the Antarctic Circumpolar Current. The x -axis is the high-resolution estimate of the streamfunction and the y -axis is the low-resolution estimate, The colorbar indicates the depth of the calculation in meters.

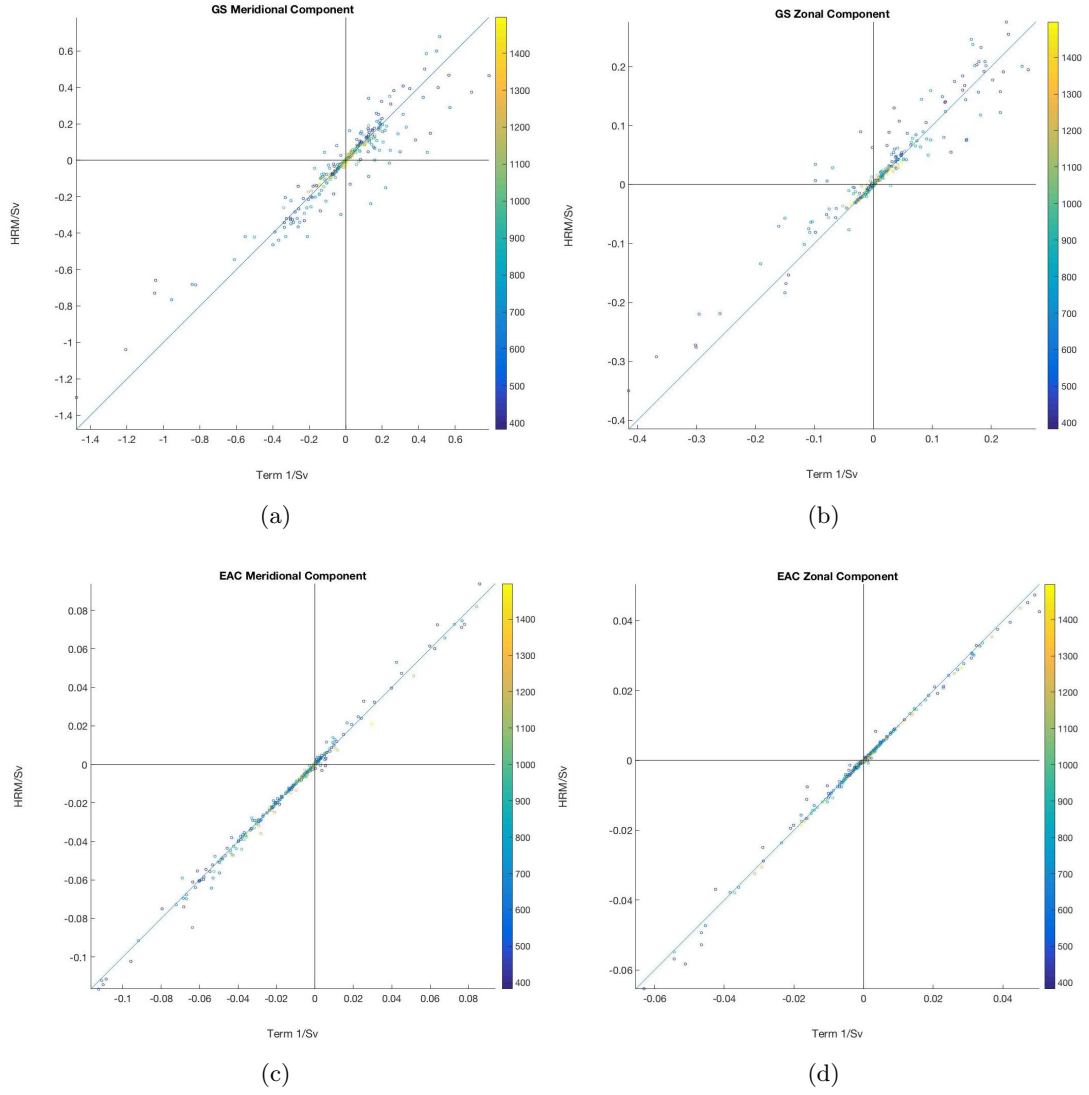


Figure 3.12: The first term (the horizontal shear term) of the right-hand sides of equations 3.13 (meridional) and 3.14 (zonal) is plotted on the x -axis, with the full right-hand sides of these equations plotted on the y -axis of these figures.

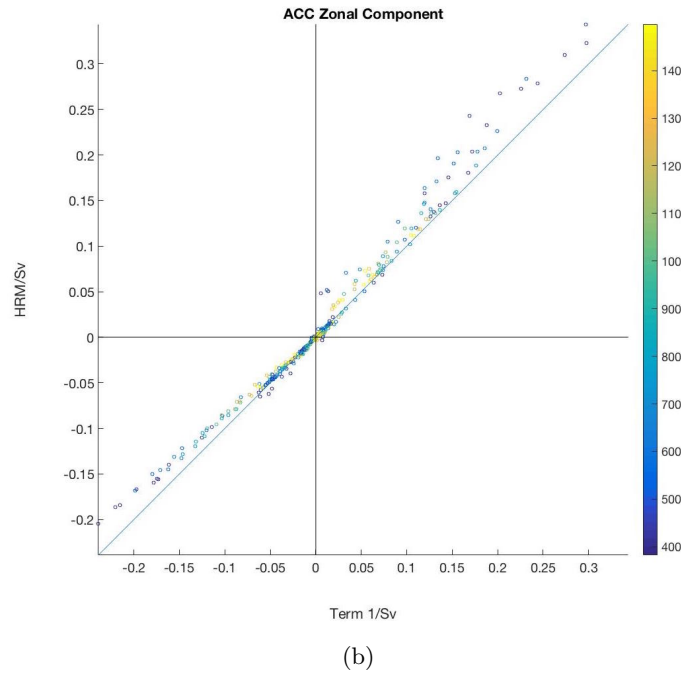
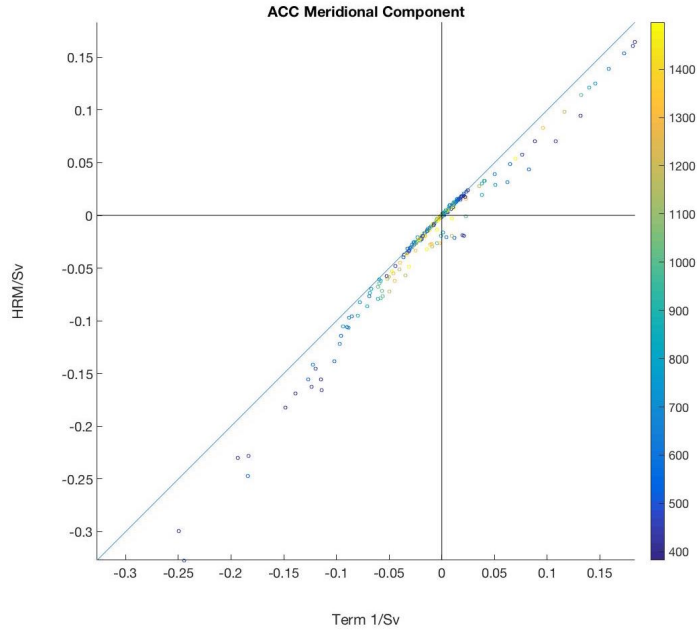


Figure 3.13: The first term (the horizontal shear term) of the right-hand sides of equations 3.13 (meridional) and 3.14 (zonal) is plotted on the x -axis, with the full right-hand sides of these equations plotted on the y -axis of these figures.

3.4 The HRM contribution to meridional overturning

The contribution of the quasi-Stokes velocity of the HRM to the meridional overturning circulation is estimated by calculating the zonally-integrated meridional streamfunction Ψ_{HRM}^y given by equation 3.16, using the same output. The extra meridional overturning of the HRM is dominated by a cell in the ACC region of strength 1.5 Sv. This overturning cell has the same sign and a similar structure to that induced by the advection of the TRM [e.g., calculated with the Gent et al. (1995) scheme]: it advects surface waters southward and deeper water northward, opposing the Ekman-induced overturning. Nevertheless, at a strength of 1.5 Sv, the HRM extra overturning is approximately 10% of its TRM counterpart.

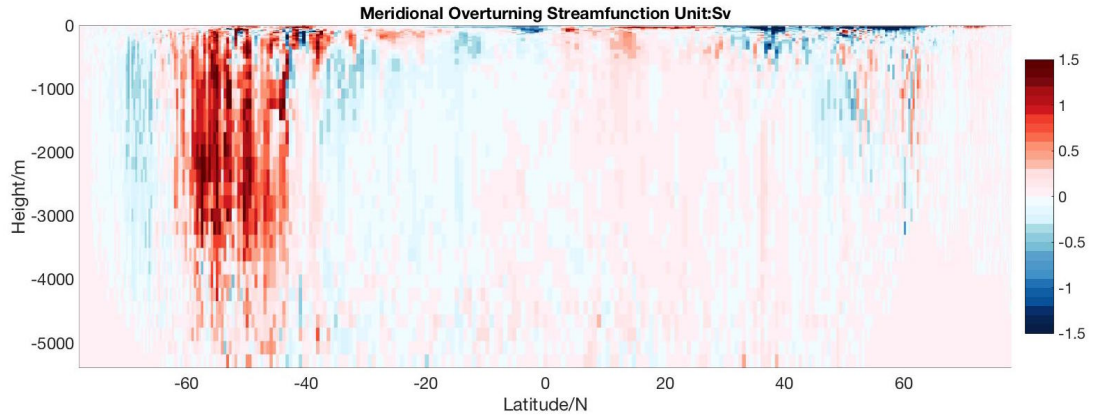


Figure 3.14: The meridional overturning streamfunction of the HRM quasi-Stokes velocity in z -coordinates.

3.5 The HRM contribution to the horizontal heat transport

Rintoul and Wunsch (1991) compared the heat transport of different ocean models and concluded that spatial smoothing is primarily responsible for the differences they calculated in the heat fluxes. The present scheme aims to incorporate the spatial correlations between velocity and scalar quantities that are missing in ocean models, due to the limited spatial resolution and the box-car averaged nature of the velocity and the scalar field. In this way, it is expected that implementing the scheme into a coarse-resolution ocean model will improve its representation of lateral heat fluxes. In this section, the meridional heat fluxes induced by the extra HRM advection are calculated and analyzed. The depth-integrated heat fluxes are calculated across the northern and eastern faces of every coarse-resolution grid column. Where the face of an individual box is land, the streamfunction there is put equal to zero before performing the vertical integration.

As in McDougall and McIntosh (2001), the contribution of the extra streamfunction to the horizontal heat flux is

$$\begin{aligned}
 \rho_0 c_p^0 \int_{-H}^0 \frac{d\Psi_{HRM}}{dz} \Theta dz &= \rho_0 c_p^0 \int_{bottom}^{top} \Theta d\Psi_{HRM} \\
 &= \rho_0 c_p^0 \sum_{i=1}^N \Theta_i (\Psi_{HRM,i} - \Psi_{HRM,i+1}),
 \end{aligned} \tag{3.19}$$

where Θ stands for Conservative Temperature, ρ_0 is taken to be $1030 kg \cdot m^{-3}$ and the constant value of the specific heat at constant pressure, c_p^0 , is the TEOS-10 value given by the GSW code [McDougall and Barker (2011)]. The last step of equation 3.19 is the finite amplitude approximation to the integrals on the first line. The index i in this equation goes from 1 at the sea surface to N at the sea floor. The streamfunction is first interpolated onto the interface heights (the heights of the top and bottom of the model boxes) before being used in this equation. The shallowest box has index $i = 1$ with Conservative Temperature at mid height of Θ_i and the interpolated HRM streamfunction of $\Psi_{HRM,1}$ is forced to be zero at the sea surface, and is $\Psi_{HRM,2}$ at the bottom of this box. The HRM streamfunction at the sea floor, $\Psi_{HRM,N+1}$, is also forced

to be zero. This ensures that the vertically-integrated mass flux is zero within each water column, so that the depth-integrated extra heat flux given by 3.19 is independent of whether the temperature is measured in Kelvin or Celsius.

The depth-integrated heat flux, $\rho_0 c_p^0 \sum_{i=1}^N \Theta_i (\Psi_{HRM,i} - \Psi_{HRM,i+1})$, is shown in Fig. 3.15 for the Gulf Stream region. The underlying color map indicates the magnitude of the total depth-integrated heat flux in each grid box. The direction of the depth-integrated heat flux is given by the white arrow in each grid box. The large values are found mainly along the coastal line, which is expected because the extra HRM streamfunction are more significant at the boundary areas. The streamfunction has the eastward and northward components given by equations 3.13 and 3.14 respectively, so that it includes the widths Δx and Δy of the (x, y) grid and the units displayed are PW. As expected, the additional heat fluxes introduced by the scheme are concentrated along the coast and at eddying locations, where flows are both strong and of relatively small scale. When the values of the meridional component of equation 3.19 are summed across all longitudes we obtain the contribution of the quasi-Stokes velocity field to the oceanic meridional heat transport. This contribution is typically 0.1 PW, and almost 0.2 PW at the latitudes of the ACC in the Southern Ocean (Fig. 3.16). Thus, introducing the HRM extra advection into an ocean model run at 3/4-degree resolution could significantly impact the simulated meridional heat fluxes. The take-home message from Fig. 3.16 is that, when running an ocean model at 3/4-degree resolution, the HRM correlations that are missing due to the coarse nature of the model grid means that the model misses typically 0.1 PW, and misses almost 0.2 PW at the latitudes of the ACC in the Southern Ocean, of meridional heat flux which can readily be added to the model code using our quasi-Stokes HRM streamfunction approach.

This 0.2 PW heat transport is induced by the spatial correlations and it is not under the influence of the time average. The temporal and spatial correlations are calculated simultaneously. Unlike the eddy heat transport in Treguier et al. (2017) which was a time-averaged eddy heat transport, this heat transport will not be compensated by the time-mean flow. When the HRM method is implemented in an ocean model, the HRM transport is calculated at each step rather than being averaged over time as additional

mean transport.

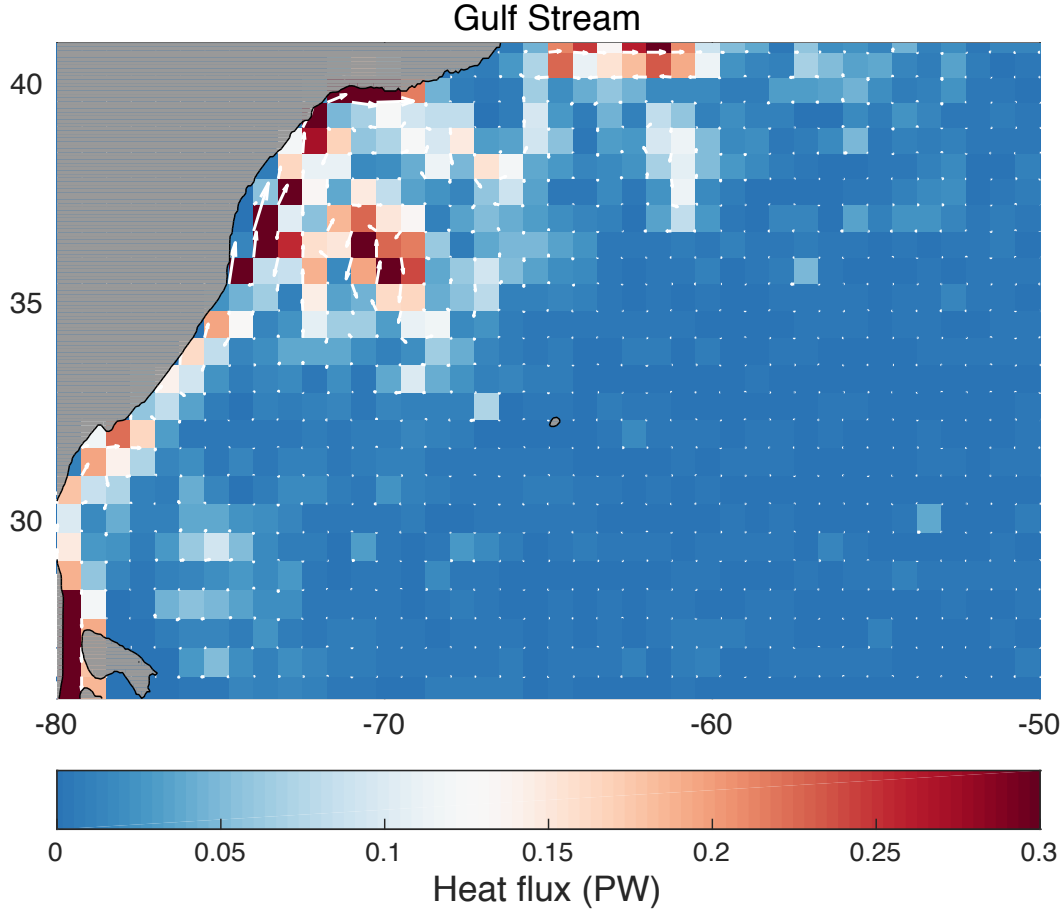


Figure 3.15: The values of $\rho_0 c_p^0 \sum_{i=1}^N \Theta_i |\Psi_{HRM,i} - \Psi_{HRM,i+1}|$ in the region of the Gulf Stream, in units of PW. The underlying color indicates the total amount of depth-integrated heat flux in each grid box, which is the absolute value of magnitude of the heat flux. The white arrows show the directions.

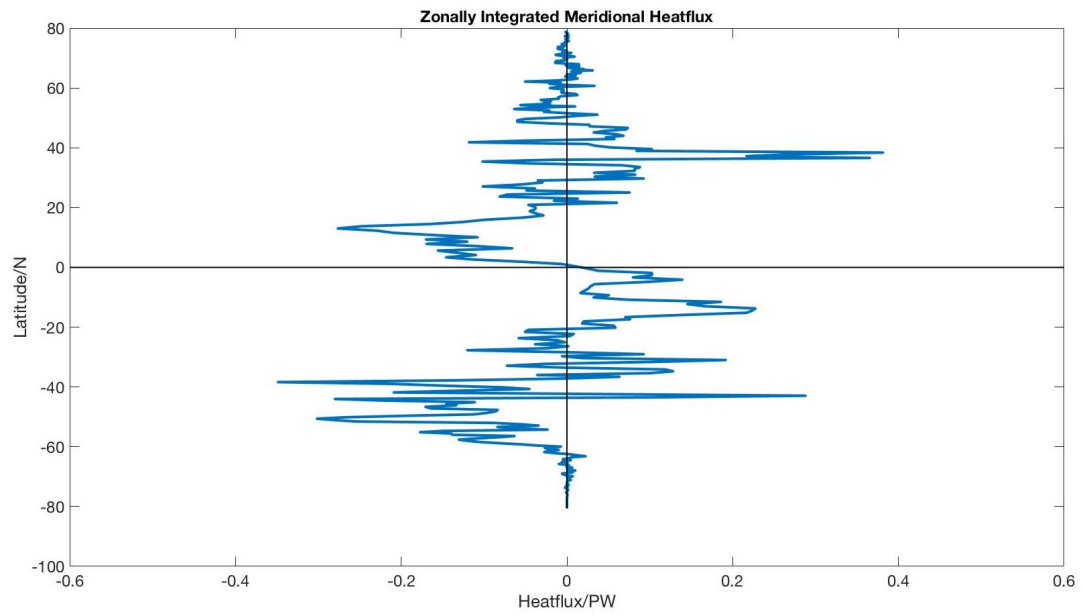


Figure 3.16: The quasi-Stokes HRM zonally- and depth-integrated meridional heat transport.

3.6 Tapering of the quasi-Stokes HRM streamfunction

The HRM method does not apply tapering near the sea surface. At the surface, the intersection of the neutral tangent plane and the adjacent cast may be located above the sea level. However, the effective height difference we used is actually half of that calculated on the adjacent cast (see the red dot in Fig. 3.17), because each calculation of the HRM transport is the transport through half of the face of a grid box (the eastern, western, northern or southern half), shown as one of the shaded areas in Fig. 3.17. Even if the effective height difference, based on an extrapolating a given isopycnal surface, would tend to outcrop as shown in Fig. 3.18, our estimate of the quasi-Stokes HRM streamfunction which clamps the height at the sea surface is an underestimate of the true volume flux. These considerations justify our decision to not taper the HRM streamfunction towards zero except right at the sea surface. This is an important difference compared with the quasi-Stokes TRM streamfunction where the tapering towards zero at the upper and lower boundaries is justified by physical considerations based on the transport of water that is more dense than the density surface whose average height perturbation is zero [see section 9 in McDougall (1998) and section 8 in McDougall and McIntosh (2001)].

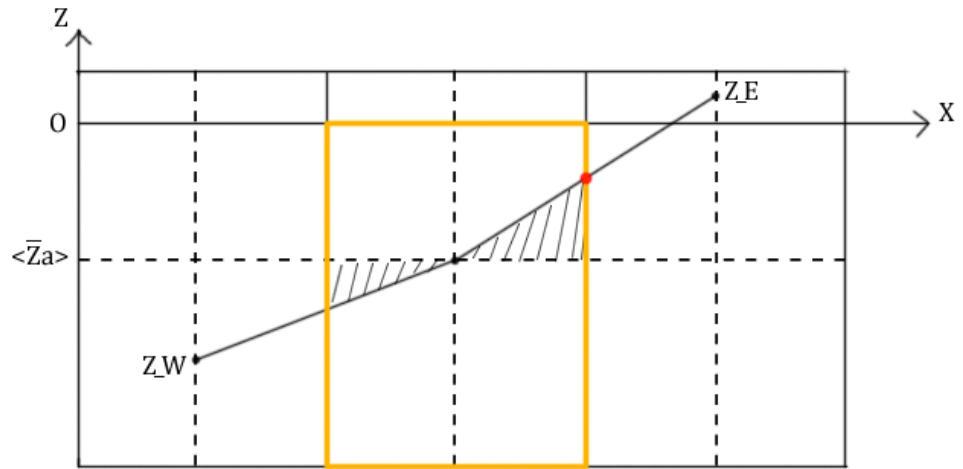


Figure 3.17: An example of outcropping locally-referenced neutral tangent plane in which the effective height (the red dot) is below the sea surface.

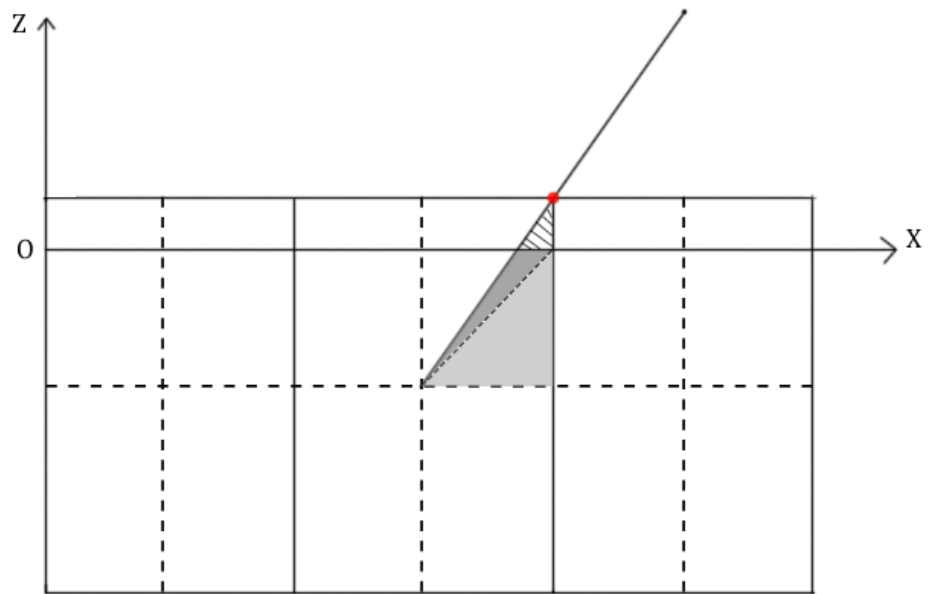


Figure 3.18: An illustration of outcropping case where the effective height (the red dot) is also above sea surface.

3.7 HRM implementation in ocean models

The HRM streamfunction can be implemented in ocean models to incorporate the contribution from spatial correlations into models. It does not need parameterization and can be calculated using data that are already available in the model. In the diagnostics, we used a snapshot dataset with only salinity, potential temperature and velocity field available. However, in a forward model run, the density field is updated in real time. It is more reasonable and easier to use real-time densities to calculate the neutral density slope that is needed for HRM calculation.

In the forward model, the slopes of neutral tangent planes L^x and L^y can be calculated at every time step by using the horizontal and vertical gradients of the locally-referenced potential density,

$$L^x = -\frac{\gamma_x}{\gamma_z}, \quad (3.20)$$

$$L^y = -\frac{\gamma_y}{\gamma_z}. \quad (3.21)$$

Therefore, the quasi-Stokes HRM transport in the meridional direction can be computed by substituting equation 3.20 into equation 3.10 (repeated here as equation 3.22). Similarly, the zonal component of the quasi-Stokes HRM transport can be computed by equation 3.23, with substitution of equation 3.21, as

$$\begin{aligned} \int_{-\Delta x/2}^{\Delta x/2} \int_{\langle \bar{z}_a \rangle}^{\bar{z}_a(x)} (\bar{v} - \bar{v}_0) dz dx &= \frac{1}{24} \langle \bar{v} \rangle_x L_E^x [\Delta x]^3 + \frac{1}{24} \langle \bar{v} \rangle_x L_W^x [\Delta x]^3 \\ &+ \frac{1}{48} \langle \bar{v} \rangle_z (L_E^x)^2 [\Delta x]^3 + \frac{1}{48} \langle \bar{v} \rangle_z (L_W^x)^2 [\Delta x]^3 \\ &+ \frac{1}{2} \langle \bar{v} \rangle_z (\delta z)^2 \Delta x + O([\Delta x]^4), \end{aligned} \quad (3.22)$$

$$\begin{aligned} \int_{-\Delta y/2}^{\Delta y/2} \int_{\langle \bar{z}_a \rangle}^{\bar{z}_a(y)} (\bar{u} - \bar{u}_0) dz dy &= \frac{1}{24} \langle \bar{u} \rangle_y L_N^y [\Delta y]^3 + \frac{1}{24} \langle \bar{u} \rangle_y L_S^y [\Delta y]^3 \\ &+ \frac{1}{48} \langle \bar{u} \rangle_z (L_N^y)^2 [\Delta y]^3 + \frac{1}{48} \langle \bar{u} \rangle_z (L_S^y)^2 [\Delta y]^3 \\ &+ \frac{1}{2} \langle \bar{u} \rangle_z (\delta z)^2 \Delta y + O([\Delta y]^4), \end{aligned} \quad (3.23)$$

where $\delta z = \frac{1}{8}(L_E^x - L_W^x)\Delta x$ for equation 3.22 and $\delta z = \frac{1}{8}(L_N^y - L_S^y)\Delta y$ for equation 3.23.

Encouragingly, the HRM transport does not significantly change in magnitude when the neutral density slope is calculated by taking the ratio of the density gradients. To demonstrate this fact, we generated a density field of 3/4 degree resolution from the known salinity, conservative temperature and pressure, since the snapshot we used for diagnostics has no information about in situ density. The GSW code of McDougall and Barker (2011) was used to obtain the spatial gradients of locally-referenced potential density γ_x , γ_y and γ_z and hence calculate the slopes in equations 3.22 and 3.23. The vertical density gradient γ_z at the face indexed (i, j, k) is given by the difference between upper and lower potential densities whose reference pressure is at k , as

$$\begin{aligned} \gamma_z(i, j, k) = & \rho_\theta \left(sa(i, j, k-1), ct(i, j, k-1), pr(i, j, k) \right) \\ & - \rho_\theta \left(sa(i, j, k+1), ct(i, j, k+1), pr(i, j, k) \right), \end{aligned} \quad (3.24)$$

where potential density ρ_θ is determined by Absolute Salinity sa , Conservative Temperature ct and pressure reference pr .

We compared both meridional and zonal HRM transport in three areas to show that the HRM transport is not sensitive to the method of obtaining neutral density slopes. The two ways of calculating HRM transport have been compared in three areas: Gulf Stream, East Australian Current and Antarctic Circumpolar Current. At most of the grid points, the two methods give same HRM transports (see Fig. 3.19 and Fig. 3.20), except for a few points of zonal HRM transports in Gulf Stream and East Australian Current. In the Antarctic Circumpolar Current, the two methods are very close to the one-to-one line.

This section is simply a preliminary attempt to implement the HRM method into ocean models. It has been shown that the HRM calculation is robust and easy to be adapted to ocean models. An actual implementation needs a full understanding of the target ocean model. Equations 3.22 and 3.23 provide a framework that can be amended to match the models technical features. For example, equations 3.22 and 3.23 can be programmed as a diagnostic module in the Modular Ocean Model (MOM). The MOM provides tracer and velocity fields that are needed for HRM, as well as the real-time density field. Also, the MOM has intrinsic function to calculate potential density for γ_z in equations 3.22 and 3.23. Ultimately, the HRM streamfunction can be added to the total quasi-Stokes streamfunction and calculate simultaneously in the MOM. However,

it will require a full understanding of the fundamentals of MOM and the structure of the numerical codes.

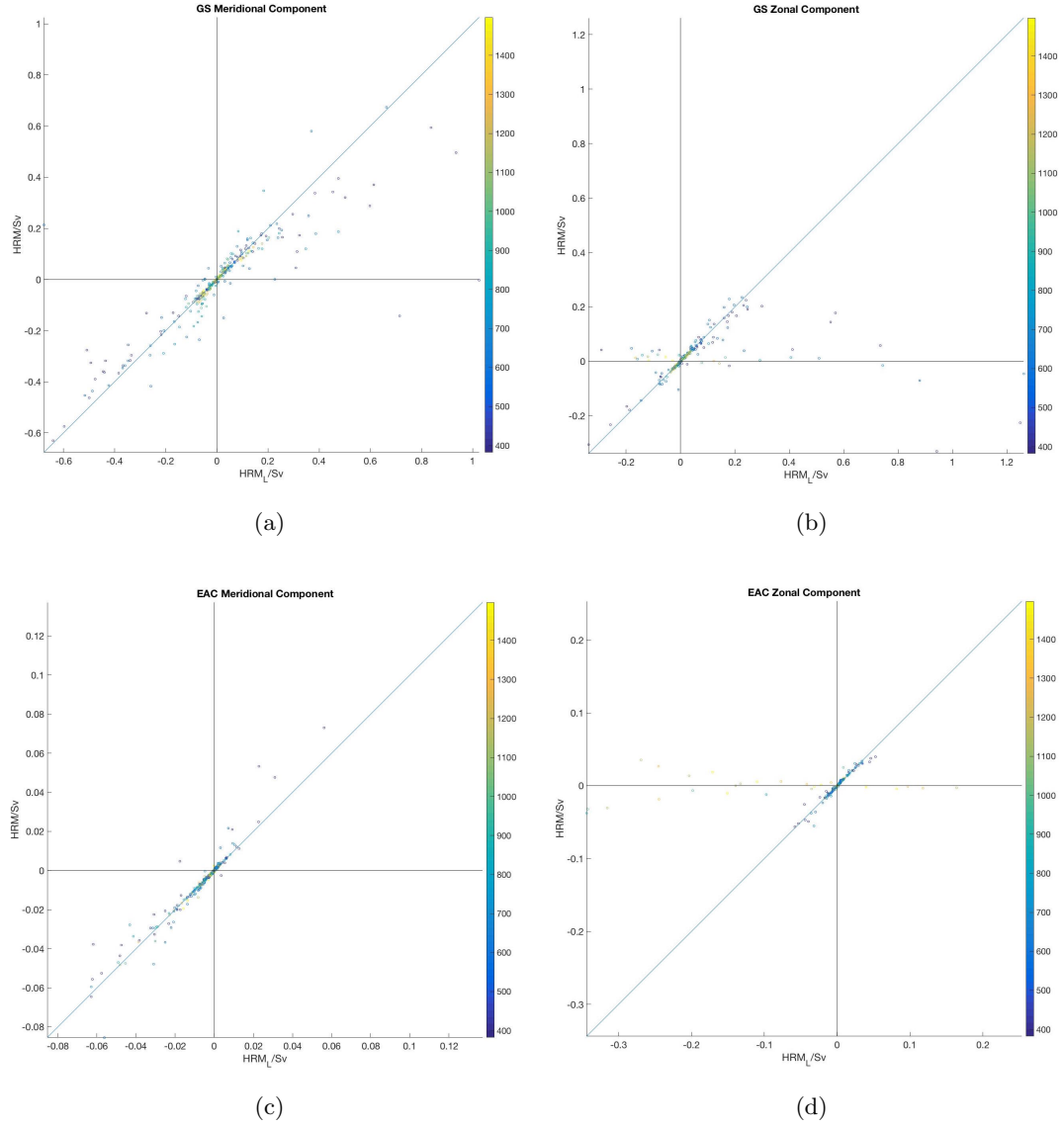
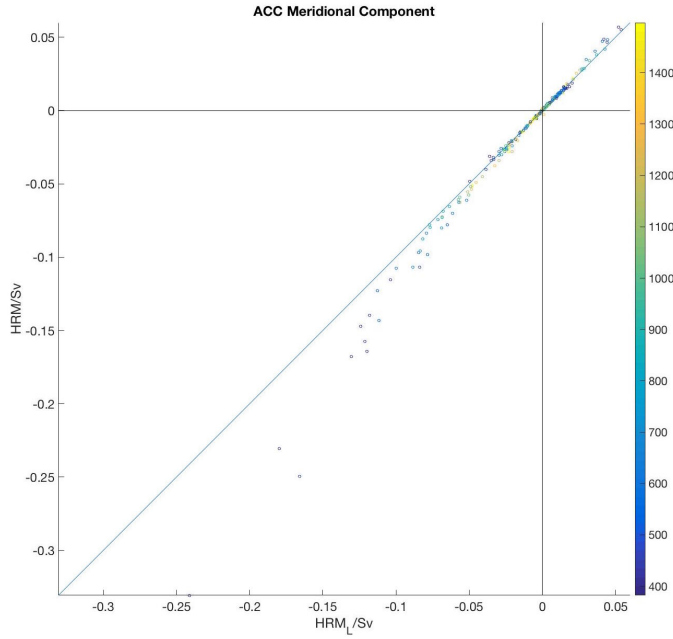
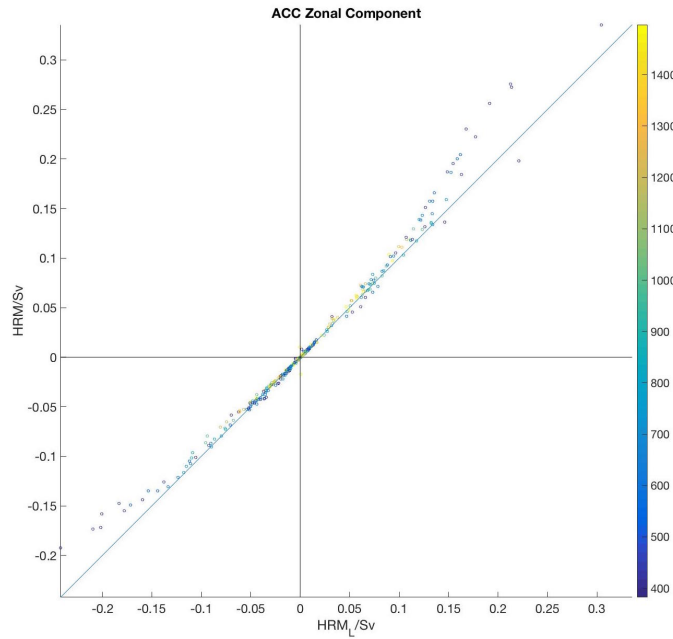


Figure 3.19: Two ways of calculating HRM transport have been compared in the GS and EAC areas. Both meridional and zonal HRM transports in these three areas are compared. The x -axis gives HRM transports calculated by using the ratio of locally-referenced potential density gradients. The y -axis presents the HRM transport calculated by the heights of neutral tangent planes calculated using all the information of vertical casts. The color indicates the depths and colorbar shows the depths in meters.



(a)



(b)

Figure 3.20: Two ways of calculating HRM transport have been compared in the ACC area. Both meridional and zonal HRM transports in these three areas are compared. The x -axis gives HRM transports calculated by using the ratio of locally-referenced potential density gradients. The y -axis presents the HRM transport calculated by the heights of neutral tangent planes calculated using all the information of vertical casts. The color indicates the depths and colorbar shows the depths in meters.

3.8 Conclusions

We have proposed a method of approximating the transport of scalar quantities due to spatial correlations that are unresolved by ocean models. The method introduces an extra non-divergent advection, which is calculated from resolved model fields via a Taylor-series approximation. Analogous to the quasi-Stokes TRM velocity, which accounts for unresolved temporal correlations [Gent et al. (1995), McDougall and McIntosh (2001)], this extra advection, or quasi-Stokes HRM velocity, can be added to the Eulerian-mean velocity of the model. However, in contrast to the quasi-Stokes TRM streamfunction, the proposed quasi-Stokes HRM streamfunction does not need a parameterization. Instead, it is estimated directly from the quantities known to the model which appear on the right-hand sides of equations 3.5 and 3.6. The only assumption made is that the resolved velocity field is sufficiently smooth that the Taylor series approach (equation 3.4) converges and can be approximated by the leading linear terms. This assumption is justified in the theory by the choice of performing the spatial averaging after the temporal averaging, and in practice by the recognition that the effective resolution of an ocean model (run with appropriate viscosity) is several grid boxes.

The proposed method has been tested diagnostically using instantaneous output from a 1/4-degree model simulation, boxcar averaged to 3/4-degree resolution. We compared the transport of water of a certain density class within the 1/4-degree dataset to the corresponding HRM extra transport calculated at 3/4-degree resolution. We found that the method gives a reasonable approximation of the fine-resolution transports in the Gulf Stream, East Australian Current and Antarctic Circumpolar Currents regions, but tends to underestimate the true transport by several tens of percent in the first two of these regions. These results suggest that the scheme could assist in mitigating the limitations of coarse-resolution models in the representation of tracer fluxes such as the meridional heat transport.

In the 3/4-degree resolution dataset, the contribution of the quasi-Stokes HRM streamfunction to the meridional overturning circulation peaks near 1.5 Sv in the Southern Ocean, representing about 10% of the corresponding circulation due to unresolved temporal correlations as parameterized using the Gent et al. (1995) method. On the other hand, the contribution to the poleward heat flux in the Southern Hemisphere of

the same dataset reaches 0.18 PW, which is approximately half as large as the corresponding flux due to the quasi-Stokes streamfunction of the TRM method [see Fig.8 of Gent et al. (1995)]. The larger impact on the meridional heat fluxes relative to the overturning mass transports possibly relates to the fact that no near-surface tapering has been imposed on the extra HRM streamfunction, in contrast to standard practice for the TRM quasi-Stokes streamfunction. In our discussion of the outcropping of isopycnals at the sea surface, we found no physical reason to taper the quasi-Stokes HRM streamfunction. Indeed, we argued that the outcropping of isopycnals leads to an underestimate of the quasi-Stokes HRM streamfunction.

It may come as a surprise that the zonal integral of the northward quasi-Stokes HRM streamfunction is quite smooth and predominantly of one sign in the ACC region, and that it exhibits a similar structure to the meridional overturning circulation associated with the Gent and McWilliams (1990) parameterization. This similarity may even seem paradoxical when considering that the quasi-Stokes TRM streamfunction, $(\Psi_{TRM}^x, \Psi_{TRM}^y) = (-\kappa L^x, -\kappa L^y)$, points in the direction of minus the slope of density surfaces, whereas the quasi-Stokes HRM streamfunction is often perpendicular to this direction. However, both the TRM and the HRM quasi-Stokes advection aim to compensate for missing correlations, which, in the context of a modelled $O(1^\circ)$ -resolution ACC, arise primarily from the unresolved mesoscale eddies. Both the TRM and the HRM extra streamfunctions thus contribute to mimicking the effect of Southern Ocean mesoscale eddies, which is to oppose the Ekman-forced overturning.

We proposed a method addressing the limited spatial resolution, yet now we ask the question about to what extent the HRM method is affected by the resolution itself. According to equations 3.16 and 3.17, the HRM velocity streamfunctions are proportional to the second powers of resolution scale $(\Delta x)^2, (\Delta y)^2$. If changing the resolution does not change the velocity shears and neutral density slopes, then the quasi-Stokes HRM transport would decrease proportionally to the fineness of the resolution of the model. However, it is likely that as the horizontal resolution is increased, both the velocity shears and the slope of isopycnals will increase, so it is not yet known how the quasi-Stokes HRM streamfunctions might change as the horizontal resolution is increased. The HRM captures the unresolved correlations between velocity and

density, but does not resolve or parametrize the subgrid-scale physical processes. Also, a sufficiently smooth velocity field has been assumed within grid boxes for the Taylor series and this assumption may not be true in strong frontal areas.

An important caveat related to the construction of the coarse-resolution dataset must be acknowledged here. By boxcar averaging an eddy-permitting, $1/4$ -degree model snapshot, we have formed $3/4$ -degree fields that contain some of the signature of the eddies of the original simulation. The HRM extra streamfunction diagnosed here has therefore seen these eddy signatures. In contrast, if the HRM extra streamfunction were calculated during the running of a $3/4$ -degree-resolution model, with the Gent and McWilliams (1990) scheme activated, no eddy footprints would be available to the HRM procedure. This difference could substantially reduce the impact of the HRM extra advection in the ACC. Future work will need to assess the impacts of the quasi-Stokes HRM advection when incorporated online in a prognostic ocean simulation.

It has been demonstrated that the HRM calculation is not sensitive to the way available data from ocean models are used to calculate the slope of neutral tangent planes. This enhances our confidence in the feasibility of implementing the HRM method into ocean models to capture the unresolved spatial correlations. Equations 3.22 and 3.23 in section 3.7 in this chapter sets up the framework of HRM implementation into ocean models where the density field can be updated in real time. The actual implementation will need to take the model's features into consideration.

Chapter 4

Conclusions

Two aspects of small scale thermohaline structures are explored in this thesis. Double diffusive interleaving has been studied in chapter 2 as it is an important small scale thermohaline structure in the ocean. Chapter 2 focused on the properties of steady-state solutions of double diffusive interleaving. Chapter 3 aimed at evaluating and incorporating the unresolved spatial correlations at the scale of the model resolution. These small scale spatial correlations are unresolved in numerical ocean models, but have important influences on the heat and salt transport in the ocean.

In chapter 2, we first built up a model which made a transition from the initial exponentially growing stage to the steady state, based on the momentum equation (equations 2.19 - 2.22), under the assumption that the rate of change of the horizontal velocity perturbation needs to be zero at the steady state. In contrast to previous studies in which double-diffusive fluxes are given by general power laws of the stability ratio, we represented the heat and salt fluxes across interfaces according to laboratory-based flux laws of heat by Huppert (1971) and of salt from McDougall and Taylor (1984). The transition evolved through three regimes (Finger-Finger, Finger-Nondouble-diffusive, Finger-Diffusive) and enabled us to examine the conditions necessary to achieve steady-state double-diffusively driven intrusions. It was found that the strength of the fluxes across the “diffusive” interfaces need to be increased by at least an order of magnitude above the laboratory-determined values, relative to the laboratory-based “finger” fluxes, in order for a steady state to be attained.

In the steady state, the ratio of the vertical flux of Absolute Salinity or Conservative

Temperature across the diffusive interface to that across the finger interface is a function of the exaggeration factor and the environmental stability ratio. The value of those two ratios showed a strong dependence on the environmental stability ratio rather than the exaggeration factor, especially when the exaggeration factor is greater than 15. These two ratios also change with different Prandtl number but the dependency is not significant. The ratio of Conservative Temperature across the diffusive interface to that across the finger interface is close to 1 in all cases of different Prandtl numbers, while the ratio of Absolute Salinity across the diffusive interface to that across the finger interface is much smaller. That means that the amounts of flux of salt across two types of interfaces are very different, whereas the vertical fluxes of heat across two types of interfaces are of similar magnitude.

The proportionality constant between the salt flux across a finger interface and the salinity contrast across the interface increased after reaching the steady state. This was caused by allowing the laboratory-based flux laws to take over instead of linearly growing. The flux of salt across a finger interface is thus enhanced relative to the salinity contrast. The larger the environmental stability ratio, the larger the increase in this proportionally constant is, relative to the value at the initial state.

An important aspect of this study is that we took the advection of the perturbations in the steady state as well as the interfacial double-diffusive fluxes themselves into account when quantifying the total diapycnal fluxes of heat and salt. This advection of the perturbations consists of two sources, one from the correlations of vertical velocity and heat or salt at a given point, and the other from the correlations induced by the spatial average in the horizontal direction. As a result, we realized that it is mainly the spatial correlations of the diapycnal velocity of the intrusions with the temperature and salinity perturbations that is responsible for the upgradient fluxes of heat and salt (see the large -0.61 numbers in equations 2.57 and 2.58). The dominant contributions to the total diapycnal fluxes of heat and salt from the advection of heat and salt were not recognized by previous studies. One would get a greater (0.47 rather than -0.29) downgradient diapycnal flux of salt and a much smaller (0.04 instead of -0.75) downgradient diapycnal flux of heat, if the dominant advective correlations are ignored. We have also shown that the total diapycnal fluxes of both Absolute Salinity and

Conservative Temperature are upgradient, that is, both are in the sense of a negative vertical diffusion coefficient.

The magnitude and signs of the total diapycnal fluxes of heat and salt will certainly have implications for parameterizing the double diffusive interleaving motions in intermediate-scale and large-scale numerical ocean models. The vertical diffusivity of temperature and salinity may need to be set at different magnitudes, with the magnitude of negative vertical diffusivity for temperature being larger than that for salinity. When Prandtl number is greater than or equal to 1, and the exaggeration factor less than 20, the ratio of the total diapycnal fluxes of heat and salt is close to 1. In this case, the negative vertical diffusivity for temperature should be larger but still close to that for salinity. Therefore a larger turbulent diapycnal mixing is required to counteract the double-diffusive interleaving motion because the negative diffusions of heat and salt have nearly equal diffusion coefficients.

It is very difficult to compare an interleaving model to observation data because the observational data of interleaving are limited, especially the work in this thesis is three dimensional and the interleaving observations are mainly two dimensional. Researches in interleaving modelling commonly do not compare models with observations.

Numerical ocean models have limited ability to resolve the temporal and spatial correlations of subgrid-scale processes. Just as the TRM theory accounted for the unresolved temporal correlations between temperature and horizontal velocity, the HRM theory incorporates the unresolved spatial correlations that are missing from ocean models. In chapter 3, we applied a Taylor-series expansion to the resolved velocity field and calculated the transport of scalar quantities due to the unresolved spatial correlations. The Taylor-series approach introduces an extra non-divergent advection named the quasi-Stokes HRM streamfunction which can be added to the total quasi-Stokes streamfunction. This extra non-divergent advection consists mainly of the correlation between the horizontal and vertical velocity shear and the slope of neutral tangent plane. The proposed quasi-Stokes HRM streamfunction does not need a parameterization. Instead, it is estimated directly from the quantities known to the model such as velocities, tracers and densities. The instantaneous output from a 1/4-degree MOM simulation has been used to do diagnostic tests for the HRM method. The dataset has

been boxcar averaged to construct a 3/4-degree coarse resolution dataset in order to show that the HRM method gives reasonable approximations of HRM transport of water mass and scalar properties that could be resolved by a fine-resolution (1/4-degree) ocean model. Three areas of interest are selected for comparing the transport of water of a certain density class calculated by the original 1/4-degree dataset to the corresponding HRM extra transport calculated at 3/4-degree coarse resolution. The Gulf Stream and East Australian Current areas are famous western boundary areas and the Antarctic Circumpolar Currents regions are of great interest to oceanographers. The coarse-resolution-based calculation gives a good approximation of the fine-resolution transports in these three areas, but tends to underestimate the true transport by several tens of percent in the first two of these regions. Another finding is that the HRM streamfunction is dominated by the spatial correlation between the horizontal velocity shear (as opposed to the vertical shear of the horizontal velocity) and the slope of the locally-referenced neutral tangent plane. This strong dominance has been found in all of the three previously mentioned areas.

The HRM method has shown significant influence on the ocean circulation. A contribution with a peak of 1.5 Sv to the meridional overturning circulation in the Southern Ocean is due to the unresolved spatial correlations represented by quasi-Stokes HRM streamfunction. This value is about 10% of the amount of the meridional overturning circulation due to unresolved temporal correlations induced by the TRM. The zonally-integrated northward quasi-Stokes HRM streamfunction exhibits a similar structure to the meridional overturning circulation associated with the Gent and McWilliams (1990) parameterization, even though the direction of the quasi-Stokes HRM streamfunction is generally perpendicular to the direction of the quasi-Stokes TRM streamfunction.

At the 3/4-degree resolution, the contribution from the quasi-Stokes HRM streamfunction to the poleward heat flux in the Southern Hemisphere of the same dataset peaks at around 0.2 PW. This value is approximately 50% as large as the corresponding flux due to the quasi-Stokes streamfunction of the TRM method. The absence of the near-surface tapering of the HRM streamfunction may be responsible for this large impact on the meridional heat fluxes. We consider the non-tapering option to be justified. Indeed, we found that the HRM method has a tendency to underestimate the

real transport.

The only assumption made in HRM approximation is that the resolved velocity field is sufficiently smooth that the Taylor series approach converges and can be approximated by the leading linear terms. To date, even the linear terms that we use have been neglected, so our HRM work is clearly an improvement compared with present practice. The linear assumption is very common in ocean studies for various ocean properties. The non-linear terms increase the precision at the cost of largely increasing computational complexity. Fig. 3.12 has shown that only the zonal linear terms are dominant.

The diagnostics of the HRM method presented here is only a beginning. The ultimate goal is to implement the HRM method in ocean models. The quasi-Stokes HRM streamfunction that accounts for the unresolved spatial correlations of ocean properties can be added to the Eulerian-mean and TRM streamfunctions in ocean models. We have also calculated the quasi-Stokes HRM transport using only the density field generated by salinity, temperature and pressure fields on the Cartesian model grid. Computing the HRM transport using the slope of the neutral tangent plane calculated in this manner is easier to implement in ocean models, such as MOM. Density is a real-time variable that is updated at each time step in ocean models. Also, the slope of the neutral tangent plane is easy to calculate as long as the in situ density and potential density are accessible. The results calculated in this way turned out to be very close to the transport calculated by the previous method, especially in the ACC area where we have demonstrated the useful implications from the HRM method for ocean models. This comparison implies that the HRM method is a stable approximation that is adaptable to different ocean models. The implementation of the HRM method in ocean models surely requires comprehensive understandings of the features and technical details of the target ocean model. However, the proposed framework and the demonstrated robustness and flexibility of the HRM method open up the possibility for future studies. Once the HRM method can be added to both B-grid and C-grid ocean models that contain the GM scheme. Next step is to implement the HRM method in the newest version of MOM (which is MOM6) and NEMO. The implementations will allow modelers to add partial or enhanced HRM to the existing

scheme. Further studies on the impact of the HRM method on the ocean properties can be investigated using customized numerical experiments.

Appendix A

DDI: The Linearly Unstable Solutions

The Prandtl number σ is the ratio of the flux coefficient of momentum D to that of salt B (see equations 2.9 and 2.10).

The disturbances of equations 2.3 - 2.8 are taken to be proportional to $\exp[\hat{\lambda}t + i(\hat{k}x + \hat{l}y + \hat{m}z)]$ with amplitudes Θ_0 for Conservative Temperature, S_0 for Absolute Salinity, U_0 for cross-front velocity, V_0 for alongfront velocity, W_0 for vertical velocity and P_0 for pressure, so that equations 2.3 - 2.8 become

$$(\lambda\hat{U}_0) - fV_0 = -\rho^{-1}\hat{k}P_0 - D\hat{m}U_0, \quad (\text{A.1})$$

$$(\lambda\hat{V}_0) + fU_0 = -\rho^{-1}\hat{l}P_0 - D\hat{m}V_0, \quad (\text{A.2})$$

$$(\lambda\hat{W}_0) = -\rho^{-1}\hat{m}P_0 + g(\alpha\Theta_0 - \beta S_0) - D\hat{m}W_0, \quad (\text{A.3})$$

$$\hat{k}U_0 + \hat{l}V_0 + \hat{m}W_0 = 0, \quad (\text{A.4})$$

$$\hat{\lambda}\beta S_0 + U_0\beta\bar{S}_{Ax} + W_0\beta\bar{S}_{Az} = -B\hat{m}\beta S_0, \quad (\text{A.5})$$

$$\hat{\lambda}\alpha\Theta_0 + U_0\alpha\bar{\Theta}_x + W_0\alpha\bar{\Theta}_z = -\gamma_f B\hat{m}\beta S_0. \quad (\text{A.6})$$

The isopycnal surfaces are initially assumed to be flat and the $x - y$ coordinates are chosen so that $\beta\bar{S}_{Ay} = \alpha\bar{\Theta}_y = 0$. The acceleration terms which are in brackets in equations A.1 - A.3 are neglected for large turbulent Prandtl numbers.

Nondimensional variables are defined by

$$\lambda = \frac{\hat{\lambda}}{N}, m = \frac{B\hat{m}}{N}, \omega = \frac{f}{N}, s = \frac{\hat{k}}{\hat{m}}, r = \frac{\hat{l}}{\hat{m}}, \sigma = \frac{D}{B}, \quad (\text{A.7})$$

$$\epsilon_x = \frac{(1 - \gamma_f)g\beta\bar{S}_{Ax}}{N^2}, \quad \epsilon_z = \frac{(1 - \gamma_f)g\beta\bar{S}_{Az}}{N^2} = \frac{(1 - \gamma_f)}{(R_\rho - 1)}, \quad (\text{A.8})$$

$$R_\rho = \frac{\alpha\bar{\Theta}_z}{\beta\bar{S}_{Az}}, \quad N^2 = g(\alpha\bar{\Theta}_z - \beta\bar{S}_{Az}) = g\beta\bar{S}_{Az}(R_\rho - 1), \quad (\text{A.9})$$

and for finite turbulent Prandtl number, the nondimensional growth rate λ satisfies

$$\begin{aligned} & \lambda^4 + \lambda^3 m(1 + 2\sigma) + \lambda^2[\omega^2 + \sigma m^2(2 + \sigma) + (s^2 + r^2)] \\ & + \lambda[m\omega^2 + \sigma^2 m^3 + (s^2 + r^2)(1 + \epsilon_z + \sigma)m - ms\epsilon_x] \\ & + \sigma m^2(s^2 + r^2)(1 + \epsilon_z) - m\epsilon_x(\sigma ms + \omega r) = 0. \end{aligned} \quad (\text{A.10})$$

The growth rate λ is now maximized with respect to m, r and s . In practice, the vertical wavenumber \hat{m} is much larger than the two horizontal wavenumbers \hat{k} and \hat{l} , and so $(1 + s^2 + r^2) \approx 1$. By differentiating equation A.10 with respect to both r and s and setting them equal to zero, it can be shown that

$$\frac{r}{\omega} = \frac{s}{\lambda + m\sigma}. \quad (\text{A.11})$$

Substituting equation A.11 into A.10 and dividing both sides of A.10 by $(1 + r^2/s^2)$ gives

$$\lambda^3 + \lambda^2 m(1 + \sigma) + \lambda(\sigma m^2 + s^2) + ms^2(1 + \epsilon_z) - ms\epsilon_x = 0, \quad (\text{A.12})$$

which, as noted by McDougall (1985a), is independent of r and so the growth rate λ and the vertical and horizontal wavenumbers are all independent of the Coriolis parameter. Equations 2.12 and 2.13 in the body of this paper are derived from this equation, being the values of m and s that maximize the growth rate λ of the intrusions.

Appendix B

DDI: Initial Conditions

To choose the initial starting point for the model, we take a small value of X and X_0 and use the a relationship between X_0 and Y_0 that applies during the exponentially growing linearly unstable solution, namely, equation (40) of McDougall (1985a) (which is here expressed in terms of $\tilde{s} = s/\epsilon_x$ and $\tilde{m} = \sqrt{\sigma}m/\epsilon_x$),

$$\frac{\left(\frac{\alpha\Theta_0}{\beta S_0} - 1\right)}{1 - \gamma_f} = \tilde{m} \left\{ \sqrt{\sigma}(\tilde{m}^2 - \tilde{s}^2)^{\frac{1}{2}} + \tilde{s}^2 \left[\frac{1}{\sqrt{\sigma}}(\tilde{m}^2 - \tilde{s}^2)^{\frac{1}{2}} + \tilde{m} \right]^{-1} \right\}^{-1}, \quad (\text{B.1})$$

which gives

$$Y_0 = X_0 + X_0(1 - \gamma_f)\tilde{m} \left\{ \sqrt{\sigma}(\tilde{m}^2 - \tilde{s}^2)^{\frac{1}{2}} + \tilde{s}^2 \left[\frac{1}{\sqrt{\sigma}}(\tilde{m}^2 - \tilde{s}^2)^{\frac{1}{2}} + \tilde{m} \right]^{-1} \right\}^{-1}. \quad (\text{B.2})$$

Appendix C

DDI: The Laboratory Flux Laws

A finger interface has warm salty water above cold fresh water, and for this type of double-diffusive interface we use the laboratory results of McDougall and Taylor (1984), where from their Fig. 2 the salt flux across the finger interface can be represented by the function

$$\beta F_f^{S_A} = \frac{0.19}{(R_\rho^f - 0.5)} (g\kappa_T)^{\frac{1}{3}} (\beta \Delta S_A^f)^{\frac{4}{3}} \quad \text{for all} \quad R_\rho^f \equiv \frac{\alpha \Delta \Theta^f}{\beta \Delta S_A^f} > 1. \quad (\text{C.1})$$

As for diffusive interfaces which have cool fresh water above warm salty water, from Fig. 2 of Huppert (1971), we have

$$\gamma_{\text{diff}} \equiv \frac{\beta F_{\text{diff}}^{S_A}}{\alpha F_{\text{diff}}^{\Theta}} = 1.85 - 0.85 R_\rho^{\text{diff}} \quad \text{for} \quad 1 \leq R_\rho^{\text{diff}} \equiv \frac{\beta \Delta S_A^{\text{diff}}}{\alpha \Delta \Theta^{\text{diff}}} \leq 2, \quad (\text{C.2})$$

and

$$\gamma_{\text{diff}} \equiv \frac{\beta F_{\text{diff}}^{S_A}}{\alpha F_{\text{diff}}^{\Theta}} = 0.15 \quad \text{for} \quad R_\rho^{\text{diff}} \equiv \frac{\beta \Delta S_A^{\text{diff}}}{\alpha \Delta \Theta^{\text{diff}}} \geq 2. \quad (\text{C.3})$$

From equations 2.1 - 2.4 and Fig. 1 of Huppert (1971), we find that the flux across a diffusive interface is given by

$$\alpha F_{\text{diff}}^{\Theta} = \frac{3.8}{(R_\rho^{\text{diff}})^2} 0.085 \left(\frac{g\kappa_T^2}{\nu} \right)^{\frac{1}{3}} (\alpha \Delta \Theta^{\text{diff}})^{\frac{4}{3}} \quad \text{for all} \quad R_\rho^{\text{diff}} > 1. \quad (\text{C.4})$$

Appendix D

DDI: The Finger Flux Divergence in the FF Regime

Based on the laboratory-based flux laws, the right-hand side of equation 2.24 is given by

$$\begin{aligned} \frac{2}{\frac{h}{2}\beta\bar{S}_{Az}} \frac{(\beta F_{lower}^{SA} - \beta F_{upper}^{SA})}{\hat{B}} = \\ - \frac{2 \times 0.19(g\kappa_T)^{\frac{1}{3}}(\frac{h}{2}\beta\bar{S}_{Az})^{\frac{1}{3}}}{\hat{B}} \left\{ \frac{(1+X)^{\frac{4}{3}}}{\left[\left(\frac{R_\rho+Y}{1+X}\right) - 0.5\right]} - \frac{(1-X)^{\frac{4}{3}}}{\left[\left(\frac{R_\rho-Y}{1-X}\right) - 0.5\right]} \right\}. \end{aligned} \quad (D.1)$$

As the evolution transitions to finite amplitude at the beginning point, the expression for the FF regime is obtained by the linearly growing analysis of the physical basis of this integration. In the linear growth case, let $\beta F_f^{SA} = \hat{B}\beta\Delta S_A^f$ such that

$$\beta F_{lower}^{SA} - \beta F_{upper}^{SA} = -\hat{B}4\beta S_A', \quad (D.2)$$

and the right-hand side of equation 2.24 and then becomes

$$\frac{2}{\frac{h}{2}\beta\bar{S}_{Az}} \frac{(\beta F_{lower}^{SA} - \beta F_{upper}^{SA})}{\hat{B}} = -4X, \quad (D.3)$$

and correspondingly, equation 2.25 is

$$\frac{2}{\frac{h}{2}\beta\bar{S}_{Az}} \frac{(\alpha F_{lower}^\Theta - \alpha F_{upper}^\Theta)}{\hat{B}} = -4\gamma_f X. \quad (D.4)$$

Now requiring that equations 2.32 and 2.34 be the same at $X = X_0 = 0.1$ implies that \hat{B} is given by

$$\hat{B} = \frac{2 \times 0.19(g\kappa_T)^{\frac{1}{3}}(\frac{\hbar}{2}\beta\bar{S}_{Az})^{\frac{1}{3}}}{4X_0} \left\{ \frac{(1+X_0)^{\frac{4}{3}}}{\left[\left(\frac{R_\rho+Y_0}{1+X_0}\right) - 0.5\right]} - \frac{(1-X_0)^{\frac{4}{3}}}{\left[\left(\frac{R_\rho-Y_0}{1-X_0}\right) - 0.5\right]} \right\}. \quad (\text{D.5})$$

For simplicity, let

$$A(X, Y) = \left\{ \frac{(1+X)^{\frac{4}{3}}}{\left[\left(\frac{R_\rho+Y}{1+X}\right) - 0.5\right]} - \frac{(1-X)^{\frac{4}{3}}}{\left[\left(\frac{R_\rho-Y}{1-X}\right) - 0.5\right]} \right\}, \quad (\text{D.6})$$

so that

$$\hat{B} = \frac{2 \times 0.19(g\kappa_T)^{\frac{1}{3}}(\frac{\hbar}{2}\beta\bar{S}_{Az})^{\frac{1}{3}}}{4X_0} A(X_0, Y_0). \quad (\text{D.7})$$

Appendix E

DDI: The Relationship between the Steady-State Value X^s , Y^s and a^s

The ratio of the salt flux coefficients \hat{B}^s/\hat{B} at steady state to that in the linearly unstable growth phase can also be obtained by using the definition (equation 2.43) of \hat{B}^s together with the finite-amplitude finger flux, equation C.1 in Appendix C, giving (using equation 2.27 at steady state)

$$\frac{\hat{B}^s}{\hat{B}} = \frac{2X_0}{A(X_0, Y_0)} \frac{(1 + X^s)^{\frac{1}{3}}}{\left[\frac{(R_\rho + Y^s)}{(1 + X^s)} - 0.5 \right]}. \quad (\text{E.1})$$

Equating equations 2.47 and E.1 leads to the following equation that is obeyed by the steady-state values of X^s , Y^s and a^s (we have checked that our solutions obey this equation):

$$(1 + a^s) = \frac{(\frac{\tilde{s}}{m})^2 (Y^s - X^s) (\frac{D_0}{D^{ss}})}{(1 + X^s)^{\frac{4}{3}} \left(1 - \frac{\alpha \Theta_l}{\beta S_{A_l}} \right)} \left[\frac{(R_\rho + Y^{ss})}{(1 + X^s)} - 0.5 \right] \left[\frac{A(X_0, Y_0)}{X_0} \right]. \quad (\text{E.2})$$

Appendix F

HRM: Evaluation of the Left-hand Side of Equation 3.8

To calculate the left-hand side of equation 3.8, we use a “two-triangle” calculation. The vertical face at constant latitude through which the transport passes is shown in Fig. F.1, and the words “two-triangle” refers to triangle ABC and ADE for the calculation of transport through area ADE. Fig. F.1 covers the width of three boxes of the coarse-resolution model, that is, it contains three T, S points and eight velocity points. The total transport through the whole area is the sum of the signed transport through ADE and AD'E' compared with that of the Eulerian-mean transport. Note that because the slopes of AD and AD' are being calculated separately, they are not necessarily the same. The first step of the two-triangle calculation is to calculate the velocities at points E, C, E' and C' by vertically averaging the given velocity data that is at the vertices of the cubes of the T, S boxes of the fine resolution data. Then we calculate the spatially averaged Eulerian velocity at $\langle \bar{z}_a \rangle$ using $v_0 = \frac{1}{6}v_{E'} + \frac{1}{3}v_{C'} + \frac{1}{3}v_C + \frac{1}{6}v_E$. This spatially averaged Eulerian mean velocity is then subtracted from all velocities to obtain the perturbation velocities. Since the same method is conducted similarly on the western half of Fig. F.1 as on the eastern half, we concentrate here on describing what we do on the eastern half.

The heights of points D and B are given by $z_D - z_E = \frac{3}{2}(z_H - z_E)$ and $z_B - z_E = \frac{1}{2}(z_H - z_E)$, where z_H indicates the height where the neutral tangent plane connects the

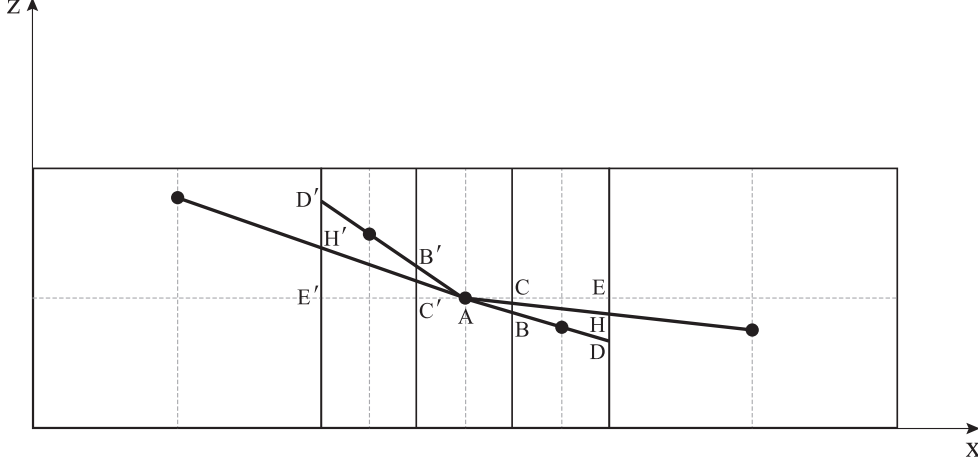


Figure F.1: Vertical cross-section through three boxes of a coarse-resolution ocean model, with the central box showing three boxes of a finer resolution ocean model that has three times the horizontal resolution compared with the coarse resolution model. For the fine resolution boxes, the slopes of the density surfaces are given by the lines from the central point to the dots at points on the fine-scale grid boxes, while for the coarse-resolution data the slopes of the density surfaces are determined by the lines from the central point to the other two dots at the centre (horizontally) of the coarse-resolution boxes.

central point A to point H on the vertical T, S cast at the longitude mid way between the longitudes of points C and E. Now knowing the locations of points B and D, we find the vertically adjacent locations on the fine-resolution model grid where the velocity components are stored, and the velocities at points B and D are then found by vertical interpolation.

First consider the (perturbation) transport into the page passing through the vertical area ACB. The perturbation velocities at these points are v'_A, v'_C and v'_B . At any position (x, z) within ABC, the velocity through the vertical area can be denoted as $v' = v'_A + (v'_C - v'_A)\frac{x}{X} + (v'_B - v'_C)\frac{z}{Z}$, where X and Z are the signed lengths of AC and BC. The required horizontal volume flux of marked fluid is equal to the “volume” of a three-dimensional space where the spatial directions to the east and upwards (x, z) are

two of the dimensions, and the third dimension is the perturbation meridional velocity v' . The volume is

$$\begin{aligned}
 \text{"volume" of ABC} &= \int_0^X \int_0^{\frac{x}{X}Z} v' dz dx \\
 &= \int_0^X \int_0^{\frac{x}{X}Z} \left[v'_A + (v'_C - v'_A) \frac{x}{X} + (v'_B - v'_C) \frac{z}{Z} \right] dz dx \\
 &= \int_0^X \left[v'_A \frac{Z}{X} x + \frac{(v'_C - v'_A)}{X} \frac{Z}{X} x^2 + \frac{1}{2} \frac{(v'_B - v'_C)}{Z} \left(\frac{Z}{X} \right) x^2 \right] dx \\
 &= \frac{1}{2} X Z \left[\frac{1}{3} (v'_A + v'_B + v'_C) \right].
 \end{aligned} \tag{F.1}$$

We note from this expression that the transport into the page is equal to the signed area of triangle ABC multiplied by the average of the perturbation velocity at the three vertices of the triangle. The derivation of this expression follows the same Taylor series expansion and spatial integration as performed by McDougall (1998), and the correspondence to the main HRM result of McDougall (1998), which is equation 3.5, can be seen as follows. McDougall (1998) took the perturbation velocity at the centre, v'_A , to be zero, and in this case, we can write the last line of equation F.1 as $\frac{1}{6} X Z [2v'_C + (v'_B - v'_C)]$. With X being half the box width, that is, $X = \frac{1}{2} \Delta x$, with Z being $Z = \frac{1}{2} \Delta x L^x$, with $2v'_C$ being $\bar{v}_x \Delta x$, and with $(v'_B - v'_C)$ being $\frac{1}{2} L^x \bar{v}_z \Delta x$, the right-hand side of equation F.1 is one half of the right-hand side of equation 3.5; the factor of one half being due to the fact that triangle ABC represents just the right-hand half of the transport of marked fluid in this model box.

We note that in equation F.1, v'_C and v'_B are not individually important; rather it is their mean value that enters this expression. We will use this property to simplify the evaluation of the three-dimensional space corresponding to area AED, where we will take the average of the perturbation velocities at points D and E, as well as those at points B and C. In Fig. F.2 we sketch the three-dimensional volume whose volume we seek to evaluate. We have drawn Fig. F.2 with both v'_D and v'_E equal to the same value, $0.5(v'_D + v'_E)$. The same is done for v'_A and v'_B , both having the value $0.5(v'_A + v'_B)$. These average perturbation velocities are now used to extrapolate these velocities to the

spatial location of point A, obtaining namely $v'_{A'}$. Note that this extrapolated velocity is different to the actual perturbation velocity at point A, namely v'_A , (obtained by interpolation of the perturbation velocities at the height of point A).

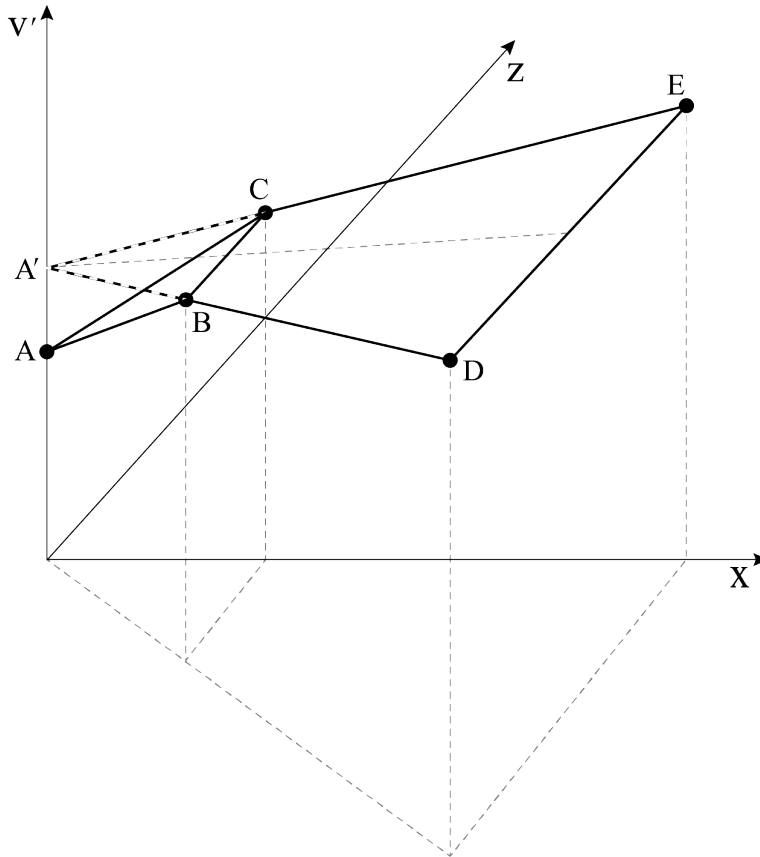


Figure F.2: The three-dimensional view of two-triangle calculation for transports.

From Fig. F.2 the transport through the vertical triangle ACEDBA of Fig. F.1 is equal to the difference between two volumes; being the volume from the $v' = 0$ plane up to the inclined triangle A'DE, minus the volume between the two inclined triangles A'BC and ABC. Both of these volumes can be evaluated using the above “triangular volume” equation with suitable reassignments of the corners of the triangle. Note that the first volume usually dominates: for example, the relevant value of XZ for the large triangle is nine times the corresponding value of XZ for the small triangle.

The evaluation of HRM transport is at the average height of the neutral density surface $\langle \bar{z}_a \rangle$. However, in practice, the average depth of the above triangle calculations is not necessarily the same as $\langle \bar{z}_a \rangle$, since the slopes of the density surfaces are different to the east and to the west. The two-triangle calculation includes extra transport due to its density surface being higher in the water column by the height difference given by equation 3.9, namely $\delta z = \frac{1}{8}(z_E - \langle \bar{z}_a \rangle) + \frac{1}{8}(z_W - \langle \bar{z}_a \rangle) = \frac{1}{8}(L_E^x - L_W^x)\Delta x$. The extra transport is

$$\left(\frac{1}{6}v'_{D'} + \frac{1}{3}v'_{B'} + \frac{1}{3}v'_B + \frac{1}{6}v'_D - \frac{1}{2}\langle \bar{v} \rangle_z \delta z \right) \Delta x \delta z \quad (\text{F.2})$$

and this transport is subtracted from that calculated using the above two-triangle calculation.

The “two-triangle” method is a way to fully utilize the fine resolution data. Three tracer points and eight velocity points are all included in the “two-triangle” calculation. The transport calculated by this method is considered to be the accurate transport and hence was used to determine how good the Taylor Series approximation is.

Bibliography

- D. Andrews, J. Holton, and C. Leovy. *Middle Atmosphere Dynamics*. International geophysics series. Academic Press, 1987.
- D. G. Andrews and M. E. McIntyre. Planetary Waves in Horizontal and Vertical Shear: The Generalized Eliassen-Palm Relation and the Mean Zonal Acceleration. 33:2031–2048, 1976.
- J. D. Boyd. Properties of thermohaline staircase off the northeast coast of South America. Spring and Fall 1985. *Journal of Geophysical Research*, 94:8303–8312, 1989.
- J. D. Boyd and H. Perkins. Characteristics of thermohaline steps off the northeast coast of South America, July 1983. *Deep Sea Research Part A, Oceanographic Research Papers*, 34(3):337–364, 1987.
- C. Eden. Anisotropic Rotational and Isotropic Residual Isopycnal Mesoscale Eddy Fluxes. *Journal of Physical Oceanography*, 40(11):2511–2524, 2010. ISSN 0022-3670. doi: 10.1175/2010JPO4397.1.
- C. Eden. Relating Lagrangian, Residual, and Isopycnal Means. *Journal of Physical Oceanography*, 42(7):1057–1064, 2012. ISSN 0022-3670. doi: 10.1175/JPO-D-11-068.1. URL <http://journals.ametsoc.org/doi/abs/10.1175/JPO-D-11-068.1>.
- A. Eliassen and E. Palm. *On the Transfer of Energy in Stationary Mountain Waves*. Det Norske Videnskaps-Akademi i Oslo. Geofysiske publikasjoner. I kommisjon hos Aschehoug, 1961.
- A. F. Fanning and A. J. Weaver. A horizontal resolution and parameter sensitivity

- study of heat transport in an idealized coupled climate model. *Journal of Climate*, 10(10):2469–2478, 1997.
- A. E. Gargett and G. Holloway. Sensitivity of the GFDL ocean model to different diffusivities for heat and salt. *Journal of Physical Oceanography*, 22(10):1158–1177, 1992.
- P. R. Gent. The Gent–McWilliams parameterization : 20/20 hindsight. *Ocean Modelling*, 39:2–9, 2011.
- P. R. Gent and J. C. McWilliams. Isopycnal Mixing in Ocean Circulation Models. *Journal of Physical Oceanography*, 20(1):150–155, 1990.
- P. R. Gent, J. Willebrand, T. J. McDougall, and J. C. McWilliams. Parameterizing Eddy-Induced Tracer Transports in Ocean Circulation Models. *Journal of Physical Oceanography*, 25(4):463–474, 1995.
- F. S. Graham and T. J. McDougall. Quantifying the Nonconservative Production of Conservative Temperature, Potential Temperature, and Entropy. *Journal of Physical Oceanography*, 43(5):838–862, 2013.
- M. C. Gregg. The three-dimensional mapping of a thermohaline intrusion. *Journal of Physical Oceanography*, 10:1468–1492, 1980.
- M. G. Gregg and J. H. McKenzie. Thermohaline intrusions lie across isopycnals. *Nature*, 280:310–311, 1979.
- S. M. Griffies. *Fundamentals of Ocean Climate Models*. Princeton Press, 2004.
- S. K. Gulev, B. Barnier, J. M. Molines, T. Penduff, and J. Chanut. Impact of spatial resolution on simulated surface water mass transformations in the Atlantic. *Ocean Modelling*, 19(3-4):138–160, 2007.
- H. E. Huppert. On the stability of a series of double-diffusive layers. *Deep-Sea Research and Oceanographic Abstracts*, 18(10):1005–1021, 1971.
- IOC, SCOR, and IAPSO. The international thermodynamic equation of seawater 2010: Calculation and use of thermodynamic properties. *Intergovernmental Oceanographic Commission, Manuals and Guides No. 56*, (June):196, 2010.

- W. S. Jevons. II. On the cirrous form of cloud. *Philosophical Magazine Series 4*, 14 (90):22–35, 1857.
- O. M. Johannessen and O. S. Lee. A deep stepped thermo-haline structure in the Mediterranean. *Deep-Sea Research and Oceanographic Abstracts*, 21(8):629–639, 1974.
- T. Joyce, W. Zenk, and J. M. Toole. Anatomy of the Antarctic Polar Front in the Drake Passage. *Journal of Geophysical Research-Oceans and Atmospheres*, 83(8):6093–6113, 1978.
- A. Klocker and T. J. McDougall. Influence of the Nonlinear Equation of State on Global Estimates of Dianeutral Advection and Diffusion. *Journal of Physical Oceanography*, 40(8):1690–1709, 2010.
- E. Kunze. A review of oceanic salt-fingering theory. *Progress in Oceanography*, 56(3-4):399–417, 2003.
- J. R. Ledwell, A. J. Watson, and C. S. Law. Evidence for slow mixing across the pycnocline from an open-ocean tracer-release experiment. *Nature*, 364(6439):701–703, 1993.
- J. R. Ledwell, E. T. Montgomery, K. L. Polzin, L. C. St. Laurent, R. W. Schmitt, and J. M. Toole. Evidence for enhanced mixing over rough topography in the abyssal ocean. *Nature*, 403(6766):179–182, 2000.
- J. R. Ledwell, L. C. St. Laurent, J. B. Girton, and J. M. Toole. Diapycnal Mixing in the Antarctic Circumpolar Current. *Journal of Physical Oceanography*, 41:241–246, 2011.
- J. R. Maddison and D. P. Marshall. The EliassenPalm flux tensor. *Journal of Fluid Mechanics*, 729:69–102, 2013.
- G. O. Marmorino and D. R. Caldwell. Heat and salt transport through a diffusive thermohaline interface. *Deep-Sea Research and Oceanographic Abstracts*, 23(1):59–67, 1976. ISSN 00117471. doi: 10.1016/0011-7471(76)90808-1.

- P. A. Mazeika. Subsurface Mixed Layers in the Northwestern Tropical Atlantic. *Journal of Physical Oceanography*, 4(3):446–453, 1974.
- T. McDougall, S. Groeskamp, and S. Griffies. Comment on Tailleux, R. Neutrality versus Materiality: A Thermodynamic Theory of Neutral Surfaces. *Fluids* 2016, 1, 32. *Fluids*, 2(2):19, 2017.
- T. J. McDougall. Double-Diffusive Interleaving. Part I: Linear Stability Analysis. *Journal of Physical Oceanography*, 15:1532–1541, 1985a.
- T. J. McDougall. Double-Diffusive Interleaving. Part II: Steady State Interleaving. *Journal of Physical Oceanography*, 15:1542–1556, 1985b.
- T. J. McDougall. *Three-Dimensional Residual-Mean Theory*. Springer, 1998.
- T. J. McDougall. Potential Enthalpy: A Conservative Oceanic Variable for Evaluating Heat Content and Heat Fluxes. *Journal of Physical Oceanography*, 33(5):945–963, 2003.
- T. J. McDougall and P. M. Barker. *Getting started with TEOS-10 and the Gibbs Seawater (GSW) Oceanographic Toolbox*. Number January. 2011.
- T. J. McDougall and D. R. Jackett. The material derivative of neutral density. *Journal of Marine Research*, 63(1):159–185, 2005.
- T. J. McDougall and P. C. McIntosh. The Temporal-Residual-Mean Velocity. Part I: Derivation and the Scalar Conservation Equations. *Journal of Physical Oceanography*, 26(12):2653–2665, 1996.
- T. J. McDougall and P. C. McIntosh. The Temporal-Residual-Mean Velocity. Part II: Isopycnal Interpretation and the Tracer and Momentum Equations. *Journal of Physical Oceanography*, 31(5):1222–1246, 2001.
- T. J. McDougall and J. R. Taylor. Flux measurements across a finger interface at low values of the stability ratio. *Journal of Marine Research*, (42):1–14, 1984.
- T. J. McDougall, S. Groeskamp, and S. M. Griffies. On Geometrical Aspects of Interior Ocean Mixing. *Journal of Physical Oceanography*, 44(8):2164–2175, 2014.

- A. Melet, R. Hallberg, S. Legg, and K. Polzin. Sensitivity of the Ocean State to the Vertical Distribution of Internal-Tide Driven Mixing. *Journal of Physical Oceanography*, pages 602–615, 2012.
- W. J. Merryfield. Origin of Thermohaline Staircases. *Journal of Physical Oceanography*, 30(5):1046–1068, 2000.
- R. D. Mueller, W. D. Smyth, and B. Ruddick. Shear and convective turbulence in a model of thermohaline intrusions. *Journal of Physical Oceanography*, 37(10):2534–2549, 2007.
- T. Penduff, M. Juza, L. Brodeau, G. C. Smith, B. Barnier, J.-M. Molines, A.-M. Treguier, and G. Madec. Impact of global ocean model resolution on sea-level variability with emphasis on interannual time scales. *Ocean Science*, 6:269–284, 2010.
- P. Porta Mana and L. Zanna. Toward a stochastic parameterization of ocean mesoscale eddies. *Ocean Modelling*, 79:1–20, 2014.
- S. Riha. Methods for forming approximately neutral surfaces in the ocean, 2017.
- S. R. Rintoul and C. Wunsch. Mass, heat, oxygen and nutrient fluxes and budgets in the North Atlantic Ocean. *Deep Sea Research Part A. Oceanographic Research Papers*, 38, Supple(0):S355–S377, 1991.
- B. Ruddick and A. E. Gargett. Oceanic double-infusion: introduction. *Progress in Oceanography*, 56(3-4):381–393, mar 2003.
- B. R. Ruddick. The Life of a Thermohaline Intrusion. *J. Mar. Res.*, 42(1973):831–852, 1984.
- B. R. Ruddick, R. W. Griffiths, and G. Symonds. Frictional Stress at a Sheared Double-Diffusive Interface. *Journal of Geophysical Research*, 94(C12):161–173, 1989.
- R. W. Schmitt. Flux measurements on salt fingers at an interface. *Journal of Marine Research*, 37(3):2913–1919, 1979.
- R. W. Schmitt. Double Diffusion in Oceanography. *Annual Review of Fluid Mechanics*, 26:255–285, 1994.

- R. W. Schmitt and D. T. Georgi. Fine-structure and microstructure in the North Atlantic Current. *Journal of Marine Research*, 40:659–705, 1982.
- R. W. Schmitt, H. Perkins, J. D. Boyd, and M. C. Stalcup. C-SALT: An investigation of the thermohaline staircase in the western tropical North Atlantic. *Deep Sea Research Part A, Oceanographic Research Papers*, 34(10):1655–1665, 1987.
- W. D. Smyth and S. Kimura. Instability and Diapycnal Momentum Transport in a Double-Diffusive, Stratified Shear Layer. *Journal of Physical Oceanography*, 37(1985):1551–1565, 2007.
- L. St. Laurent, A. C. Naveira Garabato, J. R. Ledwell, A. M. Thurnherr, J. M. Toole, A. J. Watson, L. S. Laurent, A. C. N. Garabato, J. R. Ledwell, A. M. Thurnherr, J. M. Toole, and A. J. Watson. Turbulence and Diapycnal Mixing in Drake Passage. *Journal of Physical Oceanography*, 42(12):2143–2152, 2012.
- M. E. Stern. The Salt-Fountain and Thermohaline Convection. *Tellus*, 12(2):172–175, 1960.
- P. H. Stone and G. Salustri. Generalization of the Quasi-Geostrophic Eliassen-Palm Flux to Include Eddy Forcing of Condensation Heating. *Journal of the Atmospheric Sciences*, 41(24):3527–3536, 1984.
- R. I. Tait and M. R. Howe. Some observation of thermohalin stratification in the deep ocean. *Deep Sea Research*, 15:275–280, 1968.
- J. M. Toole. Intrusion Characteristics in the Antarctic Polar Front. *Journal of Physical Oceanography*, 11(6):780–793, 1981.
- J. M. Toole and D. T. Georgi. On the dynamics and effects of double-diffusively driven intrusions. *Progress in Oceanography*, 10(2):123–145, 1981.
- A. M. Treguier, S. Theetten, E. P. Chassignet, T. Penduff, R. Smith, L. Talley, J. O. Beismann, and C. Böning. The North Atlantic Subpolar Gyre in Four High-Resolution Models. *Journal of Physical Oceanography*, 35(5):757–774, 2005.
- A. M. Treguier, C. Lique, J. Deshayes, and J. M. Molines. The North Atlantic Eddy Heat Transport and Its Relation with the Vertical Tilting of the Gulf Stream Axis.

- Journal of Physical Oceanography*, 47(6):1281–1289, 2017. ISSN 0022-3670. doi: 10.1175/JPO-D-16-0172.1. URL <http://journals.ametsoc.org/doi/10.1175/JPO-D-16-0172.1>.
- K. E. Trenberth. An Assessment of the Impact of Transient Eddies on the Zonal Flow during a Blocking Episode Using Localized Eliassen-Palm Flux Diagnostics. *Journal of Atmospheric Sciences*, 43(19):2070–2087, 1986.
- J. Turner. Salt fingers across a density interface. *Deep Sea Research and Oceanographic Abstracts*, 14(5):599–611, oct 1967.
- J. S. Turner. The coupled turbulent transport of salt and heat across a sharp density interface. *International Journal of Heat and Mass Transfer*, 8(5):759–767, 1965. ISSN 00179310. doi: 10.1016/0017-9310(65)90022-0. URL [http://dx.doi.org/10.1016/0017-9310\(65\)90022-0](http://dx.doi.org/10.1016/0017-9310(65)90022-0).
- D. Walsh and B. Ruddick. Nonlinear equilibration of thermohaline intrusions. *J Phys Oceanogr J Phys Oceanogr*, 28(6):1043–1070, 1998.
- A. J. Williams. The role of double diffusion in a Gulf Stream frontal intrusion. *Journal of Geophysical Research*, 86(C3):1917–1928, 1981.
- W. R. Young. An Exact Thickness-Weighted Average Formulation of the Boussinesq Equations. *Journal of Physical Oceanography*, 42(5):692–707, 2012.
- J. Zhang, R. W. Schmitt, and R. X. Huang. Sensitivity of the GFDL Modular Ocean Model to Parameterization of Double-Diffusive Processes*. *Journal of Physical Oceanography*, 28(4):589–605, 1998.
- G. Zodiatis and G. P. Gasparini. Thermohaline staircase formations in the Tyrrhenian Sea. *Deep-Sea Research Part I: Oceanographic Research Papers*, 43(5):655–678, 1996.